

# **Investigation of the atmospheric water cycle on Mars by the Planetary Fourier Spectrometer onboard Mars Express**

Dissertation  
zur Erlangung des Doktorgrades  
der Mathematisch-Naturwissenschaftlichen Fakultäten  
der Georg-August-Universität zu Göttingen

vorgelegt von  
**Martin Alexander Tschimmel**  
aus Roding

Göttingen 2007

## **Bibliografische Information Der Deutschen Bibliothek**

Die Deutsche Bibliothek verzeichnet diese Publikation in der Deutschen Nationalbibliografie; detaillierte bibliografische Daten sind im Internet über <http://dnb.ddb.de> abrufbar.

D7

Referent: Prof. Dr. A. Tilgner

Korreferent: PD Dr. D. Schmitt

Tag der mündlichen Prüfung: 1. Februar 2007

Copyright © Copernicus GmbH 2007

ISBN 978-3-936586-63-3

Copernicus GmbH, Katlenburg-Lindau

Druck: Schaltungsdienst Lange, Berlin

Printed in Germany

Für Niki.  
Für meine Eltern.



# Contents

<b>Zusammenfassung</b>	<b>7</b>
<b>Summary</b>	<b>9</b>
<b>1 Introduction</b>	<b>11</b>
1.1 The planet Mars . . . . .	11
1.2 Open questions and future missions . . . . .	16
1.3 Research objective . . . . .	17
1.4 Outline . . . . .	17
<b>2 The atmosphere of Mars</b>	<b>19</b>
2.1 Composition and chemistry . . . . .	19
2.2 Structure of the atmosphere . . . . .	20
2.3 Dust and CO <sub>2</sub> cycle . . . . .	21
2.4 Atmospheric physics . . . . .	23
2.4.1 Large scale dynamics . . . . .	25
2.4.2 Effects on mesoscale and small scales . . . . .	29
2.5 Evolution of the climate . . . . .	30
<b>3 Water vapour on Mars</b>	<b>33</b>
3.1 History of H <sub>2</sub> O observations . . . . .	33
3.1.1 Spacecraft exploration . . . . .	33
3.1.2 Observations from Earth . . . . .	36
3.2 The seasonal cycle of atmospheric water . . . . .	38
3.3 Surface–atmosphere interaction . . . . .	40
3.4 The diurnal cycle and an alternate theory . . . . .	42
<b>4 The PFS experiment on <i>Mars Express</i></b>	<b>45</b>
4.1 The <i>Mars Express</i> mission . . . . .	45
4.2 The Planetary Fourier Spectrometer . . . . .	46
4.3 PFS in-flight performance . . . . .	48
4.4 PFS observations and spectrum averaging . . . . .	51
<b>5 Data analysis</b>	<b>55</b>
5.1 Introduction to spectroscopy . . . . .	55
5.2 The retrieval algorithm and the preparation of the PFS measurements . . . . .	57
5.3 The synthetic spectrum . . . . .	58

5.3.1	Vertical atmospheric profiles . . . . .	58
5.3.2	The monochromatic transmittance spectrum . . . . .	59
5.3.3	Convolution with solar spectrum and instrumental function . . . . .	61
5.4	Normalization of the spectra . . . . .	63
5.5	Data fitting and continuum correction . . . . .	65
5.6	Examples of spectral fits . . . . .	66
5.7	Fitting improvements . . . . .	67
5.8	Discussion of uncertainties . . . . .	71
5.8.1	Uncertainties from numerical models . . . . .	71
5.8.2	Instrumental errors . . . . .	73
5.8.3	Uncertainties of the retrieval method . . . . .	74
<b>6</b>	<b>Results and discussion</b>	<b>79</b>
6.1	Seasonal cycle . . . . .	79
6.2	Retrieved reflectance . . . . .	83
6.3	Spatial variations . . . . .	84
6.4	Diurnal variations . . . . .	88
6.5	Comparison of results from individual orbits . . . . .	89
6.6	Comparison of the global water behaviour . . . . .	101
6.7	Vertical distribution . . . . .	104
<b>7</b>	<b>Conclusions and outlook</b>	<b>105</b>
7.1	Conclusions . . . . .	105
7.2	Future work and outlook . . . . .	107
<b>A</b>	<b>Appendix</b>	<b>109</b>
A.1	The definition of a martian year . . . . .	109
A.2	The spectral bands of water vapour in the PFS range . . . . .	109
A.3	The European Mars Climate Database (EMCD) . . . . .	109
A.4	Measurement quantities of H <sub>2</sub> O . . . . .	110
A.5	Hamming apodization . . . . .	112
A.6	Radiometric terminology . . . . .	112
	<b>Bibliography</b>	<b>113</b>
	<b>Publications</b>	<b>123</b>
	<b>Acknowledgements</b>	<b>125</b>
	<b>Curriculum Vitae</b>	<b>127</b>

# Zusammenfassung

Eines der Hauptziele von Weltraummissionen und erdgebundener Beobachtung des Mars ist die Untersuchung des Wasserdampfhaushalts. Diese Beobachtungen zeigen starke jahreszeitliche, räumliche und tageszeit-abhängige Veränderungen des Wassers in der Atmosphäre, was eine Vielzahl von verantwortlichen physikalischen Prozessen nahelegt. Diese sind der Austausch von Wasserdampf mit den Polkappen und dem Regolith und der Transport durch die atmosphärische Zirkulation. Die Raumsonde *Mars Express*, die den Planeten seit Januar 2004 umkreist, trägt das leistungsfähige Instrument "Planetary Fourier Spectrometer" (PFS) an Bord, das infrarotes Licht im Bereich zwischen 1.2 und 40  $\mu\text{m}$  bei hoher spektraler Auflösung aufnimmt. Die Spektren atmosphärischen Wassers im 2.6  $\mu\text{m}$  Band, die während mehr als einem halben Marsjahr aufgenommen wurden, wurden in dieser Arbeit untersucht.

Für die Analyse wurden die relativen Bandtiefen der Wasserlinien mit einem synthetischen Spektrum gefittet. Diese Maßnahme war hilfreich, da eine absolute Kalibration der PFS Spekten im kurzwelligen Kanal (SW) auf Grund von Problemen mit dem Instrument, die während der Flugphase auftraten, nicht möglich ist. Deshalb beinhaltet die Analyseprozedur eine sorgfältige Definition des Kontinuums, um den bestmöglichen Fit zu erhalten.

Die Verarbeitung des gesamten vorhandenen Datensatzes lieferte überraschende Ergebnisse über den Wasserdampf zwischen Januar 2004 und April 2005. Dieser Zeitraum deckt die Jahreszeiten zwischen  $L_S=331^\circ$  des Marsjahres 26 und  $L_S=196^\circ$  des darauffolgenden Jahres ab. Die Ergebnisse sind wie folgt:

- Die mittlere Säulendichte während der Saison der Tag-und-Nacht-Gleiche vor dem nördlichen Sommer beträgt 8.2 pr.  $\mu\text{m}$ . Die erreichten Maximalwerte während des nördlichen Sommers sind 65 pr.  $\mu\text{m}$ , die um den 75. Breitengrad Nord zentriert sind. Nach  $L_S=130^\circ$  verschwindet das Maximum rasch innerhalb eines halben Marsmonats. Zur gleichen Zeit gibt es eine Spitze von 15–20 pr.  $\mu\text{m}$ , die südwärts wandert und den Äquator bei etwa  $L_S=190^\circ$  erreicht. Dabei wird jedoch nur eine kleine Menge Wasser transportiert, während der Großteil an der Oberfläche als Eis abgelagert wird oder durch den Regolith adsorbiert wird.
- Während  $L_S=335-70^\circ$  ist ein tageszeit-abhängiger Prozeß sichtbar, und zwar eine Zunahme der  $\text{H}_2\text{O}$  Säulendichte um 2–3 pr.  $\mu\text{m}$  vom Morgen bis zum frühen Nachmittag. Im Rest des beobachteten Jahres wird dieser Anstieg nicht gefunden.
- Ein direkter Vergleich verschiedener PFS Kanäle zeigt, daß besonders für den nördlichen Sommer die PFS/LW Ergebnisse nördlich des 50. Breitengrades signifikant niedriger sind als diejenigen von PFS/SW. Diese Tatsache legt stark nahe,

daß die vertikale Verteilung des Wassers nicht eine gleichmäßige Mischung mit CO<sub>2</sub> bis hinauf zur Sättigungsgrenze ist, sondern eher eine Konzentration auf die unteren paar Kilometer über der Oberfläche darstellt.

- Die geographische Verteilung zeigt zwei Maxima, deren H<sub>2</sub>O Häufigkeiten etwa um einen Faktor zwei größer sind als im Vergleich zu benachbarten Regionen. Diese Maxima sind über Arabia Terra und dem Tharsis Hochland und werden höchstwahrscheinlich durch eine Wechselwirkung zwischen Atmosphäre und Boden und durch atmosphärische Zirkulation verursacht.
- Auch die Verteilung um den Nordpol ist im Sommer ungleichmäßig bezüglich der Längengrade. Ein breites Minimum wurde zwischen 30° West und 10° Ost nachgewiesen. Über dem Rest der polaren Gegend ist das atmosphärische Wasser ebenfalls in Maxima und Minima verteilt, was ungleichmäßige Sublimations- und Resublimationsprozesse nahelegt.
- Prinzipiell stimmt der beobachtete Wasserdampfkreislauf sehr gut mit vorherigen erdgebundenen und orbitalen Messungen überein. Vorhandene Abweichungen haben ihre Ursache eher in Meßungenauigkeiten als in tatsächlichen Unterschieden, weil alle Instrumente nur eine gewisse Genauigkeit haben. Dies führt zu der Schlußfolgerung, daß sich der Wasserdampfzyklus jedes Jahr auf die gleiche Weise wiederholt, zumindest zu Zeiten niedriger Opazität durch Staub.
- Ein Zusammenhang zwischen Wasserdampfmenge und gewonnenen Daten über den relativen Reflexionsgrad der Oberfläche konnte nicht festgestellt werden.
- Zuletzt ergeben die Messungen, nicht nur von PFS/SW, sondern von allen Spektrometern auf *Mars Express*, einheitlich niedrigere Ergebnisse als sie von der European Mars Climate Database berechnet werden, weshalb dieses Modell verbessert werden muß.

# Summary

One of the main goals of space missions and ground based observations of Mars is the study of its water vapour cycle. These observations exhibit strong seasonal, spatial and even a diurnal variability of atmospheric water that implies a variety of physical processes involved. Those are the exchange of water vapour with the polar caps and regolith, and transport by the general atmospheric circulation. The *Mars Express* spacecraft, orbiting the planet since January 2004, carries the powerful Planetary Fourier Spectrometer (PFS) recording infrared light between 1.2 and 40  $\mu\text{m}$  with high spectral resolution. The spectra of atmospheric water in the 2.6  $\mu\text{m}$  band, taken during more than half a Martian year, were investigated in this work.

In the analysis the relative band depths of water lines were fitted with a synthetic spectrum. This measure was useful because an absolute calibration of the PFS spectra is not possible in the shortwavelength range (SW) due to instrumental problems occurring during flight. Therefore the analysis procedure includes a careful definition of the continuum in order to get the best possible fit.

The processing of the entire available dataset yielded intriguing results about the water vapour between January 2004 and April 2005. This time covers the season between  $L_S=331^\circ$  of Mars Year 26 to  $L_S=196^\circ$  of the consecutive year. The findings are as follows:

- The mean column density of the equinox season before northern summer is 8.2 pr.  $\mu\text{m}$ . The maximum reached values during northern summer are 65 pr.  $\mu\text{m}$ , centered around  $75^\circ\text{N}$  latitude. After  $L_S=130^\circ$  the maximum vanishes quickly within half a martian month. At the same time there is a spike of 15–20 pr.  $\mu\text{m}$  that progresses southward and reaches the equator at about  $L_S=190^\circ$ . However, in this process only a small amount of water is transported while the bulk is stored on the surface, either as ice or adsorbed by the regolith.
- During  $L_S=335-70^\circ$  there is a diurnal process visible, namely an increase of  $\text{H}_2\text{O}$  column density of 2–3 pr.  $\mu\text{m}$  from morning to early afternoon. At the rest of the observed year this rise is not found in the data.
- A direct comparison of different PFS channels shows that in particular for the northern summer the PFS/LW results northward of  $\sim 50^\circ\text{N}$  are significantly lower than those of PFS/SW. This fact strongly suggests that the vertical distribution of water is not an equal mixture with  $\text{CO}_2$  up to the saturation level but rather exhibits a confinement to the lower few kilometers above the surface.
- The geographical distribution shows two maxima whose  $\text{H}_2\text{O}$  abundances are by about a factor of two higher compared to the adjacent regions. These maxima

are over Arabia Terra and the Tharsis highlands and are most probably caused by atmosphere–ground interaction and by atmospheric circulation.

- Also the distribution around the north pole is longitudinally uneven in summer. A broad minimum has been detected between 30°W and 10°E. Above the rest of the polar area the atmospheric water is spread into maxima and minima as well which suggests inhomogeneous sublimation and deposition processes.
- In principle the observed water cycle is in very good agreement with previous ground-based and orbital measurements. Existing disagreements have their origin more likely in measurement uncertainties than in real differences because all instruments have a limited accuracy. This leads to conclude that the water cycle repeats constantly every year, at least in the times of low dust opacity.
- A correlation between H<sub>2</sub>O amounts and retrieved information about the relative reflectance of the surface could not be observed.
- Finally, the measurements, not only of PFS/SW but of all spectrometers on *Mars Express*, yield consistently lower results than calculated by the European Mars Climate Database why this model needs to be improved.

# 1 Introduction

## 1.1 The planet Mars

Mars, the outer neighbour of Earth in the solar system, has been of interest to stargazing humans since prehistoric times. Before the space age the knowledge of it was limited by the performance of the available telescopes. In the early 20<sup>th</sup> century the basic properties of the planet were known, such as its rotation period and the existence of polar caps. Also simple maps were created by the astronomers of that time, some claiming even water channels on Mars. Certainly the necessity of water for life as we know it drove the imagination and scientific investigation of Mars not only then but until today. Therefore the main goal of the first robotic spacecraft sent to the planet was to determine its appearance and the existence of water. The first spacecraft that reached Mars operationally, *Mariner 4* in July 1965, showed a dry, moon-like world without any hints of water. Only more global and advanced research by later probes and ground-based observations proved that liquid water must have flown on Mars, that the north polar ice cap is made up of water ice and that the martian atmosphere contains water in gaseous state. A more detailed review of how this atmospheric water was investigated will be given in chapter 3.1.

Although Mars is often called the brother of Earth as of all planets it has the most Earth-like appearance there are several things that make it quite different. So here the relevant parameters of Mars are presented:

mass:	$6.4185 \cdot 10^{23} \text{ kg}$	=	$0.107 M_{\text{Earth}}$
mean radius:	3390 km	=	$0.532 R_{\text{Earth}}$
surface gravity:	$3.71 \text{ m/s}^2$	=	$0.379 g_{\text{Earth}}$
solar irradiance:	$589.2 \text{ W/m}^2$	=	$0.431 I_{\text{Earth}}$
black-body temperature:	210.1 K	=	$0.826 T_{\text{Earth}}$
semimajor axis:	$227.92 \cdot 10^6 \text{ km}$	=	1.524 AU
eccentricity:	0.0935	=	$5.599 \epsilon_{\text{Earth}}$
sidereal orbit period:	686.980 days	=	$1.881 P_{\text{Earth}}^{\text{orb}}$
sidereal rotation period:	24.623 hours	=	$1.029 P_{\text{Earth}}^{\text{rot}}$

The season of a martian year  $L_S$  is defined as the solar longitude of Mars or, in other words, the positional angle between Mars and the point of its spring equinox. For example  $L_S=0^\circ$  means Mars is at vernal equinox while  $L_S=90^\circ$  means that Mars experiences northern summer solstice. In addition, in the current epoch the northern summer solstice almost coincides with the aphelion point of the orbit ( $L_S=71^\circ$ ) and the southern summer solstice position with the perihelion point ( $L_S=251^\circ$ ), respectively. Similar to Earth the tilt of the martian rotational axis of  $25.2^\circ$  causes seasons. However, due to the high eccentricity of Mars' orbit this has climatic implications as the northern hemisphere experiences a

longer summer than the southern hemisphere but receives less solar radiance at that time. To provide a basis for comparisons between different martian years (MY) the chronology introduced by Clancy et al. (2000) is followed which is explained in appendix A.1.

The topography of Mars is also quite outstanding as it has the highest altitude difference of the surface of all rocky planets. It ranges from the top of Olympus Mons (18°N, 135°W), with about 26 km the largest volcano in the entire solar system, to the depths of the giant Hellas impact basin (45°S, 60°E) which is more than 8 km below the defined MOLA<sup>1</sup> zerolevel of the surface. Hellas is not the only basin, though, there are also the smaller Argyre basin (50°S, 40°W), Isidis (12°N, 88°E) and the buried Utopia Planitia (45°N, 110°E). The same is true for Olympus Mons. It might be the tallest mountain but it is accompanied by three other giant volcanos of about the same size (about 15–18 km height): Ascraeus Mons (12°N, 112°W), Pavonis Mons (0°N, 113°W) and Arsia Mons (9°S, 121°W) which are part of the Tharsis volcanic highland dominating the western hemisphere. In the eastern hemisphere there is also a huge volcano, the ~15 km tall Elysium Mons (25°N, 147°E). One of the most famous features on the Red Planet is the immense rift valley Vallis Marineris (8°S, 90–45°W) which holds with its 4500 km length and more than 5 km depth also the record in the solar system. Witnesses of massive water outflows in its early history can be found on Mars, too. Some of the most striking ones are the Kasei Vallis (24°N, 65°W), northeast of the Tharsis plateau, and the Dao Vallis (38°S, 88°E), east of Hellas.

Reminiscent of Earth, Mars has polar caps as well which consist of a residual ice shield surrounded by the so-called layered terrain, a sequence of lighter and darker material. In winter the poles are additionally covered by a seasonal cap which sublimates in the following summer of the respective hemisphere. Regarding their composition the northern cap is comparable to the terrestrial one since it is composed mainly of water ice. It has a thickness of about 3 km and covers  $1.04 \cdot 10^6 \text{ km}^2$ , including the layered terrain. The south pole cap, however, is made up of 85% CO<sub>2</sub>-ice mixed with 15% H<sub>2</sub>O whose fraction increases towards the scarps on the edges. It is surrounded by permafrost fields containing large amounts of water ice. In the course of the winter the permanent cap is covered by seasonal frost of both water and carbon dioxide ice. The area of the south pole region is  $1.44 \cdot 10^6 \text{ km}^2$ . Finally, an important factor influencing even the martian atmosphere is the dichotomy of the surface into a southern highland and northern lowlands. The height difference between them exceeds 5 km and is most pronounced between the poles. All these mentioned features are displayed in the albedo maps 1.1 and 1.2 and altitude map 1.3. Please note that in this work all geographic locations are given in latitudes of 90° North and South and longitudes of 180° East and West of the defined prime meridian (the tiny crater "Airy 0") while the albedo maps are mapped in West longitude (0–360° W).

A geological look on these landscapes allows their temporal distinction into three major epochs (Read and Lewis 2004) by looking at the cratering statistics. Starting after the early bombardment the Noachian (4.6–3.5 Gyr ago) is the time after the formation of the planet, whose geological features can still be found in the southern highlands which is characterized by extensive cratering. The following Hesperian period (3.5–1.8 Gyr ago) saw the effects of strong volcanic activity at the end of the Noachian. This caused major floodings and the formation of giant lava outflows. The last period, the Amazonian, lasts

---

<sup>1</sup>The Mars Orbiter Laser Altimeter onboard the *Mars Global Surveyor* spacecraft has provided a very high resolution altitude map of Mars (figure 1.3).

until today and is marked by a very weak geological activity and minor erosion by winds, dust and thermal stresses. However, the Amazonian is not completely quiet but sees periodical climate changes every  $10^4$ – $10^6$  years whose records can be found in the layered terrain of the polar hood. As for the geology itself, Mars' typical red colour is due to the omnipresent iron-oxide dust which covers basically the whole surface. Beneath this fine layer the main composition of the minerals are basalts of volcanic origin. Yet more detailed mapping and in-situ exploration showed a large variety of minerals, also involving the interaction with water.

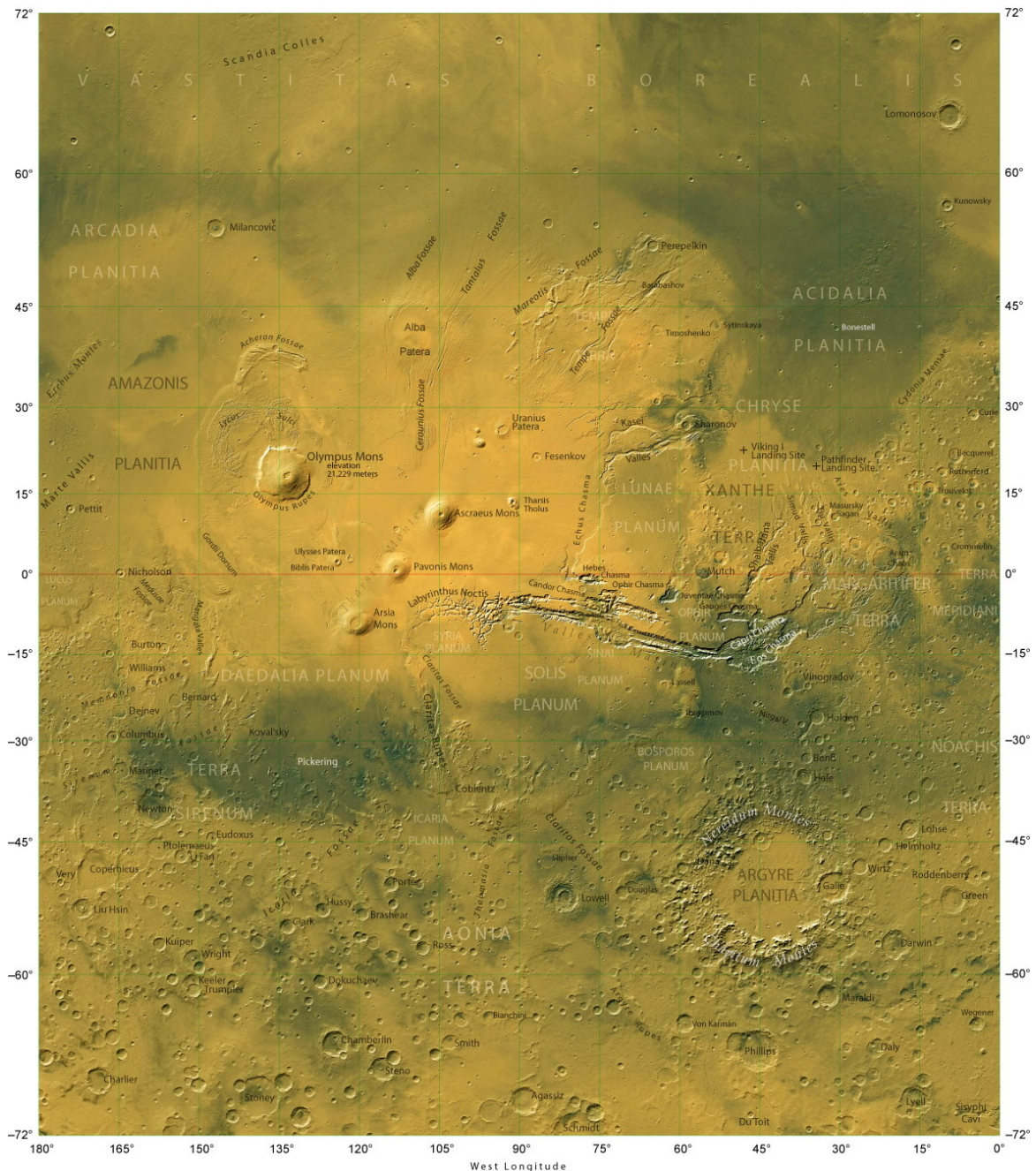


Figure 1.1: The albedo map of the western hemisphere of Mars.

# 1 Introduction

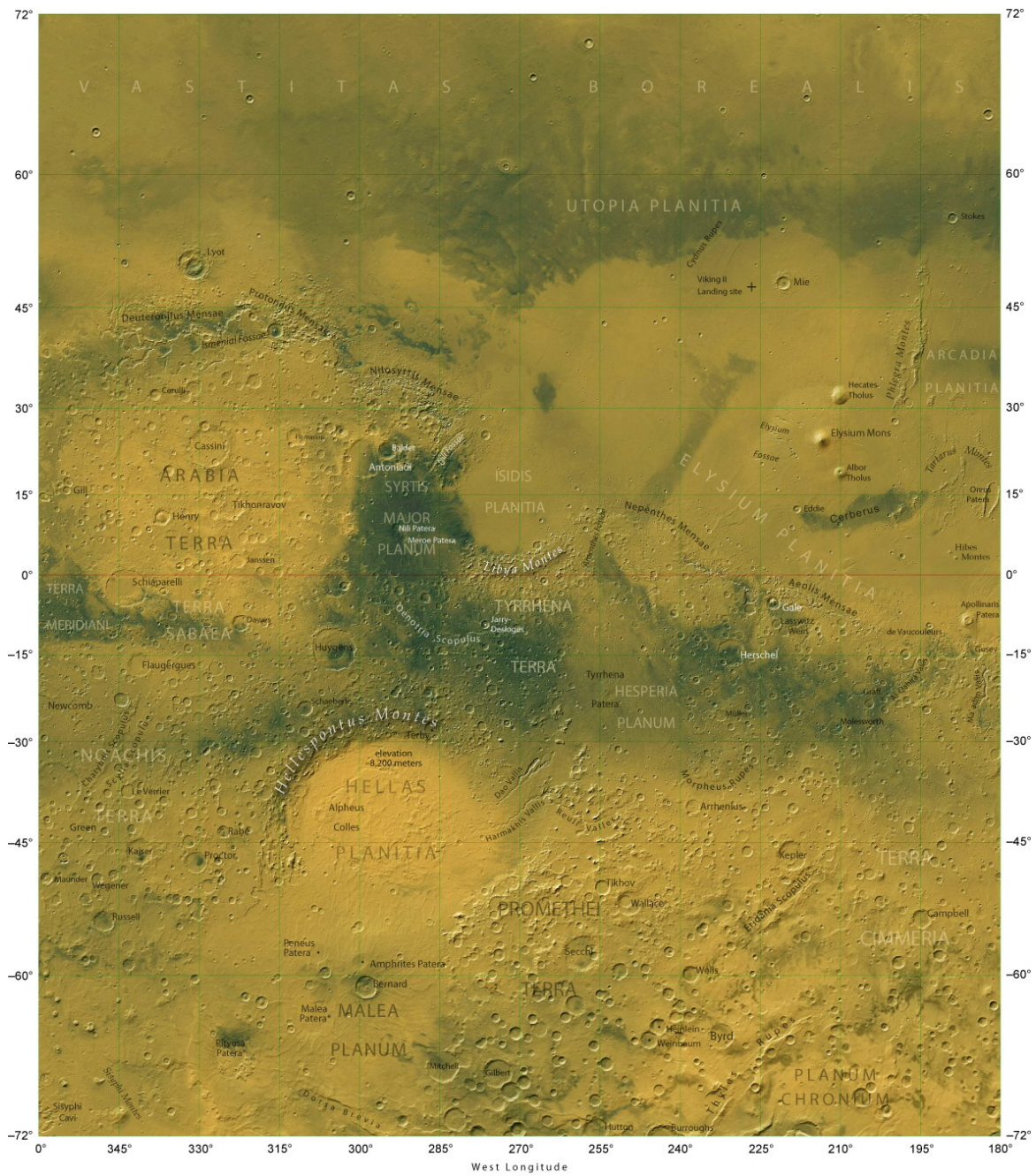


Figure 1.2: The albedo map of the eastern hemisphere of Mars.

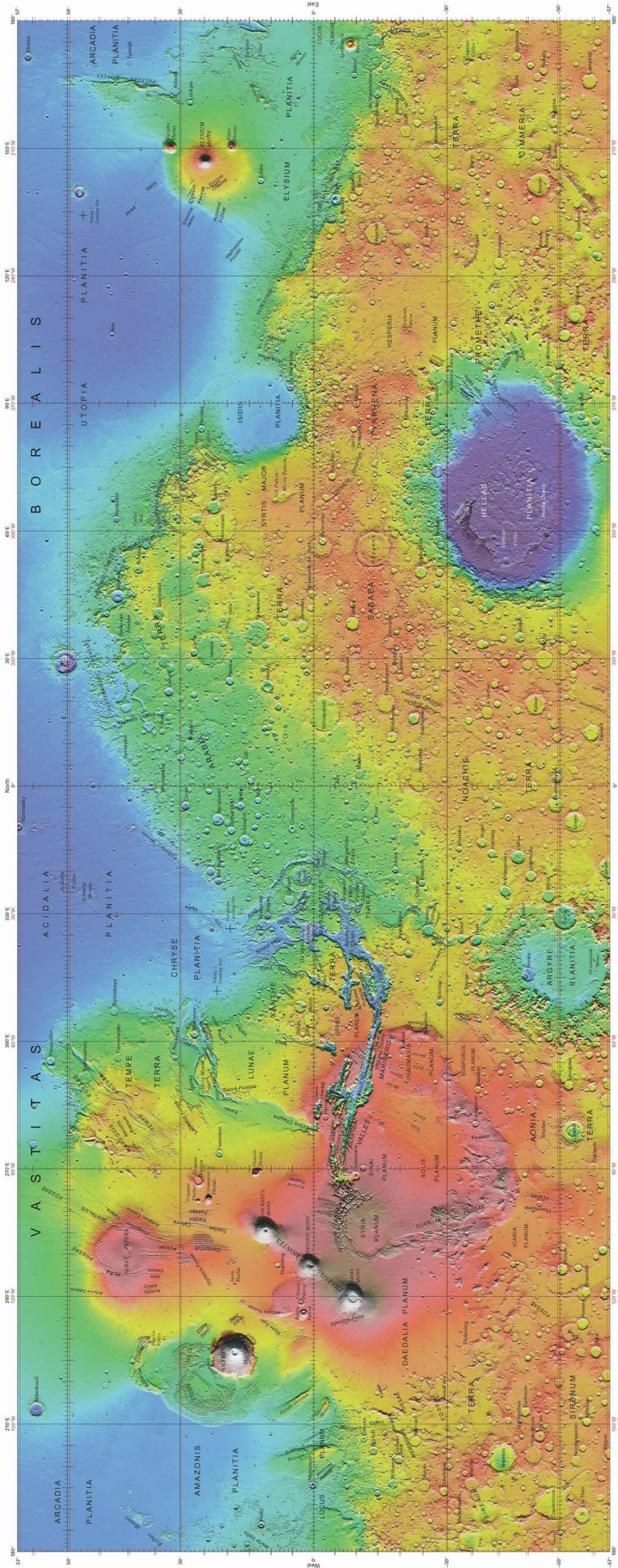


Figure 1.3: The altitude map of Mars produced by the MGS/MOLA instrument. The lowest altitudes are shown in blue (e.g. the Hellas basin) and the highest elevations in red (e.g. the Tharsis highland). Extreme values like on the volcanoes are displayed in white.

## 1.2 Open questions and future missions

Among the many open questions about the Red Planet those concerning the history of water are certainly the most intriguing, and water vapour is of course an important piece of this puzzle. Thus ultimately also this work, which will be described in the following chapters, tries to contribute to these issues:

- There are clear evidences of vast amounts of water flowing on the planet in the distant past. Where did it go?
- Did it go to the subsurface? If so, what is its contribution to the water cycle?
- What are the sinks and sources for the water cycle? Are the major contributors just the polar caps or are there other influencing areas on Mars?
- Is there a diurnal water cycle?
- How does the vertical distribution of water vapour look like?
- Is the seasonal cycle constantly repeating every year or does it experience variations?
- What does the microphysical interaction between the cycles of dust, carbon dioxide and water vapour look like?
- Is the H<sub>2</sub>O cycle closed in the present time or do we see an intermediate state between two obliquity extremes? What do these other climate states look like?
- Finally, on Earth we know: where is water, there is life. What about Mars?

The European *Mars Express* mission was partly designed to help answering these questions. However, also in the future missions will be sent to Mars to complete the puzzle, both robotic and manned (Zubrin and Wagner 1996). Regarding the near future, the American *Mars Reconnaissance Orbiter* continues where its predecessors have stopped. This powerful mission carries two instruments suitable for H<sub>2</sub>O mapping. The Mars Climate Sounder (MCS) is an infrared radiometer designed to study the atmosphere globally and continuously. The water will be sounded in two narrow thermal bands at 41.7 and 42.1  $\mu\text{m}$  (Read et al. 2006). Another onboard instrument is the spectrometer CRISM which will monitor the gas comprehensively in the 2.6  $\mu\text{m}$  band, similar to *Mars Express*'s OMEGA but with a higher spatial resolution (Wolff et al. 2006).

The next Mars lander *Phoenix*, set for touchdown in the north polar region between 65 and 70°N in May 2008 (late northern spring on Mars), will carry a meteorological package including a LIDAR that will not directly measure humidity but contribute significantly to the understanding of the polar environment (Tamppari and The Phoenix Team 2006).

Finally, in the near future ESA's *Herschel* infrared space telescope will be launched. Its HIFI instrument analyses sub-millimeter light between 480 and 1910 GHz at extremely high resolution and has the unique capability of probing the vertical distribution of water vapour directly from the spectral line shape (de Graauw et al. 2005).

## 1.3 Research objective

The history of space exploration – and especially the exploration of Mars – proved that plans are often not followed by reality. Therefore every available dataset is highly important for research. The Planetary Fourier Spectrometer (PFS) was originally designed to monitor water vapour and detect other trace gases. It covers several spectral bands of H<sub>2</sub>O which permits even the retrieval of its vertical distribution.

The continuous survey of atmospheric water is necessary in order to understand its behaviour and contribution to the questions listed above. Water vapour is also well suited for tracking of atmospheric motions because it is the most variable trace gas on Mars which enables the monitoring of atmospheric circulation, the formation of clouds, and interactions of water with the surface regolith and the polar caps. In the end, research about planetary atmospheres provides valuable information for comparative planetology, and – compared to the other planets – Mars' atmosphere is fairly similar to the terrestrial one.

In particular, the task of this work is the characterization of the seasonal water cycle on Mars in great detail, regarding both temporal and spatial resolution. Also a continuous coverage of the water behaviour should be provided that started with the American *Mars Global Surveyor* mission in 1999. Furthermore, possible sources and sinks of H<sub>2</sub>O need to be identified or confirmed, and the role of the polar caps for the cycle remains to be fully understood. Finally, the availability of a large dataset allows one also to look for other processes and correlations, for example a diurnal cycle or correlations with surface properties like albedo.

## 1.4 Outline

The work done to fulfill these mentioned research objectives is described in this thesis. It is structured as follows. After the very general introduction in this chapter a detailed description of the Martian atmosphere is given in chapter 2. The description includes basics about the composition and chemistry of the atmosphere, its structure, and the role of the carbon dioxide and the suspended dust. Then a short introduction into the physics of atmospheric dynamics is given in order to understand the underlying processes of the atmospheric circulation and phenomena on Mars. In the end of this chapter a brief outline of the evolution of the Martian climate is presented to understand the context of the present state.

Then chapter 3 (page 33) focuses on the atmospheric water vapour, in particular on the history of the measurements, both groundbased and from orbit, which have led to the understanding of the seasonal cycle as we know it. The rest of the chapter deals with the connection between the surface and the atmosphere, and its importance for the water cycle, especially its function as a reservoir which implicates a diurnal cycle of H<sub>2</sub>O.

Starting from chapter 4 all aspects of this work are described. In chapter 4 (page 45) the PFS instrument on *Mars Express* is explained, as well as its on-orbit performance and measurements. Chapter 5 (page 55) gives a detailed description of the applied method of data analysis using relative band depths. This includes the computation of the necessary synthetic spectrum and the treatment of the measured spectra, particularly the continuum

definition. At the end of this chapter (page 71) the involved uncertainties and their magnitudes are explained.

The results of this work are then presented in chapter 6 (page 79). They include the findings about the seasonal cycle, the spatial distribution (page 84) and the diurnal cycle (page 88). Furthermore, the comparison with the results of other instruments (page 101) yields interesting conclusions about the vertical distribution of water vapour (page 104).

Finally, chapter 7 (page 105) gives the conclusions from the work and a future outlook. The appendix of the thesis (page 109) is used for the description of relevant quantities and inputs like the European Mars Climate Database.

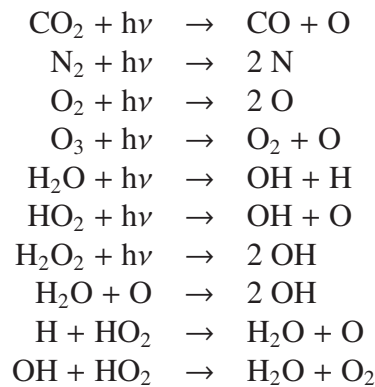
## 2 The atmosphere of Mars

### 2.1 Composition and chemistry

Not only the fundamental properties of Mars are different from Earth but also the atmosphere is quite different from the one of the blue planet. The mean surface pressure is 6.36 mbar while the average temperature lies at around 210 K whereas both undergo seasonal variations which will be described in section 2.3. The atmospheric constituents and their ratio per volume are listed in the following table, taken from Encrenaz et al. (2004) and Krasnopolsky (2006) where additional minor species and their upper limits are given, too. The sum of these gases yields a mean molecular weight of the atmosphere of 43.44 g/mol.

carbon dioxide (CO <sub>2</sub> )	=	95.32 %
nitrogen (N <sub>2</sub> )	=	2.7 %
argon 40 ( <sup>40</sup> Ar)	=	1.6 %
molecular oxygen (O <sub>2</sub> )	=	0.13 %
carbon monoxide (CO)	=	700 ppm
water vapour (H <sub>2</sub> O)	=	10 – 1000 ppm
molecular hydrogen (H <sub>2</sub> )	=	17 ppm
helium (He)	=	10 ppm
argon isotopes ( <sup>36+38</sup> Ar)	=	5.3 ppm
neon (Ne)	=	2.5 ppm
hydrogen-deuterium-oxygen (HDO)	=	0.85 ppm
krypton (Kr)	=	0.3 ppm
xenon (Xe)	=	0.08 ppm
ozone (O <sub>3</sub> )	=	0.04 – 0.2 ppm
hydrogen sulfide (H <sub>2</sub> S)	=	< 0.1 ppm
hydrogen peroxide (H <sub>2</sub> O <sub>2</sub> )	=	0.02 – 0.04 ppm
methane (CH <sub>4</sub> )	=	~ 0.01 ppm

Of course, some of these substances are also reacting chemically with each other. Especially since the atmosphere is bathed in solar UV radiation due to the absence of an ozone layer photochemistry plays a major role in the martian environment. Its influence increases towards the edge of the atmosphere where the photodissociation of molecules and the subsequent escape cause a permanent erosion of the atmosphere in direct interaction with the solar wind. A comprehensive list of reactions that are also altitude-dependent can be found in Krasnopolsky (2006). The most common chemical reactions and those with involvement of water are listed in the following table:



These reactions are just a small glimpse on the complexity of the chemical cycles on Mars that cannot be explained in detail because they are not part of this work. More important is the understanding of physical processes of the martian atmosphere. Therefore the basic knowledge about atmospheric physics is the subject of the rest of the chapter.

## 2.2 Structure of the atmosphere

Before the description of the martian atmosphere a general introduction to planetary atmospheres needs to be given. Most rocky bodies have basically no atmosphere or just a thin exosphere that is formed by the direct interaction of the solar wind with the surface. But if a body is massive enough it may hold a thicker atmosphere which is generally divided into several layers determined by the temperature profile of the atmosphere (Bauer 2001). These layers are called troposphere, stratosphere, mesosphere, and thermosphere and are separated by narrow transition regions called tropopause, stratopause, and mesopause. On top of the thermosphere there is also an exosphere where the mean free path of a gas molecule is larger than the scale height meaning that the likelihood of collisions is low enough that energetic atoms can escape into interplanetary space. Depending on the thermal structure of a planet the atmospheric layers are established in a specific way or even not present at all. Using Earth as a model a sort of idealized atmosphere can be described as follows.

The lowest part close to the surface is the troposphere where the structure is governed by radiation and convection whereas the solar energy deposited onto the surface is the heat source. In a theoretically dry atmosphere the temperature profile is determined by adiabatic thermodynamic processes and described by the adiabatic lapse rate  $\Gamma_d$  (with  $T$  the temperature,  $z$  the altitude,  $g$  the gravity acceleration and  $c_p$  the specific heat capacity at constant pressure):

$$\Gamma_d = \frac{dT}{dz} = -\frac{g}{c_p} \quad (2.1)$$

In reality this ideal behaviour is modified by the presence of water vapour because during its condensation there is a release of enthalpy<sup>1</sup> which delays the adiabatic cooling of a rising air parcel. Therefore the saturated adiabatic lapse rate is always smaller than the

---

<sup>1</sup>The term enthalpy is used to replace the older term latent heat. Enthalpy  $L$  is defined as  $L = U + p \cdot V$  with the internal energy  $U$ , the pressure  $p$  and the volume  $V$ . Using  $L$  the specific heat capacity is defined as  $c_p = \partial L / \partial T$ .

dry one. Modelled temperature profiles for Mars are shown in figures 2.2 and 2.3 for illustration. Another useful quantity for the description of an atmosphere is the altitude-depending scale height

$$H(z) = \frac{R \cdot T(z)}{\bar{m} \cdot g} \quad (2.2)$$

with the gas constant  $R$  and the mean molecular mass of the atmosphere  $\bar{m}$ .  $H(z)$  describes the altitude difference at which the pressure has fallen to  $1/e$  of the reference value.

The troposphere is separated from the next upper region by the tropopause where the convection ceases to be the driving mechanism as the atmosphere becomes vertically stable and radiation processes begin to dominate. Particularly on Earth the next layer is very pronounced: the stratosphere. Here the temperature increases with height due to absorption of solar UV radiation by ozone until a maximum temperature which defines the stratopause.

Above this temperature inversion follows the mesosphere whose decreasing or constant thermal profile is determined mainly by radiation balance. The minimum temperature is reached at the mesopause. Further upwards there is the thermosphere which is governed by solar radiation and consequently ionization processes. This leads to an increasing temperature profile again that saturates at the constant exospheric temperature.

In contrast to this described model atmosphere Mars has certain peculiarities of its atmosphere. The most characteristic feature of the lower martian atmosphere is the airborne dust whose amount in the air can vary significantly within and between martian years. Unlike the water vapour that has only marginal influence on the adiabatic lapse rate due to its tiny amount the dust plays an important role. Because of its absorption of solar and surface radiation in the visible and infrared spectrum the dry adiabatic lapse rate of  $\Gamma = 4.5 \text{ K/km}$  is hardly ever followed which makes the martian atmosphere vertically more stable by reducing or even inverting the temperature gradient (Zurek 1992). Such a temperature inversion is reached for a dusty atmosphere during the night when the atmosphere stays warm but the surface cools off rapidly. The same effect takes place at a planet-wide scale in the case of a global dust storm. Therefore the martian lower atmosphere up to  $\sim 45 \text{ km}$  is somehow a mixture of the terrestrial troposphere because of the surface as its boundary and the adiabatic lapse rate at dust-free conditions and the terrestrial stratosphere because of the heating effect of suspended dust.

However, such an Earth-like stratosphere does not exist on Mars because of the absence of an ozone layer. Although ozone is produced from  $\text{O}_2$  and  $\text{O}$  it gets quickly destroyed again by reactive molecules (Perrier et al. 2006). Finally, the mesosphere ( $\sim 45$  to  $\sim 110 \text{ km}$  in altitude), mesopause, and thermosphere (above  $\sim 125 \text{ km}$ ) of Mars are in principle similar to the described model atmosphere (Zurek 1992).

## 2.3 Dust and CO<sub>2</sub> cycle

Another outstanding characteristic of the martian climate are the presence of seasonal cycles of carbon dioxide, dust, and water. The latter one and its coupling with the other cycles will be described in detail in chapter 3.2. The importance of dust for atmospheric heating was emphasized in the previous section. Yet it needs to be mentioned that there is a constant redistribution of dust happening, primarily by dust storms. These can be

categorized into local or regional ones which can take place principally every year with different intensities and into global storms which enshroud the entire planet but occur irregularly every few martian years. Those storms generally originate in spring or summer of the southern hemisphere in the subtropics why this region can be considered as a source region. For dust sinks the most likely candidates are the northern polar cap and the northern low latitude areas neighbouring Syrtis Major (Kahn et al. 1992). In local regimes dust redistribution is done by dust devils as was impressively witnessed by the Mars Exploration Rover *Spirit*, driving in Gusev crater (14.6°N, 175.5°E). The effect of the storms on the surface is a change of albedo due to dust layers of a few tens of micrometers thickness being deposited on or lifted from the ground.

The carbon dioxide cycle was directly measured by both *Viking* landers for the first time and impressively shows a yearly pressure variation with double peaks (Tillman 1988). Driven by the seasonally changing insolation the cycle is caused by the deposition of carbon dioxide during polar winters and subsequent sublimation in springtime. Since CO<sub>2</sub> is the main atmospheric constituent the effect is a loss of atmospheric mass of 25% to 30% in case of the southern polar night. Because it coincides with the aphelion position of Mars this season is long and the temperatures fall below the condensation temperature of about 148 K (for the martian air pressure). The effect of this atmospheric mass change is shown in figure 2.1 where the pressure records of both *Viking* Landers (VL-1 and VL-2) are displayed versus time, given in sols. On the top of the panel the time is also given in solar longitude. The sublimation of CO<sub>2</sub> from the south pole cap is evident between southern winter (L<sub>S</sub>=140°) and spring (L<sub>S</sub>=230°) where the ground pressure rises by more than 2 mbar. The offset between the two landers is due to the different locations on Mars.

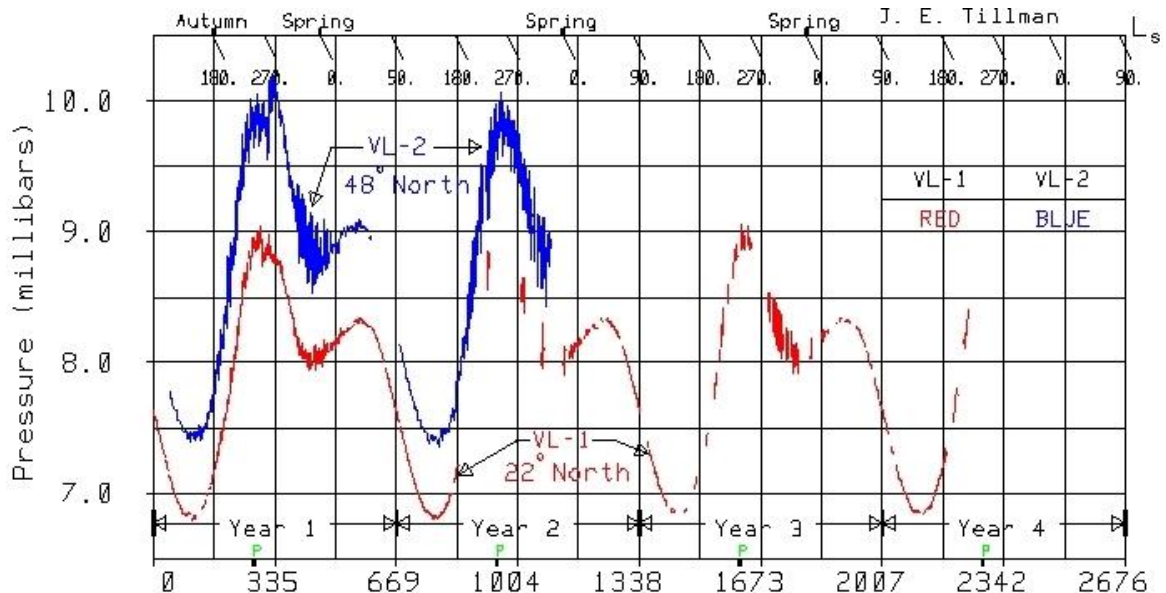


Figure 2.1: The Viking pressure records (adopted from Tillman (1988)): the lower panel shows the daily average pressure [mbar] versus the time in sols for both *Viking* Landers. The seasonal variations are clearly visible.

The governing equation to determine the mass sublimation/deposition rate per unit area is (Read and Lewis 2004):

$$\frac{\partial M_C}{\partial t} = \frac{1}{L_C} \cdot \epsilon \sigma T_C^4 \quad (2.3)$$

with  $M_C$  the mass of the condensate (CO<sub>2</sub> or H<sub>2</sub>O),  $L_C$  the corresponding enthalpy of sublimation,  $\epsilon$  the emissivity,  $\sigma$  the Stefan-Boltzmann constant and  $T_C$  the condensate's temperature. Other reservoirs in the cycle which play just a minor role are CO<sub>2</sub> clouds because of their limited quantity and the regolith which is of relevance only over long time scales (James et al. 1992). Despite more recent observations with the *Mars Global Surveyor* and *Mars Odyssey* orbiters there are still many questions unanswered regarding the CO<sub>2</sub> cycle, e.g. the detailed physics of the CO<sub>2</sub> deposits and the influence of surface properties (James et al. 2005).

An example for a typical temperature and pressure profile for Mars up to an altitude of 120 km over the local surface is shown in figure 2.2. The profiles were created by the European Mars Climate Database EMCD v4.1 (explained in appendix A.3) for 6 locations of the *Mars Express* orbit number 68 (solar longitude 342.5°):

- solid: longitude -104.2°, latitude -61.08°, altitude 1.8 km
- dotted: longitude -104.3°, latitude -29.97°, altitude 6.2 km (Tharsis plateau)
- dashed: longitude -104.5°, latitude 11.04°, altitude 16.7 km (Ascraeus Mons)
- dash-dot: longitude -103.3°, latitude 45.16°, altitude 1.2 km
- dash-dot-dot: longitude -100.8°, latitude 60.04°, altitude -2.7 km
- long dash: longitude -79.2°, latitude 80.06°, altitude -4.9 km (Vastitas Borealis)

Clearly the temperature and pressure shows a wide variety of profiles which have to be respected in any retrieval of atmospheric parameters.

Naturally the temperature varies in the course of a martian day (sol). For local times 0 h, 4 h, 8 h, 12 h, 16 h and 20 h at the longitude -16.6° and latitude 45.7° during  $L_S=15^\circ$  the profiles for the lower 5 km are displayed in figure 2.3. There the temperature changes including the inversion at nighttime are clearly visible while the pressure is basically stable during one sol. The main reason for the strong temperature variations compared to Earth is the low thermal inertia of the surface. On Earth the oceans buffer a lot of energy which makes the atmospheric temperature variations less pronounced.

## 2.4 Atmospheric physics

This chapter gives a brief introduction into the field of atmospheric dynamics which is necessary to understand the relevant processes that govern the distribution of air masses in the martian environment. In general, dynamical phenomena in an atmosphere can be classified by the relationship of their horizontal to their vertical scale and their Rossby number that relates the horizontal angular motion of the phenomenon with the Coriolis motion of the reference frame. The Rossby number is defined as  $Ro = \frac{V}{L \cdot f}$  with  $V$  and  $L$  the characteristic velocity and length scale for the dynamic phenomenon and  $f = 2\Omega \sin \phi$  the Coriolis parameter at latitude  $\phi$  of the planet rotating with an angular speed  $\Omega$ . So if  $Ro \ll 1$  this means that the planetary rotation is the dominating process and the dynamical

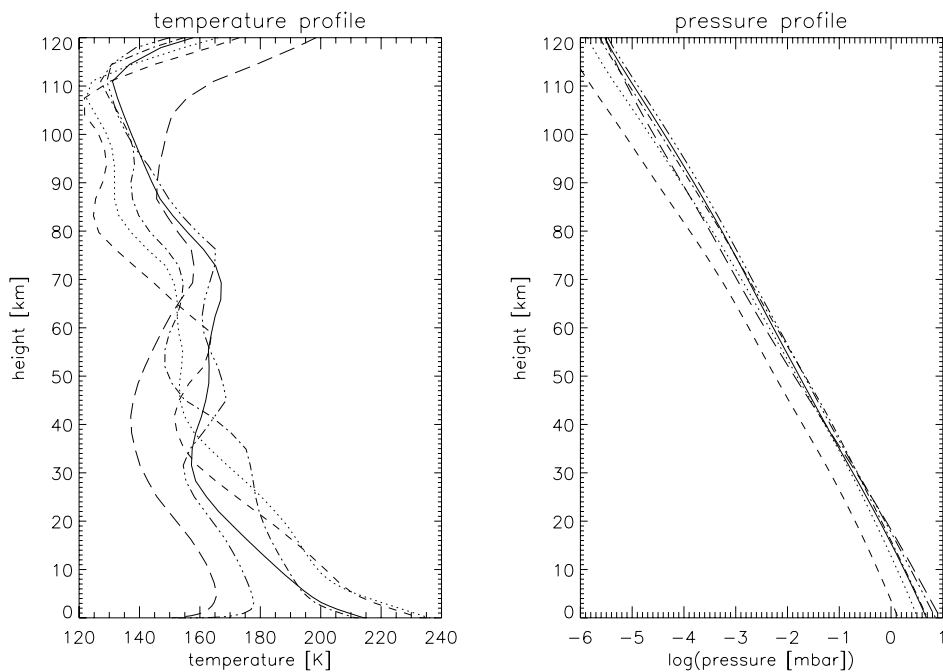


Figure 2.2: The temperature and logarithmic pressure profiles for 6 locations of *MEX* orbit 68: lat= $-61.08^\circ$  (solid), lat= $-29.97^\circ$  (dotted), lat= $11.04^\circ$  (dashed), lat= $45.16^\circ$  (dash-dot), lat= $60.04^\circ$  (dash-dot-dot), lat= $80.06^\circ$  (long dash). For more explanations see text.

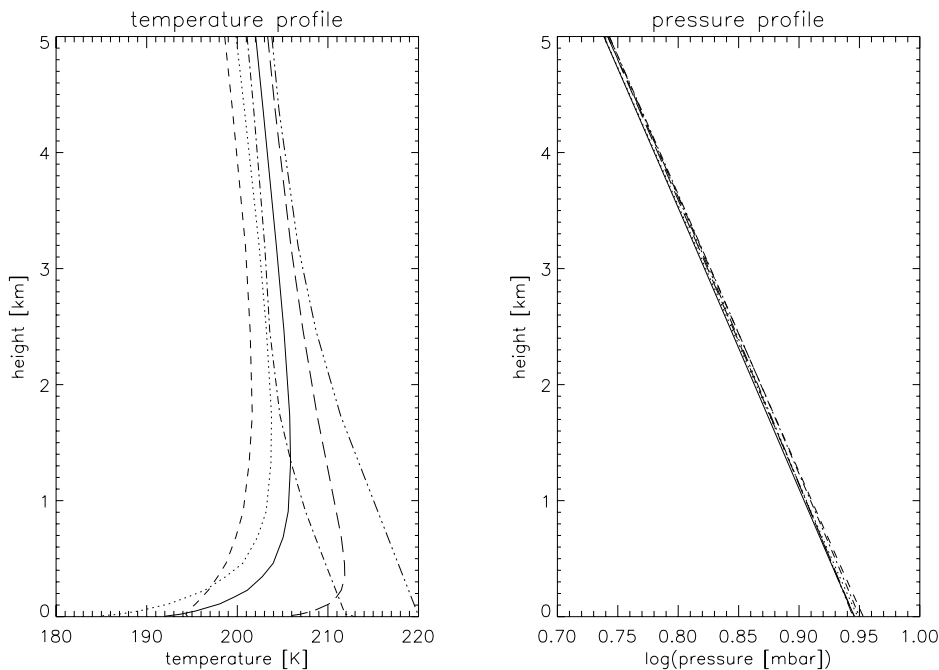


Figure 2.3: Temperature and logarithmic pressure profiles for the lower 5 km at longitude  $-16.6^\circ$  and latitude  $45.7^\circ$  during  $L_S=15^\circ$  and at different times of the day: solid: 0 h, dotted: 4 h, dashed: 8 h, dash-dot: 12 h, dash-dot-dot: 16 h, long dash: 20 h.

systems are of planetary scale while for  $Ro \gg 1$  the rotation of the planet is negligible which is valid for small scale phenomena of the boundary layer. Consequently in between there is a mesoscale with  $Ro \approx 1$  which is accountable for atmospheric systems like thunderstorms on Earth. In the following the very basic underlying physical processes and the peculiarities of Mars are described.

In this context the velocity vector  $\mathbf{V}$  of a considered air parcel is separated into its three components: the zonal wind  $u$  in east–west direction, the meridional wind  $v$  in north–south direction and the vertical wind  $w$ .

### 2.4.1 Large scale dynamics

The driving force of any dynamics of a planetary atmosphere is the insolation from the central star. The amount of energy from the sun changes naturally in the course of the day and the year and is different for each location on the planet. Yet there is a long-term radiation equilibrium which determines the blackbody temperature of the planet. As the sun has its emission maximum in the visible light the bulk of absorbed radiation is of short wavelength which has to be balanced by the emitted infrared radiation:

$$4\pi R^2 \sigma T^4 = (1 - A) F_S \pi R^2 \quad (2.4)$$

Here  $R$  is the planet's radius,  $T$  the blackbody temperature,  $A$  the albedo and  $F_S$  the incident solar flux on the planet. For a detailed description of an atmosphere things get more sophisticated, of course. Because of solar forcing parcels of air are locally set in motion and are distributed throughout the atmosphere and with them the gaseous water. Therefore  $H_2O$  acts as a tracer for atmospheric processes, too.

To understand a dynamic system one has to have a look on the behaviour of a parcel of air in the atmosphere under the influence of the acting forces. The basic equation of hydrodynamic motion derived from the Navier-Stokes equation is for a moving reference frame (Houghton 2002):

$$\frac{D\mathbf{V}}{Dt} = -2 \cdot \mathbf{V} \times \boldsymbol{\Omega} - \frac{1}{\rho} \nabla p + \mathbf{g} + \mathbf{F} \quad (2.5)$$

The formula describes the velocity  $\mathbf{V}$  of an air parcel under the influence of the Coriolis force of a rotating planet with angular velocity  $\boldsymbol{\Omega}$  and gravity  $\mathbf{g}$ , and in the presence of a pressure gradient  $\nabla p$ . Explicitly the gravity also includes the centrifugal term due to the rotation of the frame, so  $\mathbf{g} = \mathbf{g}' - \boldsymbol{\Omega} \times (\boldsymbol{\Omega} \times \mathbf{r})$  with the gravitational acceleration  $\mathbf{g}'$  at the location  $\mathbf{r}$ . The additional term  $\mathbf{F}$  describes the forces due to friction and will be neglected for large systems that are weakly influenced by surface inhomogenities. Furthermore, for large scale horizontal dynamics vertical motions are negligible. So equation 2.5 can be simplified into the following form describing horizontal motions with the Coriolis parameter  $f=2\Omega \sin \phi$  and with  $\mathbf{k}$  the unit vector, pointing in the opposite direction of  $\mathbf{g}$ :

$$\frac{D\mathbf{V}}{Dt} = f \cdot \mathbf{V} \times \mathbf{k} - \frac{1}{\rho} \nabla p \quad (2.6)$$

Starting from this equation there are two further approximations possible. The first one assumes very small accelerations of the considered air parcels ( $D\mathbf{V}/Dt \approx 0$ ). Arising from

the balance between Coriolis force and pressure gradient this so-called geostrophic flow has the velocity

$$\mathbf{V}_g = \frac{1}{\rho \cdot f} \mathbf{k} \times \nabla p$$

in parallel to the isobars and causes in the northern hemisphere a counterclockwise rotation around centers of low pressure (cyclones) and a clockwise rotation around high pressure centers (anticyclones). The applicability of the geostrophic approximation can be determined by the ratio of the left-hand side of equation 2.6 to its Coriolis term (both time integrated) which yields the above mentioned Rossby number. The smaller it is for a dynamic system the more correct is its geostrophic description.

The second approximation is called cyclostrophic wind and is applicable for large storms such as hurricanes on Earth. Despite the extent of such storms the Coriolis force is still relatively small compared to the force due to the pressure gradient. The wind speed magnitude for the accelerated air parcels is calculated as given in Salby (1996):

$$V_c = \sqrt{\frac{R}{\rho} \cdot \frac{\partial p}{\partial R}}$$

with  $R$  the distance to the center of the dynamic system which is always a low pressure system. Of course the same formula describes also smaller systems like dust devils or tornadoes.

An effect influencing the geostrophic motion are thermal winds caused by temperature differences along isobars. The result is a vertical shear of the geostrophic wind described by

$$-\frac{\partial \mathbf{V}_g}{\partial \ln p} = \frac{R}{f} \cdot \mathbf{k} \times \nabla_p T$$

whose net difference  $\Delta \mathbf{V}_g$  across a layer with a certain pressure change is called thermal wind (Salby 1996). An example for it are the jet streams on Earth. They originate from a strong meridional temperature contrast during northern summer which causes stronger eastward winds with increasing height (decreasing pressure). For Mars at different seasons the left panels of figures 2.4 (vernal equinox), 2.5 (northern summer) and 2.6 (southern summer) show the zonal winds, where the strong positive values depict westwind jets.

As for atmospheric waves the largest ones are planetary waves (or Rossby waves) that are driven by the variation of the Coriolis force with latitude. In a simplified form with constant air density and a mean zonal wind  $\bar{u}$  the absolute vorticity is conserved. It is defined as the combination of both the relative vorticity of the dynamic system<sup>2</sup> and the one of the planet's rotation, given by the Coriolis parameter  $f$ . So if – in the northern hemisphere – a rotating air parcel that moves towards east is displaced southward the smaller planetary vorticity  $f$  excites a faster counter-clockwise circulation of this system. Hence the air in front of the system is moved northward which causes a northward deflection of the air parcel, as well. Vice versa a clockwise circulation will move a northward deflected system back to the south. The solution of the equation of absolute vorticity conservation

$$\frac{D(\zeta + f)}{Dt} = 0 \quad \text{with} \quad \frac{D}{Dt} = \frac{\partial}{\partial t} + \bar{u} \frac{\partial}{\partial x} \quad (2.7)$$

---

<sup>2</sup>In general: the vertical component of the circulating velocity field  $\zeta = \partial v / \partial x - \partial u / \partial y$ .

yields the fact that Rossby waves always propagate westward relative to the basic flow  $\bar{u}$ , with speeds of a few meters per second (Houghton 2002). They have been confirmed in-situ, e.g. by the *Viking 2* lander (48.0°N, 134.3°E) finding transient waves with periods of 3 and 6–8 days (Barnes 1980). A peculiarity of Mars in this respect are the presence of stationary planetary waves caused by topography or albedo and thermal inertia differences of the surface. This phenomenon has been detected by spacecraft (Banfield et al. 2003) and is confirmed in atmospheric circulation models (Read and Lewis 2004).

Another global wave phenomenon which is especially evident for Mars are thermal tides which were observed by the *Viking* (Zurek et al. 1992) and *Pathfinder* landers (Read and Lewis 2004). The amplitude between day and night temperature differences can reach up to 100 K. Because the surface has a very low thermal inertia it is unable to store large quantities of heat and is therefore responsive to solar heating. Thus a temperature maximum migrates around the planet in the course of a day following the sub-solar point. A diurnal and also semi-diurnal tide is established which can be seen in phase-shifted maxima and minima of pressure and wind, as well.

At last, when looking at the net solar heating one will find mechanisms for global redistribution of airmasses. For moderately inclined planets the equatorial regions receive on average radiative heating while higher latitudes maintain the global energy balance (equation 2.4) through radiative cooling. Hence there must be a mechanism to transfer the heat poleward. The basic principle of this Hadley circulation is in most cases thermal forcing. This means that air which rises at the point of highest integrated sunlight, moves meridionally in the high troposphere and sinks down in regions outside the tropics. For the poleward moving air parcels under baroclinic conditions<sup>3</sup> the planetary rotation causes a geostrophic deflection. In addition, the meridional temperature gradient infers a thermal wind.

The complete interplay of all above described dynamics together with the transformations of potential, kinetic and thermal energy among each other and into frictional loss is called general circulation. For Mars Jakosky and Haberle (1992) depicts it as follows. The dominating feature of the martian troposphere is the Hadley cell being responsible for overturnings that are much larger in extent than on Earth due to the lack of a tropopause and can reach altitudes of up to 60 km (Read and Lewis 2004). Unlike the terrestrial cell the martian cell is more dependent on the season and dust content of the air. For example during dust storms the Hadley circulation gets more intense and stretches further towards the poles (Zurek et al. 1992) which in turn influences the water cycle. Now on the one hand, at equinox seasons there are two Hadley cells established per hemisphere together with weak Ferrel cells in the poleward areas (opposite circulation; driven by mechanical forcing). Figure 2.4 shows an average of zonal winds (left panel) and the mean meridional winds (right panel) for  $L_S=0-30^\circ$ . The Hadley cells become visible after the meridional winds are vertically integrated from top of the atmosphere to the bottom forming the so called mass stream function (not explicitly shown). On the other hand, during the times around solstices a single large Hadley cell develops that is much more intense than the equinox cells and whose rising branch lies at very high latitudes in the summer hemisphere. Such a cell even crosses the equator and can thus transport airmasses be-

<sup>3</sup>An atmosphere where layers of constant temperature intersect layers of constant pressure is called baroclinic; an atmosphere with constant temperature and pressure stratification is called barotropic.

tween the hemispheres. However, the big orographic difference and orbital eccentricity of Mars are strongly influencing the mere amount of transported air and hence its water content. Figures 2.5 and 2.6 show the atmospheric dynamics conditions at  $L_S=90-120^\circ$  and  $L_S=270-300^\circ$ , respectively. The southern summer cell is by a factor of 2 more intense than the northern summer cell.

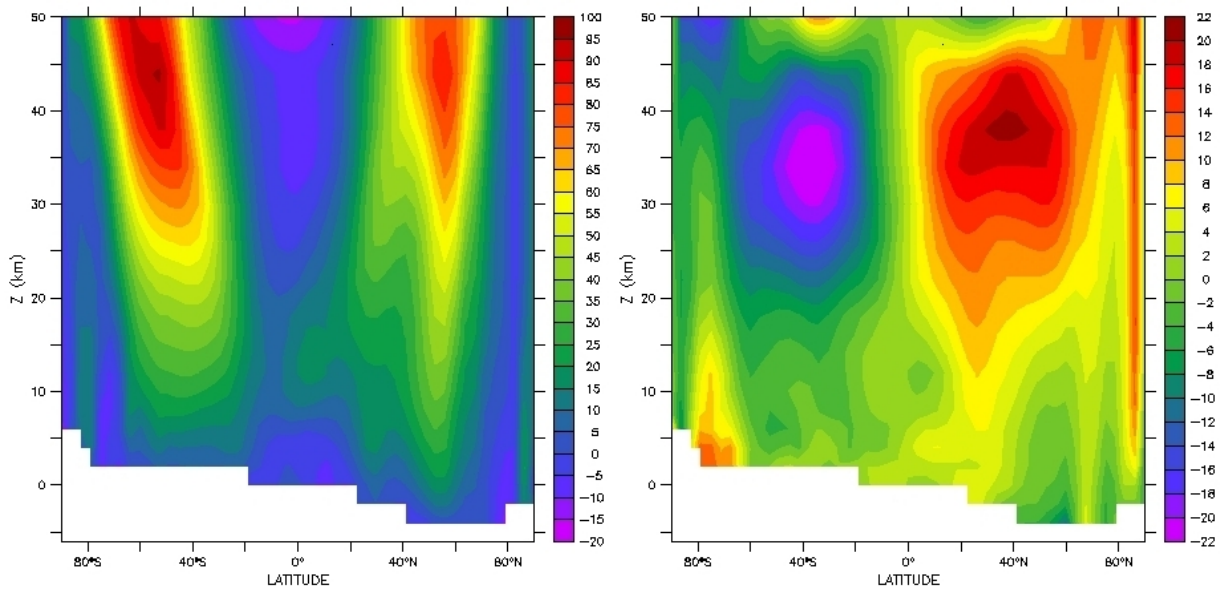


Figure 2.4: Mean zonal wind (left) and mean meridional wind (right) at  $5.6^\circ\text{W}$  longitude for  $L_S=0-30^\circ$ , given in [m/s]. The zonal wind is positive when oriented west- to eastward and the meridional wind is positive when flowing from south to north. (created with EMCD 4.1)

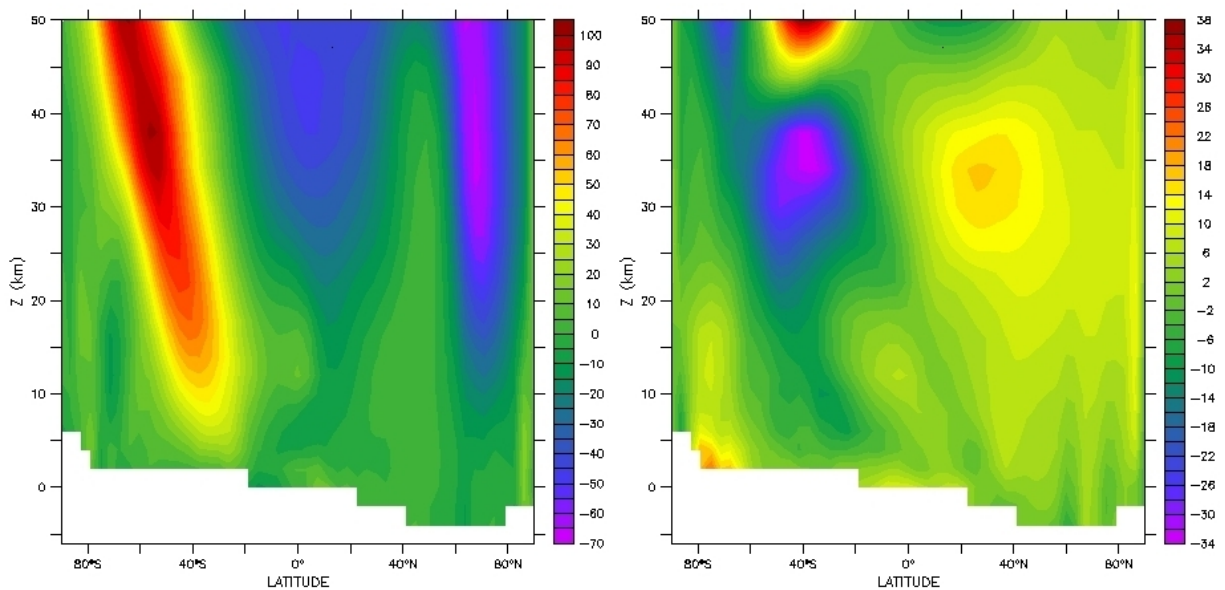


Figure 2.5: Mean zonal wind (left) and mean meridional wind (right) for  $L_S=90-120^\circ$ , given in [m/s]. (created with EMCD 4.1)

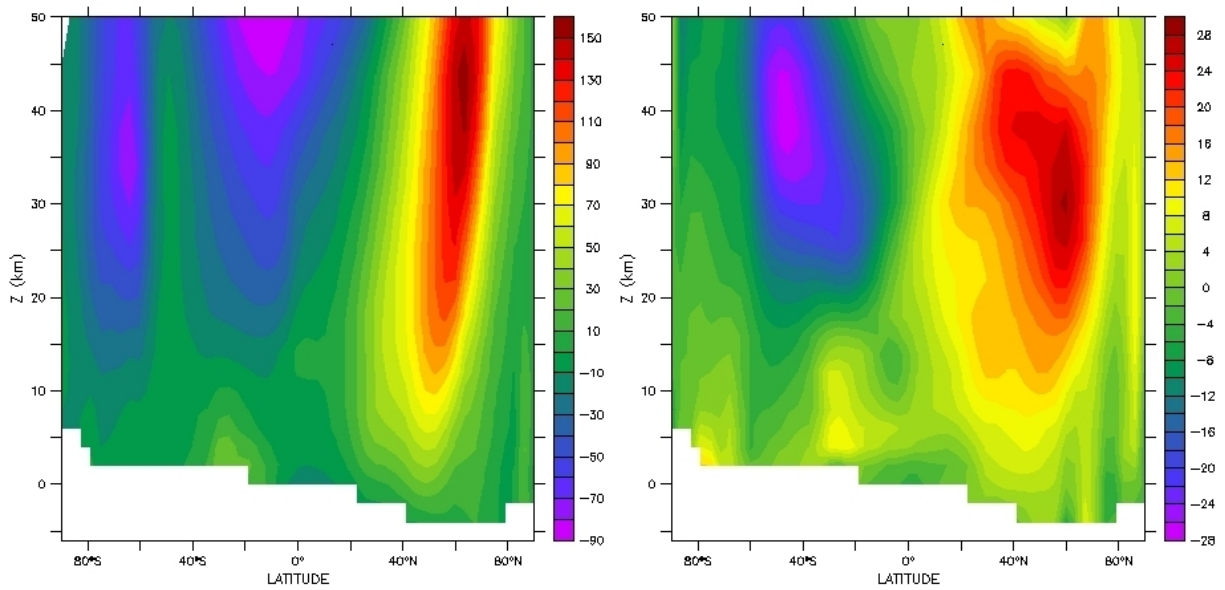


Figure 2.6: Mean zonal wind (left) and mean meridional wind (right) for  $L_S=270\text{--}300^\circ$ , given in [m/s]. (created with EMCD 4.1)

Of course the atmospheric dynamics are modulated by the steadily present thermal tides under the sub-solar point, planetary waves and geostrophic winds at higher latitudes. Finally there is a phenomenon unique for Mars: the deposition/sublimation flows on the polar caps characteristic for the  $\text{CO}_2$  cycle. A more detailed description of it will be given in the next section.

### 2.4.2 Effects on mesoscale and small scales

For dynamics at smaller than global scales the planetary rotation can be neglected. One aspect of lower atmospheric motions are so-called gravity waves. Their restoring force is buoyancy and due to their short timescales the friction term of equation 2.5 is neglected, too. Their most common appearance are lee waves downstream of topographic disturbances like mountains or crater rims of which Mars has plenty. The induced oscillation might be visible by cloud formation when the humid air is lifted upwards into colder levels and condenses. Gravity waves are important for the connection between the surface, the lower and the upper atmosphere because they transport energy upwards (Houghton 2002).

A feature typical for the martian atmosphere is the baroclinic wind between the cold polar caps and the surrounding warmer surface, an effect comparative to the sea-breeze on Earth. The martian polar caps serve as cold traps in autumn and as reservoirs in spring for up to 30% of the atmosphere's  $\text{CO}_2$  which causes additional meridional mass flow. In southern spring this baroclinic wind, estimated by Read and Lewis (2004) to be in the order of 0.2–0.5 m/s, enhanced by Coriolis forces, is the most likely cause for frequent dust storms originating in the southern hemisphere during that season (Zurek et al. 1992). In addition, because the polar caps are a water reservoir this kind of wind is important for understanding the  $\text{H}_2\text{O}$  cycle. At last, a similar mechanism is also feasible as a local circulation between areas with large topographic differences or regions of strong albedo and

thermal inertia contrast. For example the "thermal continents" of the Tharsis highlands and Arabia Terra have a very high albedo and low thermal inertia.

So far in the description of air flows there was no consideration of instabilities and turbulences which are of course present in real atmospheres. A so-called barotropic instability has its origin in the latitudinal non-uniformity of the zonal wind that was assumed constant ( $\bar{u}$ ) in the description of planetary waves (equation 2.7). A baroclinic wave is the most common form of atmospheric instabilities, especially in mid-latitudes where cyclones are formed. A more detailed description of these instabilities can be found in Houghton (2002) who also states the typical wavelength for a baroclinic wave as:

$$\lambda = \frac{2\pi \cdot H}{1.61 \cdot f} \cdot \sqrt{g \cdot \frac{1}{T} \left( \frac{dT}{dz} + \Gamma_d \right)}$$

Under martian conditions the values for the scale height  $H$ , the Coriolis parameter  $f$ , gravity  $g$ , temperature  $T$  and lapse rates yield wavelengths of a ~4000 kilometers (equal to periods of a few days for a mean zonal wind of 10-20 m/s (Zurek et al. 1992) like observed by the *Viking* landers).

Finally, the smallest scale phenomena are taking place in the boundary layer of an atmosphere where the energy of larger scale dynamics is dissipated by small-scale turbulence<sup>4</sup>. On Earth in this lowest kilometer of the atmosphere about half of the total kinetic energy is dissipated by friction (Salby 1996). The friction is responsible for turbulent transfer between the surface and the atmosphere which is especially important for water vapour stored in the ground (cf. chapter 3.3). A vertical flow in the boundary layer is established because of flux continuity between a constant geostrophic flow on top of the boundary layer and a horizontally convergent flow at the surface. This process is called Ekman pumping and the vertical wind speed  $w$  is given in Houghton (2002) by:

$$w = \frac{1}{2} \zeta \cdot \sqrt{\frac{2K}{f}}$$

with  $\zeta$  the vorticity of the geostrophic wind and  $K$  the eddy viscosity coefficient. Thus for northern hemisphere cyclones (low pressure system) with positive vorticity the boundary layer is pushed upwards by a positive  $w$  in the order of several mm/s. Vice versa it is pushed downwards in high pressure systems. This process is also observed on Mars where the boundary layer grows to heights of 5–15 km during the daytime convection and shrinks to a shallow layer during the night. Within this layer water vapour is equally mixed by turbulent eddies (Jakosky and Haberle 1992).

## 2.5 Evolution of the climate

Thanks to the observations of *Mars Express* (Bibring et al. 2006) and the findings of the *Mars Exploration Rovers* (Squyres et al. 2004) the climate history and the role of water could be rewritten and refined. It is currently understood as follows. Despite a warm

---

<sup>4</sup>The Reynolds number, defined as  $Re = (L \cdot V)/\nu$  with  $L$  the length scale,  $V$  the velocity and  $\nu$  the viscosity, differentiates between turbulent ( $Re$  greater than approx. 6000) and laminar flow.

and wet climate in the first few hundred million years Mars is basically a cold and dry desert since at least the last three billion years. The identification of minerals formed or altered by water permits a new definition of epochs on Mars. The phyllosian period (dominated by clays) and the theikian period (dominated by sulfates) are much shorter than the Noachian and Hesperian, respectively. And already 3.5 billion years ago the siderikian epoch started which lasts until today and is characterized by anhydrous iron oxides and the absence of major amounts of liquid water on the surface. That long-lasting dry state is interrupted only by short phases of more humid conditions caused by orbital mechanics and the lack of a massive moon that could stabilize Mars' rotational axis. Evidence for these wetter phases comes from geologically young ice formations (Head et al. 2005) that had evaporated if there was only a long dry climate predominating (Kossacki et al. 2006). Also the layered deposits surrounding the residual polar caps lead to the conclusion that a combination of changing orbital eccentricity and obliquity of the rotational axis affect the insolation conditions on Mars dramatically over several  $10^6$  years (Laskar et al. 2002). This in turn could cause a redistribution of ice from the poles to the equator and back and would mean a completely different water cycle and different climate in general (cf. Read and Lewis (2004)).

Furthermore, because of its low abundance in the present the atmospheric water is certainly not the answer to the question where all the water has gone that must have existed on Mars after its formation. The polar caps, ice which is possibly locked in the subsurface and atmospheric sputtering are much better explanations (Lammer et al. 2003). Still, water vapour is of major importance for the climate of Mars. Not only does  $H_2O$  influence the atmospheric chemistry and form fog and clouds but it is also the most variable trace gas and shows interaction with the ground: in interplay with  $CO_2$  fascinating features on the poles are created, ground ice could be observed both from orbiters and from landers and its adsorption in the regolith is not negligible. The role of water vapour on Mars will be subject of the next chapter.



# 3 Water vapour on Mars

## 3.1 History of H<sub>2</sub>O observations

### 3.1.1 Spacecraft exploration

In the history of the exploration of Mars the question of water vapour was always of greatest interest due to its importance for the climate. After initial groundbased observations in the spectrum around 8200 Å in the early 1960's reported by Spinrad et al. (1963) and Kaplan et al. (1964) a more thorough investigation had become feasible with the advent of the space age. The first spacecraft sent by the Soviet Union and the USA were therefore also carrying instruments to search for water vapour. Because the efforts of the Soviet engineers and scientists did not bear fruits the first orbital measurements of H<sub>2</sub>O in the martian atmosphere was performed by the American *Mariner 9* probe with its IRIS instrument, a Michelson interferometer operating between 200 and 2000 cm<sup>-1</sup>. Using the rotational lines<sup>1</sup> between 250 and 330 cm<sup>-1</sup> it confirmed the earlier ground-based measurements of a mean column density<sup>2</sup> of 10 to 20 pr. µm during the bulk of the martian year and of about 30 pr. µm during the northern spring (Hanel et al. 1972, Conrath et al. 1973).

Shortly after that also the Soviet scientists announced similar findings by the *Mars 3* orbiter using a narrow-band photometer centered around 1.38 µm (Moroz and Ksanfomaliti 1972, Moroz and Nadzhip 1975). Operating at the same time like *Mariner 9* between L<sub>S</sub>=311° and L<sub>S</sub>=358° a lower column density of only a few pr. µm up to 20 pr. µm was reported. However, this might have been due to the giant dust storm engulfing the planet at this time and the use of a different spectral band than the American instrument.

Yet the groundbreaking dataset was provided by the MAWD spectrometer onboard the *Viking 1* orbiter that arrived at Mars in 1976. It was operating for more than one martian year while the one on *Viking 2* could not be used at all. MAWD was a grating spectrometer with five channels centered at 1.38 µm and a spectral resolution of 1.2 cm<sup>-1</sup>. The main result from this instrument was the coverage of the entire seasonal cycle on Mars showing variations between roughly 0 and 100 pr. µm with a global average of 6 to 13 pr. µm. Based on this an exchange of vapour with regolith reservoirs was suggested, as well as a net transport from north to south by global circulation (Jakosky and Farmer 1982). This dataset has provided the basis for the understanding of water vapour for an entire generation of scientists (Jakosky and Haberle 1992). Even today its analysis with modern tools yields new insights into the martian atmosphere, such as the importance

---

<sup>1</sup>For the description of relevant water absorption bands see appendix A.2.

<sup>2</sup>The definition of H<sub>2</sub>O measurement units (column density and mixing ratio) is given in appendix A.4.

of light scattering of aerosols on the retrieved water amount for observation geometries with airmasses higher than 3 to 4 (Fedorova et al. 2004). The quantity "airmass" is a measure for the pathlength through an atmosphere and will be explained in chapter 5.3.2 (page 61). A comparison of the original results of MAWD with these newly analysed ones is presented in figure 3.1. There the true water amount in southern summer is masked by the dusty atmosphere which resulted in lower values after the original processing of measurements with airmasses higher than 3. Between  $L_S=200^\circ$  and  $300^\circ$  the effect is significant with a corrected maximum of over 20 pr.  $\mu\text{m}$  versus 10 pr.  $\mu\text{m}$  in the original retrieval.

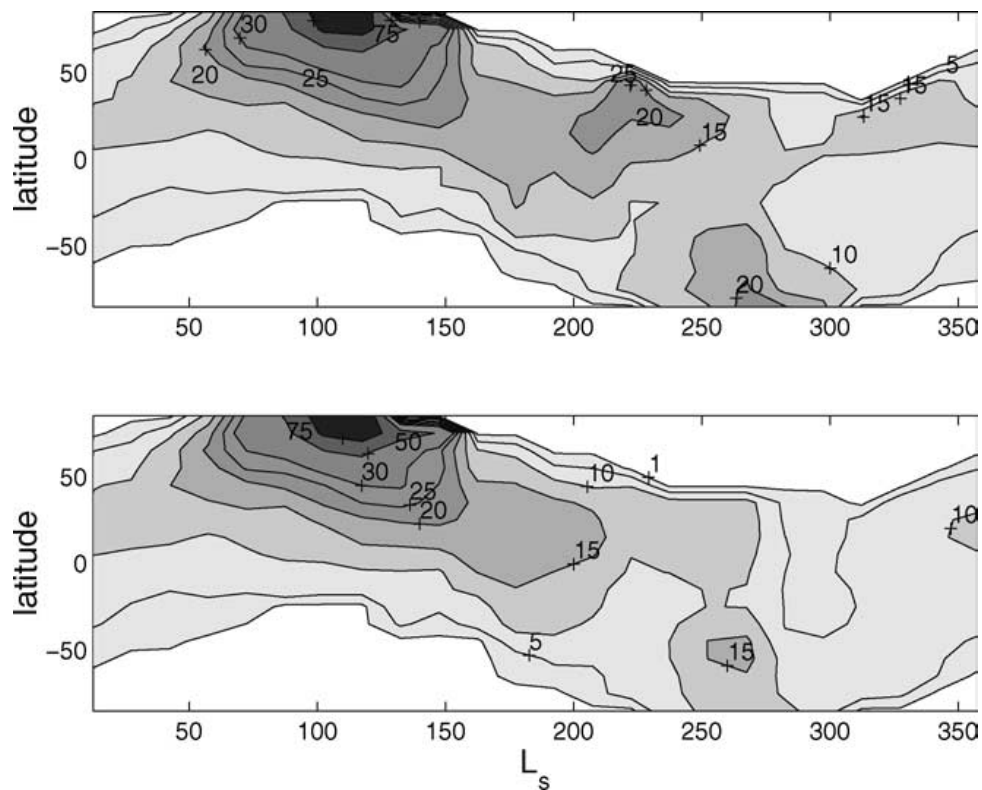


Figure 3.1: Top panel: Seasonal  $\text{H}_2\text{O}$  cycle with correction for aerosol influence as measured by MAWD. Bottom panel: original results without corrections. The correction for dust yields  $\text{H}_2\text{O}$  amounts that are by up to 100% larger. Taken from (Fedorova et al. 2004).

In parallel to the sounding from orbit the landers provided temperature measurements with a sensor in 1.6 m altitude. Ryan et al. (1982) deduced from *Viking 1* lander data a column density of  $\sim 20$  pr.  $\mu\text{m}$  during  $L_S=120-140^\circ$ ,  $2-3$  pr.  $\mu\text{m}$  during  $L_S=280-320^\circ$  and about 10 pr.  $\mu\text{m}$  in the rest of the year. However, these values require several assumptions and are thus prone to errors.

In the 1990's the role of water vapour in the environmental system of Mars was even better understood with new spacecraft observations. First the spatial imaging spectrometer ISM on *Phobos 2* detected an average column density of  $9\pm 3$  pr.  $\mu\text{m}$  in the south and  $12\pm 3$  pr.  $\mu\text{m}$  in the north by using the  $\text{H}_2\text{O}$  bands of  $1.9 \mu\text{m}$  and  $2.6 \mu\text{m}$  (Rosenqvist et al. 1992). Another instrument called Auguste had the advantage of measuring gas profiles in

the atmosphere with the means of solar occultation spectroscopy in the 1.9  $\mu\text{m}$  and 3.7  $\mu\text{m}$  bands. Therefore Krasnopol'skii et al. (1991) could provide an independent detection of 10 pr.  $\mu\text{m}$  of water with a mixing ratio of 150 ppm until an altitude of 12 km decreasing towards 3 ppm at 40 km. The solar longitude of the *Phobos 2* observations is around  $10^\circ$ . A reanalysis of both the ISM and the Auguste data provided additional proof for an exchange of water between surface regolith and the atmosphere on a hourly timescale. Hereby the water amount changes by a factor 3–4 from the morning to midday (Titov et al. 1995). Also a more detailed description of the vertical distribution was given by Rodin et al. (1997) with a mean column density of  $8.3_{-1.5}^{+2.5}$  pr.  $\mu\text{m}$  and a saturation into clouds at a level of 20–25 km.

In 1997 the camera of the *Pathfinder* lander ( $19.3^\circ\text{N}$ ,  $33.6^\circ\text{W}$ ) provided photometric data which could be used to investigate atmospheric water from the ground by imaging the sun. Yet this IMP data was taken at only one location in the Ares Vallis and had a limited temporal coverage due to the short duration of the mission. Measuring the radiance in five narrow filters around the 0.94  $\mu\text{m}$  absorption line under high-airmass conditions yielded the following results: a column density of  $6 \pm 4$  pr.  $\mu\text{m}$  at  $L_S = 150^\circ$  but, more important, a confinement of the vapour to the lower 1–3 km above the surface (Titov et al. 1999).

Between 1999 and August 2004 a new large dataset was recorded by the Thermal Emission Spectrometer (TES) onboard the *Mars Global Surveyor* spacecraft that covers more than two martian years and is today what the MAWD data were in the Viking era (Smith 2004). TES observed Mars at constantly 14:00 hours local time in the thermal infrared. Four rotational H<sub>2</sub>O bands between  $240\text{ cm}^{-1}$  and  $360\text{ cm}^{-1}$  were used for retrievals. The development of water in the atmosphere between the martian years MY 24 and MY 26 is shown in figure 3.2. The summer maximum in the polar region for the northern hemisphere reached about 75–100 pr.  $\mu\text{m}$  and the southern one about 35 pr.  $\mu\text{m}$ , each poleward of  $\sim 75^\circ$ . In autumn and winter of both hemispheres the lowest detected amounts of less than 5 pr.  $\mu\text{m}$  are occurring at middle and high latitudes, respectively. Due to the long operations of TES a comparison of different martian years was possible. So after the northern summer a movement of the water maximum towards southern latitudes was witnessed in both years. For MY 24 the location was as follows: at  $L_S = 115^\circ$  at  $80^\circ\text{N}$ , at  $L_S = 135^\circ$  at  $45^\circ\text{N}$ , at  $L_S = 150^\circ$  at  $30^\circ\text{N}$  and at  $L_S = 180^\circ$  at the equator (Smith 2002). During the southern summer there was also a second local maximum between  $0^\circ$  and  $30^\circ\text{N}$  visible but with a much smaller peak than the maximum at the south pole. The origin of this local increase in water vapour is most likely the Hadley cell transporting polar air northward (cf. chapter 2.4). Finally, around vernal equinox the global water abundance returned to a mean of 7–8 pr.  $\mu\text{m}$ .

Regarding the interannual variability of the water cycle there are moderate differences visible in the TES dataset, especially in the southern summer. In MY 24 its maximum of 35–40 pr.  $\mu\text{m}$  was not repeated in MY 25 which saw only 25 pr.  $\mu\text{m}$ . Also the secondary maximum in the northern equator region is much less pronounced. The simultaneous measurement of dust opacity also rules out problems in the retrieval caused by it. On the other hand, there was a global dust storm in 2001 (MY 25) which increased the albedo in southern areas that have usually a lower albedo and therefore changed the daytime surface temperature. This in turn might affect the water vapour amount.

A comparison of the first part of the dataset with the MAWD results was given by Smith (2002) and showed a general agreement but a systematically higher offset of  $\sim 20\%$

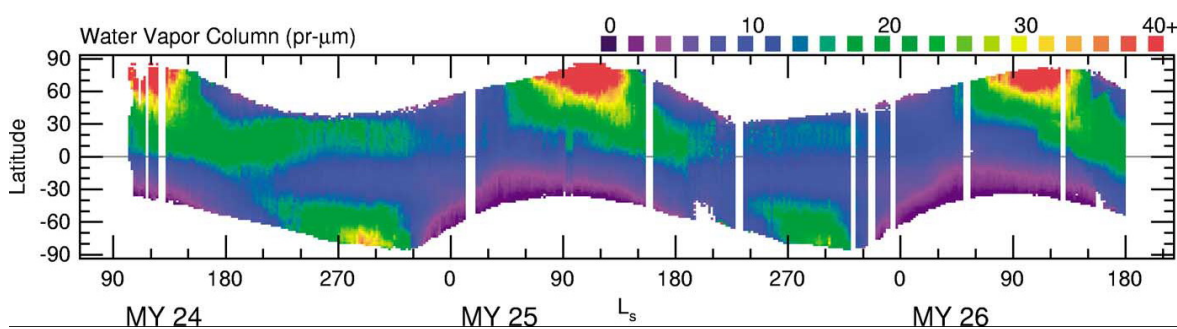


Figure 3.2: *MGS/TES* results: The zonal mean water vapour as a function of season covering two martian years shows a repeatable pattern in the water cycle but also differences, in particular between  $L_S=270^\circ$  and  $L_S=300^\circ$ . Adopted from Smith (2004).

of TES compared to MAWD. The strong difference in the southern summer maximum which was not very distinctive in the original MAWD results was already explained above (Fedorova et al. 2004). Moreover, the secondary maximum during southern summer as seen by TES seemed not to exist in the MAWD data unless the correction for dust was applied. At this point it needs to be stated that after a reanalysis with only the two strongest bands at  $250$  and  $280\text{ cm}^{-1}$  M. Smith now corrected the TES results to about 70% of their originally published values (private communication, Smith 2006), which brings them in better agreement with other measurements. Due to its coverage of water vapour, water ice and dust the TES database is at the moment still the prime reference for comparisons.

Since TES stopped working on August 31<sup>st</sup>, 2004 orbital observations are currently taken over by the European *Mars Express* orbiter with its three spectrometers OMEGA, SPICAM and PFS (cf. chapter 4.1). Their simultaneous observations will be explicitly compared among each other and with the results of this work in chapter 6.6.

### 3.1.2 Observations from Earth

In parallel to spacecraft observations valuable contributions to the questions about  $\text{H}_2\text{O}$  were given by measurements from the vantage point of Earth which are naturally restricted in spatial resolution and in seasonal coverage by sighting opportunities. Groundbased and Earth-orbiting instruments are utilizing absorption bands in infrared, sub-mm, millimeter and microwave bands.

Since the first spectroscopic observations from ground the Doppler shift is utilized for the near-IR band around  $8200\text{ \AA}$ . In this method the martian water absorption line is Doppler-shifted with respect to the terrestrial line and resolvable in case the terrestrial line is not saturated. Over the decades different values of column density and the discovery of seasonal and spatial variations were reported. After the 1969 opposition Barker et al. (1970) reported quite large amounts of 45 to 50  $\text{pr.}\mu\text{m}$  during late southern summer ( $L_S=320\text{--}340^\circ$ ) which seemed to contradict the so far consistent results of 10 to 20  $\text{pr.}\mu\text{m}$ . For example Schorn et al. (1967) found 15  $\text{pr.}\mu\text{m}$  for the northern hemisphere at  $L_S=47\text{--}61^\circ$  and  $\sim 10\text{ pr.}\mu\text{m}$  for the southern hemisphere during  $L_S=110\text{--}122^\circ$ . Later on, larger datasets in the 1970's by Barker (1976) confirmed the average amount of around

15 pr.  $\mu\text{m}$  during solstices and showed the presence of a diurnal and seasonal cycle with latitudinal differences. The maximum H<sub>2</sub>O content in the summers of both hemispheres was reported to be about 40 pr.  $\mu\text{m}$ . Jakosky and Barker (1984) presented disk-integrated measurements taken between 1975 and 1983, thus allowing comparisons with the *Viking* results. Apart from the much higher 17–27 pr.  $\mu\text{m}$  between  $L_S=195^\circ$  and  $245^\circ$  before the *Viking* arrival the retrieved amounts are only slightly larger than the originally published ones of MAWD. Compared with earlier data there appears to be mainly an interannual variation. With improving techniques the behaviour of atmospheric water was monitored at further oppositions in the 1980's and 1990's with the same method. Rizk et al. (1991) observed Mars four times during southern spring and summer. For  $L_S=208^\circ$  and  $L_S=360^\circ$  there is a very good agreement with the MAWD results over all latitudes: a very low column density for high southern latitudes, a maximum of  $\sim 15$  pr.  $\mu\text{m}$  for  $20^\circ\text{S}$  to the equator, decreasing to  $\sim 6$  pr.  $\mu\text{m}$  at  $40^\circ\text{N}$ . A difference of a factor of two appears during mid southern summer, though. At  $L_S=320^\circ$  there is a maximum of 14–20 pr.  $\mu\text{m}$  southward of  $40^\circ\text{S}$  while at  $L_S=340^\circ$  the development is 10 pr.  $\mu\text{m}$  between  $60^\circ\text{S}$  and  $40^\circ\text{S}$ , rising to only 16 pr.  $\mu\text{m}$  at  $\pm 10^\circ$  latitudes. Please note that for these last measurements there was a local dust storm reported that seems to be responsible for the 25–35% lower amounts.

A large dataset by Sprague et al. (1996) allowed a comparison of two martian years during northern summer but showed slight disagreements with earlier measurements and a variation of up to a factor of 3 between the two years. Although the general shape of the seasonal cycle was repeated quite well there were for example only 36.4 pr.  $\mu\text{m}$  at  $71.2^\circ\text{N}$  during  $L_S=100^\circ$ . Around the opposition of 1997 both for  $L_S=18.0\text{--}78.4^\circ$  and  $L_S=113.7\text{--}146.4^\circ$  the water was latitudinally and longitudinally distributed in an inhomogeneous way but generally consistent with the known seasonal behaviour. The maximum detected amounts were 40–45 pr.  $\mu\text{m}$  at latitudes between about  $60\text{--}80^\circ\text{N}$  both before ( $L_S=78.4^\circ$ ) and after ( $L_S=113.7^\circ$ ) summer solstice (Sprague et al. 2003). At the same time of TES operations in MY 24 Sprague et al. (2001) found 43–76 pr.  $\mu\text{m}$  at  $75^\circ\text{N}$  during  $L_S=105\text{--}115^\circ$  and 9–17 pr.  $\mu\text{m}$  at  $80^\circ\text{N}$  around  $L_S=150\text{--}160^\circ$ . Recently Sprague et al. (2006) reported also previously unpublished results from the years 1998–1999. There the seasonal coverage of MY 24 is extended and stretches now from  $L_S=34^\circ$  to  $L_S=249^\circ$ . The retrieved column densities vary generally between  $\sim 3$  pr.  $\mu\text{m}$  and almost 25 pr.  $\mu\text{m}$  for the times outside the northern summer. These values are consistently lower than the TES results between the equator and  $70^\circ\text{N}$ . The error is expected to be 20% for airmasses 3–6. Additionally, three more points of interest are noted in this publication: a diurnal trend is sometimes completely absent, sometimes present (then the noon values are 20–50% higher); a southern summer column density of 38 pr.  $\mu\text{m}$  at  $L_S=285\text{--}305^\circ$ ; an intercomparison of results for different martian years shows MY 24 to be wetter than MY 22 and 23.

Another facility on the ground suitable to detect martian water vapour is the NASA *IRTF* telescope. In 1997 (solar longitude  $67^\circ$ ) using the HDO absorption lines at  $3.67\ \mu\text{m}$  a column density of  $\sim 3$  pr.  $\mu\text{m}$  for southern latitudes rising to  $\sim 24$  pr.  $\mu\text{m}$  at  $70^\circ\text{N}$  was reported (Novak et al. 2002). Observations in 2003 of HDO/H<sub>2</sub>O absorption lines near  $1240\ \text{cm}^{-1}$  with higher spectral resolution by Encrenaz et al. (2005a) give a column density of  $17\pm 9$  pr.  $\mu\text{m}$  and a saturation at 30 km altitude at  $L_S=206^\circ$ . A preliminary result for data taken in 2005 suggests a 30–50% lower amount than two years before Encrenaz et al. (2006). Yet the martian season is also different with  $L_S=332^\circ$ .

Data of *ISO* from 1997 analysed in the spectral ranges of 5.6–8  $\mu\text{m}$  and 39–41  $\mu\text{m}$  describes water with  $12 \pm 3.5$  pr.  $\mu\text{m}$  and a condensation level of  $13 \pm 2$  km for the season around  $L_S = 160^\circ$  (Burgdorf et al. 2000). Similar results from the same dataset were independently reported by Lellouch et al. (2000), namely a column density of 15 pr.  $\mu\text{m}$  and a saturation at approximately 10 km.

In addition, observations can be done in the submillimeter range, but for this purpose space observatories are necessary. The team of the *SWAS* satellite analysing the rotational transitions around 554 GHz found a water amount of  $8_{-3}^{+12}$  pr.  $\mu\text{m}$ , averaged over the disk at  $128^\circ$  solar longitude, and a saturation level at 10 km (Gurwell et al. 2000). In 2001 *SWAS* was again turned towards Mars between  $L_S = 166^\circ$  and  $L_S = 233^\circ$ . During this time the water held by the atmosphere was around  $12 \pm 6$  pr.  $\mu\text{m}$  while the saturation altitude was rising from about 25 km to 70 km due to the atmospheric warming caused by the global dust storm of 2001 (Gurwell et al. 2005). Then in 2003 using the 557 GHz line the *ODIN* satellite measured  $13 \pm 3$  pr.  $\mu\text{m}$  at  $L_S = 204^\circ$  and  $10 \pm 2$  pr.  $\mu\text{m}$  at  $L_S = 293^\circ$ . Both detections included a high saturation level at 22 km (Biver et al. 2005). These sub-mm results are generally consistent with other values but are very sensitive to the precise vertical structure of the temperature.

The millimeter part of the spectrum was chosen by Encrenaz et al. (1995) for the search for atmospheric water. With the *IRAM* 30m antenna a tentative detection of the 183 GHz line has yielded an upper limit of only  $3 \pm 2$  pr.  $\mu\text{m}$  (without saturation) at  $L_S = 4^\circ$ . Five weeks before those observations Clancy et al. (1992) used the *Very Large Array* to analyse the 22 GHz emission line coming from Mars' limb. The observations around  $L_S = 345^\circ$  determined a low amount of only  $4.5 \pm 1$  pr.  $\mu\text{m}$  around the equator and  $2.9 \pm 0.7$  pr.  $\mu\text{m}$  at mid-latitudes. Here an possible saturation level must be higher than 45 km. This result is in good agreement with the millimeter observations but both are lower than expected.

As a conclusion, the essence of all these available datasets has led to the understanding of a complex water cycle on Mars. Now the following chapter describes the seasonal evolution of the atmospheric water like it is understood at the moment.

## 3.2 The seasonal cycle of atmospheric water

Despite existing discrepancies there is a general consensus about the behaviour of water vapour in the course of a martian year. The driving mechanisms to support this cycle are the deposition and sublimation on the polar caps, exchange with potential ground ice close to the surface and adsorption/desorption with the soil, combined with the global transport through atmospheric circulation (Jakosky and Haberle 1992). These processes will now be described in greater detail.

This annual cycle can be shortly described by a global average column density varying seasonally from 14 to 35 pr.  $\mu\text{m}$  (Smith 2002) and a local increase at the poles by a factor of 5 during the northern summer while during the southern summer lower abundances are detected. Those are also variable from year to year due to changing dust conditions. In detail, during the season from  $L_S = 0-40^\circ$  the global average water in the atmosphere is generally around 10–15 pr.  $\mu\text{m}$  (with disagreements of up to a factor of 3 between different reports). Then for  $L_S = 40-90^\circ$  there is a fast rise of this amount northward of  $30^\circ\text{N}$  towards

the annual maximum, driven by the beginning sublimation of the north pole cap and the release of water from the regolith. Until  $L_S=130^\circ$  the polar maximum of 75–100 pr.  $\mu\text{m}$  dominates the northern atmosphere. At the same time the  $\text{H}_2\text{O}$  content around the equator and south of it remains at very low levels. Furthermore, there is no secondary maximum detectable like in the summer of the south. Backed by images of water ice clouds and measured temperature profiles the reason for this is the presence of a saturation layer at very low altitudes down to 10 km. Since this cloudy season concurs approximately with Mars' furthest position from the sun the region northward of the equator is often called aphelion cloud belt. Physically the colder air during aphelion brings the point of condensation closer to the surface and the upwelling air of the Hadley circulation carries water vapour in large quantities. Because the gaseous water forms ice particles it is prevented from rising higher and being transported to the south and hence locked in the northern polar region. This was pointed out the first time by Clancy et al. (1996) and explains – apart from the elevation dichotomy – the large amplitude difference of the summer  $\text{H}_2\text{O}$  maxima of both hemispheres.

In general the mentioned ice clouds are certainly an important component of the martian water cycle since they are able to transport water via the global atmospheric dynamics over large distances (Montmessin et al. 2004). In observations they are visible in images both from orbiters (Hale et al. 2005) and landers and are also mapped as absorptions bands of  $\text{H}_2\text{O}$  ice aerosols (near 2  $\mu\text{m}$  and 3  $\mu\text{m}$ ) by spectrometers like TES (Smith 2004).

Now with the end of summer in the north the water disappears quickly from the air and the column density returns to low values in the areas northward of  $60^\circ\text{N}$  by  $L_S=135^\circ$ . During the same time a spike of 15–20 pr.  $\mu\text{m}$  moves towards the equator and reaches it around  $L_S=170^\circ$ . This peak then seems to split up around  $L_S=200^\circ$ . The northern branch is decreasing in amplitude but present at  $0\text{--}30^\circ\text{N}$  until the start of a new year. For the second branch it has been argued that it resembles a net transport of water vapour into the southern hemisphere (Read and Lewis 2004) because it looks like the continuing spike coming from the northern hemisphere. On the one hand, calculations have shown that the atmospheric circulation is not capable to support this theory and a release from the soil is a more reasonable explanation (Jakosky and Haberle 1992). On the other hand, a look at hemispherically averaged trends supports the north to south transport across the equator during  $L_S=150\text{--}230^\circ$  (Smith 2002). In parallel to this process it is visible that after the autumnal equinox the water content of the southern hemisphere rises slowly, reaching a maximum between solar longitudes  $260^\circ$  and  $320^\circ$  southward of  $60^\circ\text{S}$ . This peak can have quite different values from year to year as the observations show that are summarized in the following. Still Barker et al. (1970)'s detection of 45–50 pr.  $\mu\text{m}$  for  $L_S=320\text{--}340^\circ$  seems to be the highest until today; *Mariner 9* and *Mars 3* were taking data around southern mid-summer with a giant dust storm and found 10–20 pr.  $\mu\text{m}$ ; Barker (1976) estimated a maximum of  $\sim 40$  pr.  $\mu\text{m}$ ; the dust-corrected MAWD results give 20 pr.  $\mu\text{m}$  and more for high southern latitudes between  $L_S=260^\circ$  and  $290^\circ$ ; Jakosky and Barker (1984) reported disk-integrated amounts of 10–15 pr.  $\mu\text{m}$  during  $L_S=275\text{--}285^\circ$ ; Rizk et al. (1991) detected 14–20 pr.  $\mu\text{m}$  at  $L_S=320^\circ$  with an assumed underestimation of 25–35% due to a local dust storm; TES (corrected) found 18–28 pr.  $\mu\text{m}$  at  $L_S=297^\circ$  and 10–15 pr.  $\mu\text{m}$  at  $L_S=318^\circ$  in MY 24; in MY 25 the maximum amount was by about 3 pr.  $\mu\text{m}$  lower; *ODIN* detected  $10\pm 2$  pr.  $\mu\text{m}$  at  $L_S=293^\circ$  but at only  $24^\circ\text{S}$  latitude. For MY 27 *MEX/SPICAM* reported 13–16 pr.  $\mu\text{m}$  during  $L_S=270\text{--}310^\circ$  with peaks at  $70\text{--}80^\circ\text{S}$  (Fedorova et al. 2006).

The most likely explanation for the differences in the results are – apart from actual measurement uncertainties or errors – either naturally occurring variations or the influence of dust on the measurements. This can either be by masking the true amount, e.g. for near infrared observations, or by physical processes influencing the atmosphere, described further below. Hence differences with older datasets might be explained with the use of advanced analysis tools and more elaborate models. For example, after the reanalysis of *Mariner 9* data a diurnal cycle was also found there (Ignatiev et al. 2002) or the MAWD data could be corrected for dust influence which provided a better agreement with TES results (Fedorova et al. 2004).

Again regarding the water cycle, there is a clearly visible secondary maximum in the southern summer, located between 0–30°N which was mentioned above. The explanation for it is the cross-equatorial Hadley cell transporting the H<sub>2</sub>O gas from the south polar region into the northern hemisphere. In conclusion, the mechanisms of the southern summer are not well understood. Especially the confirmation of a net water transport and the interaction of the dust, the CO<sub>2</sub>– and H<sub>2</sub>O-cycle require further research.

After L<sub>S</sub>=320° the water dynamics reaches its quiet state rather quickly with a mean content of ~10 pr. μm. At the same time when the south pole maximum decreases also the secondary maximum starts to vanish. By the end of the year the atmosphere contains more or less homogeneously the same low amount of water until the circle closes with the beginning of a new martian year.

As for the interaction of the water cycle with the dust– and CO<sub>2</sub>–cycles there are several connections of importance. One point is that increased dust opacity raises the air temperature and thus its capability to hold water vapour. On the other hand, dust serves as a condensation nucleus and can in turn be removed from the atmosphere because the water condenses on it and the conglomerate sinks to the ground. Via this mechanism also the water itself is brought from higher altitudes back towards the surface. The impact of dust storms on the water cycle is as well supported by theoretical models requiring an adsorbing regolith (Böttger et al. 2004) whose properties will be described in section 3.3. Concerning CO<sub>2</sub> and H<sub>2</sub>O, in particular at the south pole there is a mixture of both compounds in the perennial and seasonal ice. This was recently confirmed by *Mars Express* with OMEGA (Bibring et al. 2004) and PFS (Hansen et al. 2005) but with disagreeing mixing ratios. Both gases certainly influence each other as the CO<sub>2</sub> ice at about 150 K acts as a cold trap for the water vapour, and water is released in turn when the carbon dioxide is sublimed. Finally, the meridional winds caused by the physical phase change of the carbon dioxide also affect the process of dust and water transportation in the polar zones.

### 3.3 Surface–atmosphere interaction

Not only the characteristics of the seasonal H<sub>2</sub>O behaviour hint to an interplay of water vapour with regolith but there are also independent measurements of hydrogen in the uppermost soil – let alone the presence of surface frost like at the *Viking 1* landing site. The neutron spectrometers onboard the *Mars Odyssey* spacecraft detected high mass-fractions of 20–100% of hydrogen in the upper layers of martian regolith poleward of ±50° latitude and still up to 10% in the regions of ±45° around the equator (Feldman

et al. 2004). Assuming this hydrogen belongs to water molecules Mitrofanov et al. (2004) showed that the subsurface in the subpolar areas can consist of up to 50% by weight of water. For mid- and low latitudes Möhlmann (2004) argues that adsorption is the only process that can keep water in the soil as sublimation would remove H<sub>2</sub>O with a factor of  $\sim 10^5$  more effectively. The reason for this is that the bonding of water molecules due to Van-der-Waals forces with an enthalpy of  $\Delta H_{ad} = \sim 70$  kJ/mol is always higher than the sublimation enthalpy of ice ( $\Delta H_S = 51$  kJ/mol). The gas release rate  $Z$  for sublimation is given by the Hertz-Knudsen formula:

$$Z = 3.47 \cdot 10^{12} \cdot \frac{\exp\left(\frac{-\Delta H_S}{k_B T}\right)}{\sqrt{2\pi m_w k T}} \quad [\text{molecule m}^{-2}\text{s}^{-1}]$$

Here  $\Delta H_S$  is given in 0.529 eV per molecule,  $m_w$  [kg] is the molecular mass,  $T$  [K] the temperature and  $k_B$  the Boltzmann constant. In addition, the bonding strength in minerals increases for lower water content of the regolith and therefore generally about two monolayers of adsorbed water cover the regolith pores. However, the exact amount of adsorbed water depends on the specific properties of the minerals which are not well known.

Recently though, hydrated minerals (phyllosilicates and sulfates) were detected on Mars, both from orbit (Bibring et al. 2005) and from ground (Squyres et al. 2004). Consequently it was easier to focus on specific minerals for the investigation of their properties. Jänchen et al. (2006) analysed the sorption<sup>3</sup> capacities of porous zeolites, clay minerals, magnesium-sulfates and gypsum under martian conditions. The outcome was that for a H<sub>2</sub>O partial pressure of 0.001 mbar in a temperature range from 193 to 333 K the minerals stay hydrated and can keep water with 2.5 to 25 percent of mass. The difference to earlier investigations on basalts (Zent and Quinn 1995) and montmorillonites (Zent et al. 2001), yielding a capacity which is by an order of magnitude smaller than measurements on Mars, is therefore most likely explained with the use of inadequate minerals for the experiments.

Now how deep is the regolith layer that is involved in the atmospheric interaction? The temperature of the atmosphere above the ground affects the subsurface temperature until a certain penetration depth which is given by three thermal skin depths  $D_{th}$  according to Möhlmann (2004) where:

$$D_{th} = \sqrt{\frac{\lambda P}{\rho_s c}} = \frac{I \sqrt{P}}{\rho_s c} \quad (3.1)$$

with  $P$  the period of planetary rotation,  $\lambda$  the heat conductivity of the soil,  $\rho_s$  its mass density,  $c$  the heat capacity and  $I = \sqrt{\lambda \rho_s c}$  the thermal inertia, given in  $[\text{J m}^{-2} \text{K}^{-1} \text{s}^{-1/2}]$ . Typical values for skin depths are one to several centimeters. Measurements of thermal inertia on Mars are typically in the range of 24–800  $\text{J m}^{-2} \text{K}^{-1} \text{s}^{-1/2}$  (Putzig et al. 2005) and values of  $\rho_s = 1500 \text{ kg m}^{-3}$  and  $c = 837 \text{ J kg}^{-1} \text{K}^{-1}$  for basalts can be assumed (Möhlmann 2004). Since the amplitudes of seasonal temperature variations are much larger and longer lasting than the diurnal ones the seasonal penetration depths are 25 times larger and can go down from a few tens of centimeters to more than a meter until an assumed stable ice layer is reached.

<sup>3</sup>Sorption means binding of water by physical adsorption or chemisorption by chemical bonds.

To describe the dynamics of water exchange with regolith one needs an empirical model describing the adsorption and desorption back into the atmosphere using the diffusion equation. Physically the amount of gas, that is adsorbed as a function of the pressure, can be described by so-called isotherms. In general the amount of adsorbed gas increases with decreasing temperature. Yet there are five different types of isotherms according to the characteristics of the involved reaction partners causing for example monolayer or multilayer adsorption or condensation in micropores (Vold and Vold 1983). Alternatively an empirically found isotherm to describe the amount of adsorption  $\alpha$  is used by Böttger et al. (2005):

$$\alpha = \rho_S \cdot \frac{\beta \cdot p_w^{0.51}}{e^{\delta/T}} = F \cdot n^{0.51} \text{ [kg m}^{-3}\text{]} \quad \text{with} \quad F = \rho_S \cdot \frac{\beta}{e^{\delta/T}} \left( \frac{kT}{m_w} \right)^{0.51}$$

Here  $\rho_S$  is the density of the regolith,  $\beta = 2.043 \cdot 10^{-8} \text{ Pa}^{-1}$ ,  $\delta = -2679.8 \text{ K}$ ,  $p_w$  the  $\text{H}_2\text{O}$  partial pressure and  $T$  the ground temperature. Starting from this equation and under the assumption of no ground ice the mass density of diffused water vapour  $n_t$  in the regolith for any timestep  $t$  can be calculated as follows:

$$n_t = \frac{\sigma_t^2}{F_t^2} \cdot \left( 1 - \frac{2\sigma_t \epsilon}{F_t^2} \right)$$

where  $\sigma_t$  is the total amount of water in the regolith (only diffused and adsorbed) and  $\epsilon$  the porosity of the soil material.

Regarding the transportation of vapour in the ground and the exchange with the atmosphere the dominating process is diffusion which is described by  $\Phi = D \cdot \frac{\partial n}{\partial z}$  with  $\Phi$  the  $\text{H}_2\text{O}$  flux and  $D$  the diffusion coefficient. With the relation  $\epsilon \cdot \frac{\partial n}{\partial t} = \frac{\partial \Phi}{\partial z}$  the result is the diffusion equation:

$$\frac{\partial n}{\partial t} = \frac{D}{\epsilon} \cdot \frac{\partial^2 n}{\partial z^2} \quad (3.2)$$

The porosity and the diffusion coefficient are of course the great unknowns. Especially the latter depends on the size of the pores in the material and its relation to the mean free path of the molecules. If the pores are larger than the free mean path then molecular collision will dominate causing a high and constant diffusion coefficient. If the pores are smaller the molecules will predominantly collide with the pore "walls" yielding a quickly declining coefficient (Böttger et al. 2005).

### 3.4 The diurnal cycle and an alternate theory

The ability of the surface to store and buffer atmospheric water results in a diurnal variation of the  $\text{H}_2\text{O}$  mixing ratio. Due to changing temperatures in the course of a sol – which is of course modulated by seasonal temperature changes – water is released or adsorbed by the regolith until a certain depth described by equation 3.1.

The resulting diurnal cycle has been measured the first time by MAWD and was most prominent in the Tharsis and Lunae Planum areas (Jakosky et al. 1988). Later also ISM onboard *Phobos 2* found an increase of a factor of 2–3 between morning and noon near the Tharsis volcano Pavonis Mons (Titov 2002). Ground-based observations by Hunten

et al. (2000) confirmed these strong variations during the day and Sprague et al. (2003) found a factor of 2–3, too. A recent reanalysis of *Mariner 9* data yielded as well a 2- to 3-fold increase in atmospheric water in correlation with the surface temperature rise from morning to noon (Formisano et al. 2001, Ignatiev et al. 2002). Comparing the available data leads to the conclusion that up to 10 pr.  $\mu\text{m}$  of  $\text{H}_2\text{O}$  can be stored and released during a diurnal cycle. This theory is backed by the observation that the variability is symmetric to midday when the ground temperature is the highest (Titov 2002).

Despite the reasonable explanation for the above described phenomena there exists also a competing theory. Jakosky et al. (2005) proposed transient ground ice in the upper meter of the surface between  $\pm 60^\circ$  latitude. The origin of this ice would lie in a recent climate change that saw much higher amounts of atmospheric water in an earlier period which allowed the build-up of subsurface ice. While today the ice is stable poleward of  $\pm 60^\circ$  latitude the equatorial ice is in an unstable state and slowly diffusing back into the atmosphere with a rate determined by the diffusion equation 3.2. This would explain the longitudinally inhomogeneous distribution of gaseous  $\text{H}_2\text{O}$  with two maxima and minima and its poor correlation with surface hydrogen and other surface characteristics, such as topography, composition, albedo or thermal inertia. This theory was recently backed up by Forget et al. (2006a) whose martian climate model predicts ice accumulation on the western slopes of the Tharsis volcanoes and also an area east of the Hellas basin for a rotational axis tilt of  $45^\circ$ . In these areas there is evidence for glacial features from orbital imaging that are only a few million years old. A recent run of the climate model with high atmospheric dust content additionally yields a weak but persistent accumulation of ice in the Arabia Terra region (private communication, Forget 2006).



## 4 The PFS experiment on *Mars Express*

### 4.1 The *Mars Express* mission

After the loss of the Russian *Mars 96* spacecraft in November 1996 which had four European experiments onboard the European Space Agency quickly decided to fly its own mission to Mars. Within only four years ESA readied its first probe to another planet for the launch date on June 2<sup>nd</sup>, 2003. When launching with a Sojus-Fregat rocket from the Bajkonur Cosmodrome in Kasachstan the *Mars Express (MEX)* spacecraft had a wet mass of 1223 kg, including the ill-fated *Beagle 2* lander and seven experiments. Two solar panels produce approximately 460 W power at Mars<sup>1</sup> although 410 W are required for observation and 500 W for data transfer. To mediate this problem there are some orbits used only for communication which is established via a S-band (2.2 GHz) antenna for uplink and telemetry downlink and a X-band (8.4 GHz) antenna for transmission of data with a maximum rate of 230 KBit per second. The seven instruments of *MEX* are built for surface studies (High Resolution Stereo Camera HRSC, visible and infrared mineralogical mapping spectrometer OMEGA, subsurface sounding radar altimeter MARSIS) and atmospheric investigations (Planetary Fourier Spectrometer PFS, ultraviolet and infrared atmospheric spectrometer SPICAM, energetic neutral atoms analyser ASPERA-3, Mars Radio Science experiment MaRS). These experiments are – apart from the radar antennas – all located on one nadir-looking side of the 1.5×1.8×1.4 m spacecraft bus. One of the main goals to be investigated by the instruments is the history of water, its distribution and behaviour, and this not only in the entire atmosphere but also in the surface materials and subsurface.

Since the orbit insertion on December 25<sup>th</sup>, 2003 ( $L_S=322^\circ$ ) and the subsequent adjustment into the final mapping orbit in January 2004 the first few hundred revolutions were kept with an inclination of  $86.35^\circ$  and a 7.6 h revolution time. After a change in orbit 405, to reduce the eclipse time of the spacecraft, *MEX* has now a 6.7 h orbital period with an apocenter at 10 107 km and a pericenter at 298 km altitude. Only during one hour around pericenter pass the instruments observe the planet while the rest of the orbit is used for communications. However, due to the restrictions of power and downlink telemetry all the instruments cannot operate at the same time. In the course of the mission the pericenter was moving due to orbit precession from near the equator after orbit insertion towards the south pole in July 2004 (orbit 523 at  $L_S=48.8^\circ$ ) and afterwards towards the north pole which was reached in March 2005 (orbit 1536 at  $L_S=183.4^\circ$ ). This pericenter precession

---

<sup>1</sup>Due to a wiring problem *MEX* can only produce 70% of its originally planned power output.

persists of course for the rest of the spacecraft lifetime. Therefore the seasonal coverage is optimized and several local times are covered (from 7 AM to 5 PM). On the other hand the spatial resolution at a given surface point then depends on the season and both seasonal and diurnal variations need to be disentangled.

Two other spectrometers onboard *MEX*, OMEGA and SPICAM, have the ability to sound the atmosphere for water vapour, too. Hence their instrumental properties are interesting in comparison with PFS. OMEGA's spectral resolution is only about  $21\text{ cm}^{-1}$  in the  $2.6\text{ }\mu\text{m}$  water band while its spatial resolution can be up to 300 m in the pericenter. In contrast to the other spectrometers SPICAM exploits the  $1.38\text{ }\mu\text{m}$  band for water studies with a spectral resolution of  $3.5\text{ cm}^{-1}$ .

## 4.2 The Planetary Fourier Spectrometer

One of the three spectrometers on *MEX*, specifically designed for atmospheric sounding, was also inherited from *Mars 96*: the Planetary Fourier Spectrometer (PFS). An in-depth description of this 30.9 kg instrument and its capabilities is given by Formisano et al. (2004) and Formisano et al. (2005). The features that are important for this work are described in the following. PFS is a double pendulum Fourier spectrometer that detects infrared radiation in two channels. The longwavelength channel LW covers the thermal radiation of Mars between 5 and  $40\text{ }\mu\text{m}$  ( $250\text{--}2000\text{ cm}^{-1}$ ) and the shortwavelength channel SW is sensitive to reflected sunlight in the range of  $1.2\text{--}5.8\text{ }\mu\text{m}$  ( $1700\text{--}8200\text{ cm}^{-1}$ ). The simultaneous recording of both spectra is achieved by splitting the incoming light with a dichroic mirror and feeding the beams into two interferometers working in parallel. Similar to the principle of a Michelson interferometer the interferograms are created by two rotating corner cube mirrors in each apparatus as shown in figure 4.1. The mirrors are jointly driven by a single motor which gets feedback for its rotation speed from two laser beams which run in parallel to the incoming IR rays. In addition, the responsible laser diodes provide the trigger for the data acquisition of the A/D converter of the detector. This happens for the SW at every zeropoint crossing of the laser interferogram and for the LW at every fourth zeropoint crossing. The SW detector is a PbSe photoconductor device operating at about 212 K. In Mars orbit the acquisition of an individual interferogram has a duration of 4 seconds and is performed every 8.5 seconds.

The operations during the science phase of each revolution around Mars generally start and end with taking – in most cases – 31 calibration measurements. For this purpose a scanning mechanism in front of the optical system is pointed first towards deep space, then towards an internal black-body and finally an internal calibration lamp. Near the pericenter pass the pointing is towards the planet and spectra of Mars are recorded, in general between 200 and 300 depending on operational and orbital constraints. Because PFS/LW has a field of view of  $2.8^\circ$  this results in a nadir LW footprint of about 15–150 km, depending on the spacecraft flight altitude which is generally  $\sim 300\text{ km}$  up to several hundreds of kilometers. For PFS/SW the values are a  $1.6^\circ$  field of view and a footprint of 8–80 km on the surface.

The spectra are obtained after a Fast Fourier Transformation (FFT) of the double-sided interferograms. Those have the advantage of insensitivity to the location of the optical zeropoint and therefore to phase errors. PFS has 15 data transmission modes,

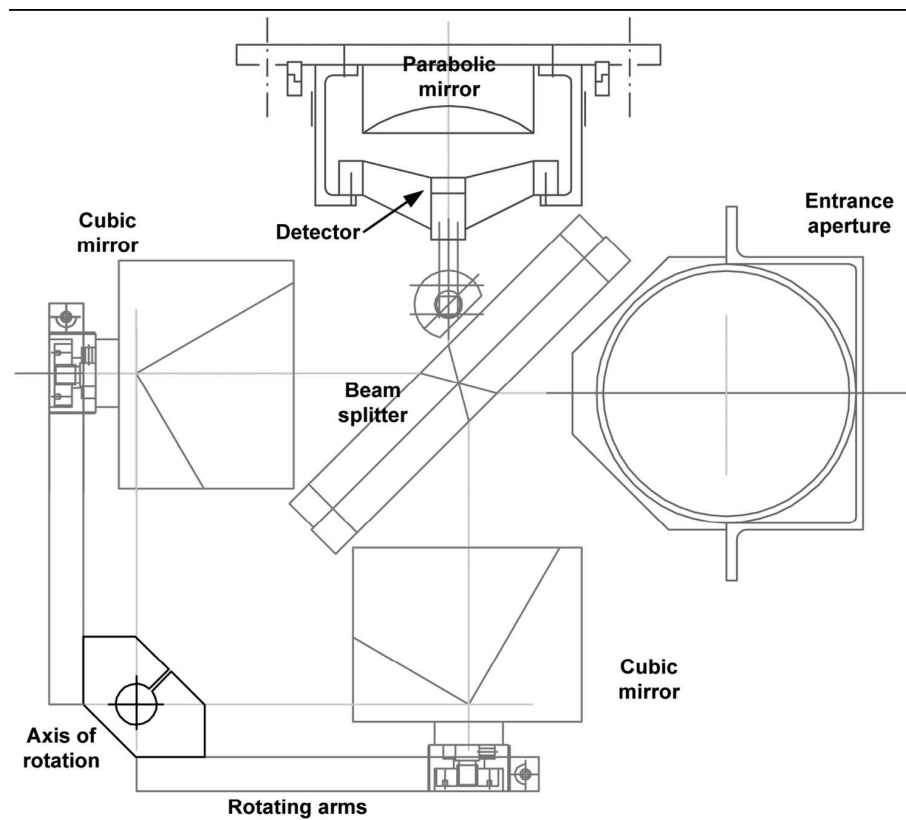


Figure 4.1: The optical system of one PFS interferometer which is schematically identical for each of them. The previously split beam is brought to interference by two rotating mirrors and recorded by the detector. Taken from Comolli and Saggin (2005).

including an autotest, and if required the FFT can be performed onboard. The most used modes are full LW and SW interferograms, one-sided LW and SW interferograms and half resolution LW and SW interferograms. An example of an average LW spectrum is presented in figure 4.2 and of a typical SW spectrum in figure 4.3. Both are the average of observation numbers 1 to 218 of orbit 1023. Relevant water vapour bands lying in these spectral ranges are described in appendix A.2.

Last but not least, the spectral response function of the instrument has a full width at half maximum (FWHM) of  $1.38 \text{ cm}^{-1}$  in the unapodized version with a spectral sampling step of  $1.02 \text{ cm}^{-1}$ . With Hamming apodization, explained in appendix A.5, it has a lower FWHM of  $2.04 \text{ cm}^{-1}$ . Apodized spectra were used for this work because of their noise reduction advantage and decrease of the overshooting effect. That asymmetric feature of a deeper lobe in the red wing than in the blue one is typical for the PFS instrumental transfer function<sup>2</sup> and can be seen in figure 4.4.

<sup>2</sup>An ideal Fourier spectrometer function follows a *sinc*-function.

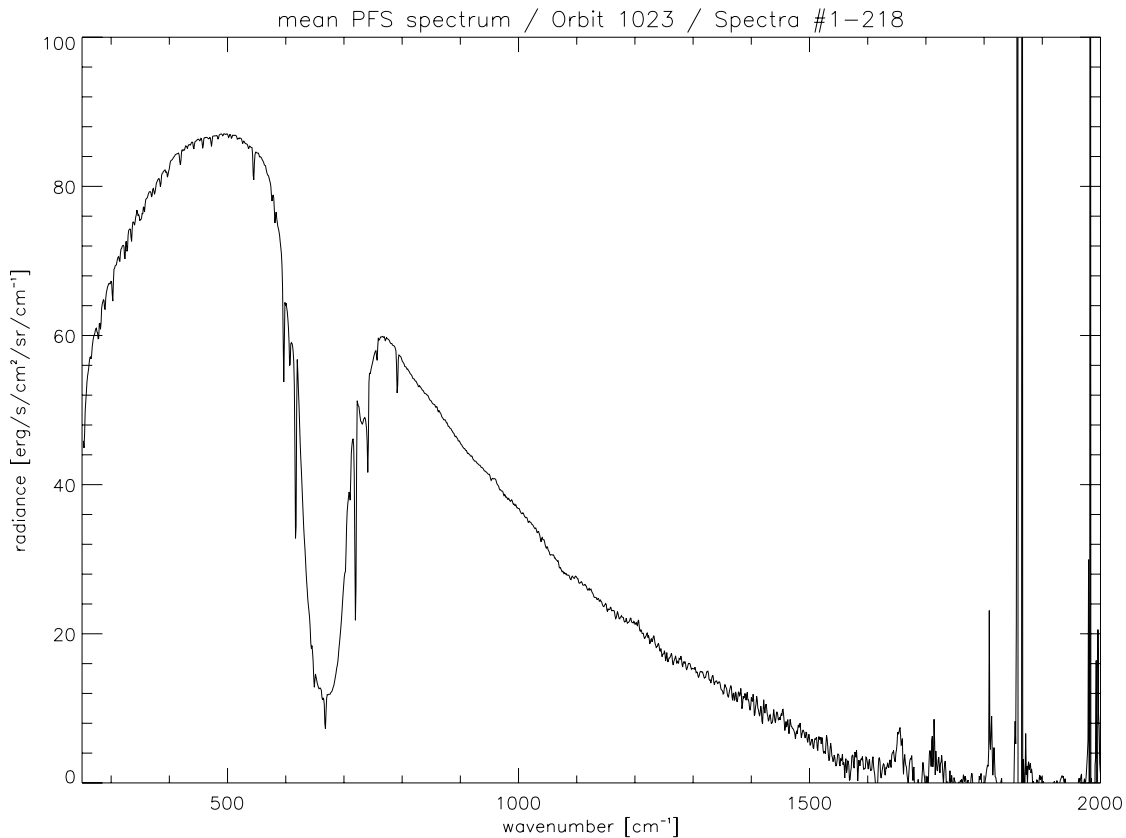


Figure 4.2: Average of 218 LW spectra of orbit 1023: the thermal radiation of Mars follows the typical Planck curve with the broad  $15\ \mu\text{m}$  ( $667\ \text{cm}^{-1}$ ) absorption band of  $\text{CO}_2$ , including the Q-branches in its wings. Water lines are found in the region below  $400\ \text{cm}^{-1}$  and above  $1400\ \text{cm}^{-1}$ . The noise at wavenumbers higher than  $\sim 1500\ \text{cm}^{-1}$  is due to vibrations of the spacecraft.

### 4.3 PFS in-flight performance

Because only the SW channel was used for this work the following description of relevant calibration issues and in-flight performance will also only concentrate on the SW as reported by Giuranna et al. (2005). The noise equivalent radiance (NER) being defined as the measurement noise (one sigma level) divided by the instrument responsivity has in the range of the  $2.6\ \mu\text{m}$   $\text{H}_2\text{O}$  band an average of  $0.02\ \text{erg/s/cm}^2/\text{sr/cm}^{-1}$  for the operations on Mars. The entire spectral behaviour is shown in figure 4.5. Therefore the signal-to-noise (S/N) ratio was expected to span from 10 at  $8000\ \text{cm}^{-1}$  to 100 at  $2700\ \text{cm}^{-1}$  for an individual spectrum (Formisano et al. 2005). However, the generally detected signal strength on Mars is lower than anticipated. Hence the real S/N ratio is also lower (for an individual spectrum: mean  $\text{S/N}=4.6$ , maximum  $\text{S/N}=14.3$ ). The reason for this are vibrations of the spacecraft that result in less power reaching the detector because of misalignment of the optics and the offset of the laser beam with respect to the central measurement light beam (cf. Comolli and Saggin (2005)). Therefore, to increase the S/N ratio, several spectra have to be averaged.

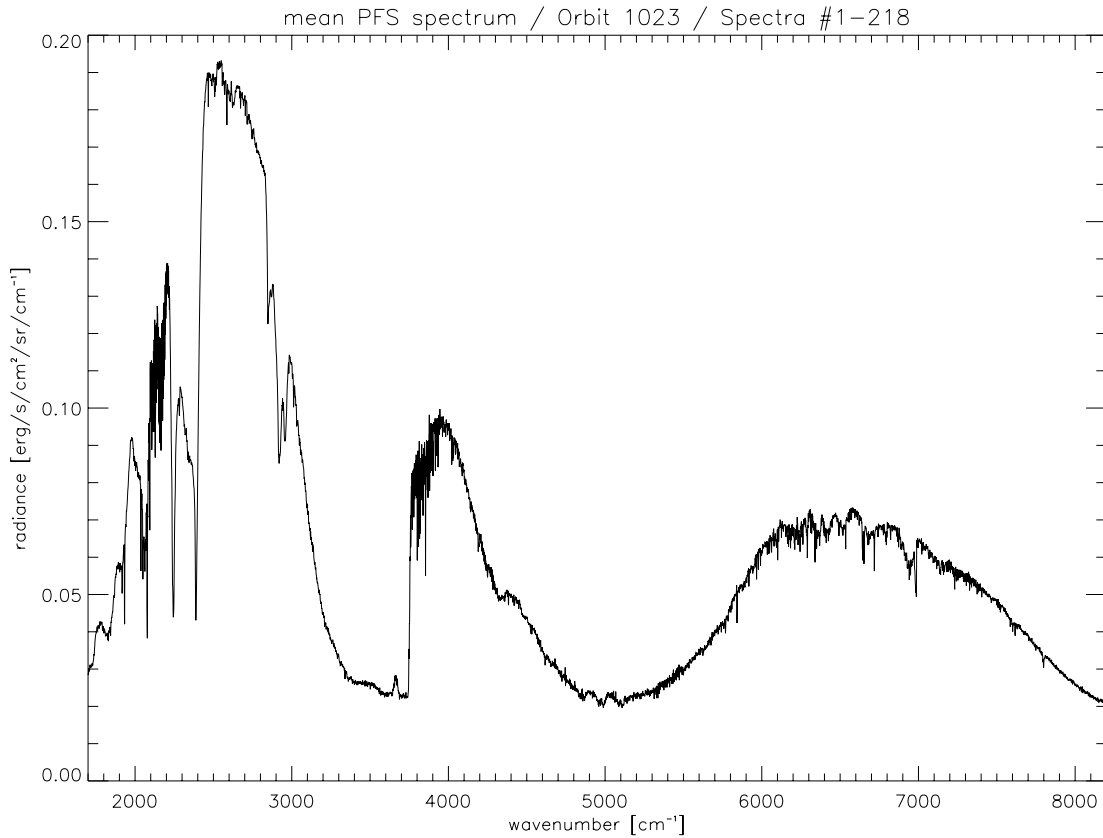


Figure 4.3: Average of 218 SW spectra of orbit 1023: in reflected sunlight there are also the CO<sub>2</sub> bands at 4.3  $\mu\text{m}$ /2325  $\text{cm}^{-1}$  and 2.7  $\mu\text{m}$ /3700  $\text{cm}^{-1}$  prominent. Yet in the case of PFS the one at 2.0  $\mu\text{m}$ /5000  $\text{cm}^{-1}$  is invisible because of spacecraft vibrations which cause the low frequency wavelike distortion between 4000  $\text{cm}^{-1}$  and 8000  $\text{cm}^{-1}$ . The same is true for the water bands at 1.87  $\mu\text{m}$ /5350  $\text{cm}^{-1}$  and 1.38  $\mu\text{m}$ /7250  $\text{cm}^{-1}$  while the 2.6  $\mu\text{m}$ /3850  $\text{cm}^{-1}$  band is in an unaffected part. The feature around 2900  $\text{cm}^{-1}$  is caused by a contamination of the pointing mirror.

The laser diodes providing the operations input for the instrument are dependent on the thermal conditions of PFS. So to have a constant laser wavelength the temperature of the laser diodes (LDT) has to be stable and well known. From the start of the mission the nominal operations scenario was implemented. Hence the SW channel was driven by the SW diode whose temperature can be converted into the used reference laser wavelength by:

$$\lambda[\text{mm}] = 8.01631 \cdot 10^{-5} \cdot T[\text{K}] + 1.16774$$

However, after orbit 634 the pendulum motor was solely driven by the laser diode of the LW channel because by switching off the SW laser diode the noise for interferograms is significantly reduced (Formisano et al. 2005). The corresponding formula for the conversion of the LW laser diode temperature into the reference wavelength is (private communication, Giuranna 2006):

$$\lambda[\text{mm}] = 6.06520 \cdot 10^{-5} \cdot T[\text{K}] + 1.19203 \quad (4.1)$$

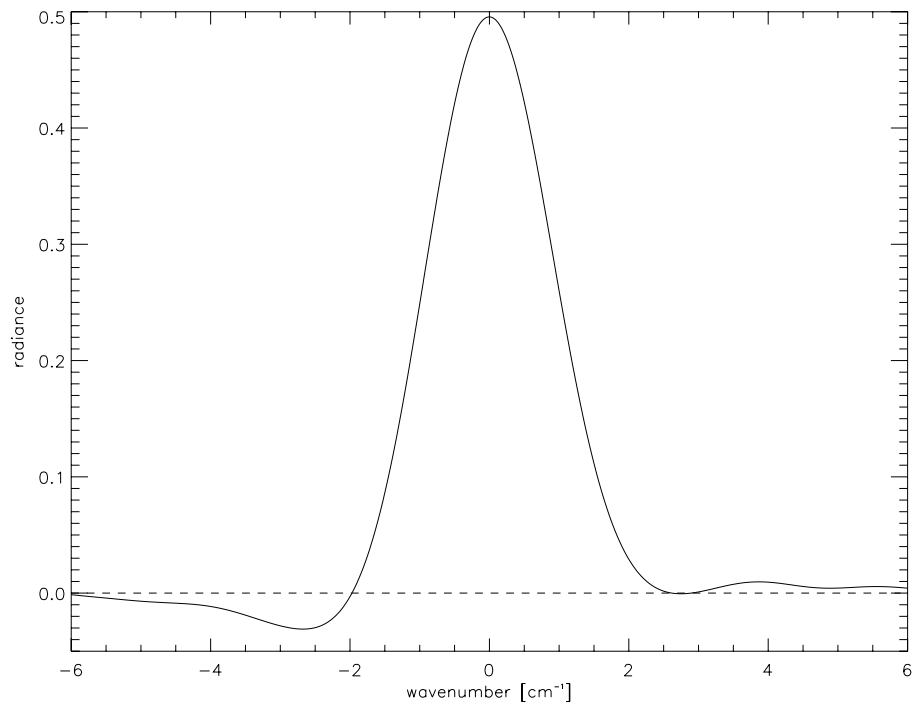


Figure 4.4: The asymmetric PFS monochromatic transfer function with Hamming apodization has a spectral resolution with a FWHM of  $2.04 \text{ cm}^{-1}$ .

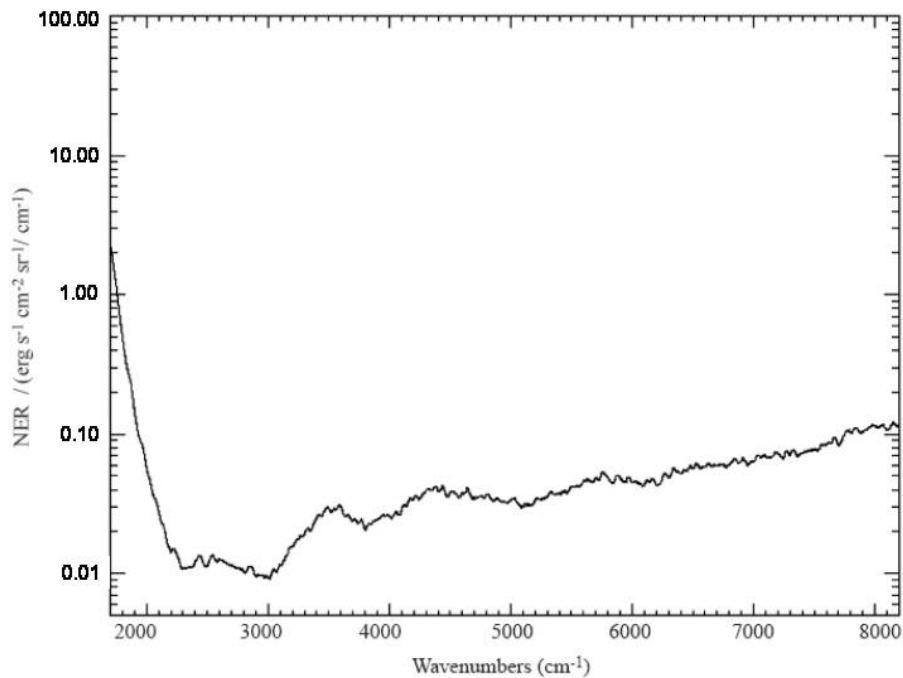


Figure 4.5: The NER spectrum for Mars operations, adopted from Giuranna et al. (2005).

The main cause for this SW diode induced noise and strong resonances at certain wavelengths are microvibrations induced by the spacecraft's mechanically moving parts like reaction wheels, actuators, rotating solar panels and other instruments (Comolli and Saggin 2005). Yet the problem could be overcome by changing the driving speed of the pendulum motor from 2000 Hz to 2500 Hz.

Two other problems that occurred most likely during the launch of MEX have also become visible in the near-Earth calibration phase. One is the contamination of the pointing mirror at the aperture of the instrument which causes an absorption-like disturbance of the spectrum between  $2800\text{ cm}^{-1}$  and  $3000\text{ cm}^{-1}$  (see figure 4.3). The second problem is much more problematic, though. Apparently the optical alignment of the internal calibration lamp was lost during launch. Therefore the absolute radiative calibration of the martian spectra is not possible.

Later in the MEX mission, operations had to be entirely stopped on August 30<sup>th</sup>, 2005 due to an errant behaviour of the joint pendulum motor that accumulated in the weeks before. After a switch to the backup motor the observations could be resumed on November 2<sup>nd</sup>, 2005. Hence there are no available data covering the southern hemisphere winter between  $L_S=255^\circ$  and  $L_S=318^\circ$ .

In conclusion, there are three causes for instrumental uncertainties that have to be taken into account: a random noise due to the spectral responsivity, problems with radiometric calibrations, and the influence of vibrations. The last one can on the one hand be clearly seen, like in figure 4.3, but on the other hand also the apparently not affected ranges might suffer from unknown effects. To mediate these problems in the water retrieval process (explained in chapter 5.2) it was decided to use relative band depths, meaning the ratio of band depth to continuum, and to work with averaged spectra.

## 4.4 PFS observations and spectrum averaging

PFS started to take scientific data on January 10<sup>th</sup>, 2004 in orbit 10 ( $L_S=331^\circ$ ). After the calibration phase the instrument was successfully operating on 732 out of the 1684 orbits considered for this work and producing about 82 Gbit of data. The largest gaps in seasonal coverage are due to the activation and subsequent calibration of the MARSIS radar in May 2005 and the previously mentioned problem with the pendulum motor in autumn of 2005. The first operation implicated only sparse data acquisition between  $L_S=196^\circ$  and  $L_S=273^\circ$  due to telemetry restrictions. The latter problem prolonged this lack of data until  $L_S=318^\circ$ . Thus the last orbit whose data were processed for this work was number 1609 at  $L_S=196^\circ$  (April 18<sup>th</sup>, 2005). Despite the fact that PFS is operating smoothly since the large gap the data taken afterwards were not processed. The reason for this is that until recently there was no information about the observational geometry available.

In the beginning of the mission there were calibrated PFS/SW data provided by the team of the principal investigator (incompletely up to orbit 731). However, due to the problems with absolute calibration only uncalibrated data were provided for the rest of the mission and thus used for this analysis.

As mentioned above, for the creation of a single mean spectrum, which is later on called datapoint, several measurements have to be averaged. The optimum averaging

number was found to be 15 because this is a good compromise between an enhancement of signal-to-noise ratio (factor of  $\sim 4$ ) and maintenance of high spatial resolution with about  $0.8^\circ$  to  $2^\circ$  in latitude per datapoint, depending on the spacecraft altitude. This is equal to an effective footprint of 50 to 120 km on the surface. Of course also the provided geometry information (Maturilli et al. 2002) on the point in time and space is averaged. For a single orbit this sliding window of 15 is shifted over the individual observations as long as they have a low enough airmass (this quantity is explained in chapter 5.3.2 on page 61). In between there is a step of 4, i.e. average spectra are constructed from observations 1–15, 5–19, 9–23, .... and so on. So in general for each orbital dataset there are about 15 to 20 averaged spectra available. The smoothing effect of building a mean spectrum is presented in figure 4.6: the left panel shows the apodized PFS observation number 68 of orbit 278; the right panel is the average of observations 61 to 75. Clearly the scattering and spikes are reduced in the mean spectrum.

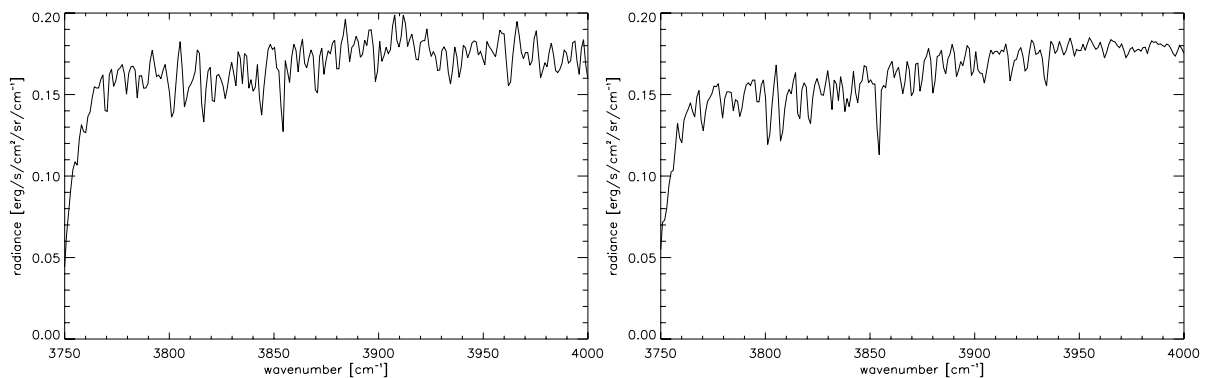


Figure 4.6: To show the necessity of spectrum averaging a single spectrum (left panel) is displayed next to an average of 15 spectra (right panel). The single spectrum is observation number 68 of orbit 278 while the average is of numbers 61–75.

Now for the presented work 21 819 datapoints were created in total using observational spectra from orbit 10 to 1609 with good quality and good observational conditions. The orbits cover the season between  $L_S=331.2^\circ$  of MY 26 and  $195.3^\circ$  of MY 27. The mean signal-to-noise ratio of a datapoint is approximately 18 but with a very high scattering. Since the *MEX* instruments are only active during pericenter passes there is a seasonal shift of the acquired data over local time. Figure 4.7 shows this evolution of coverage for the processed datapoints, including their signal-to-noise ratios.

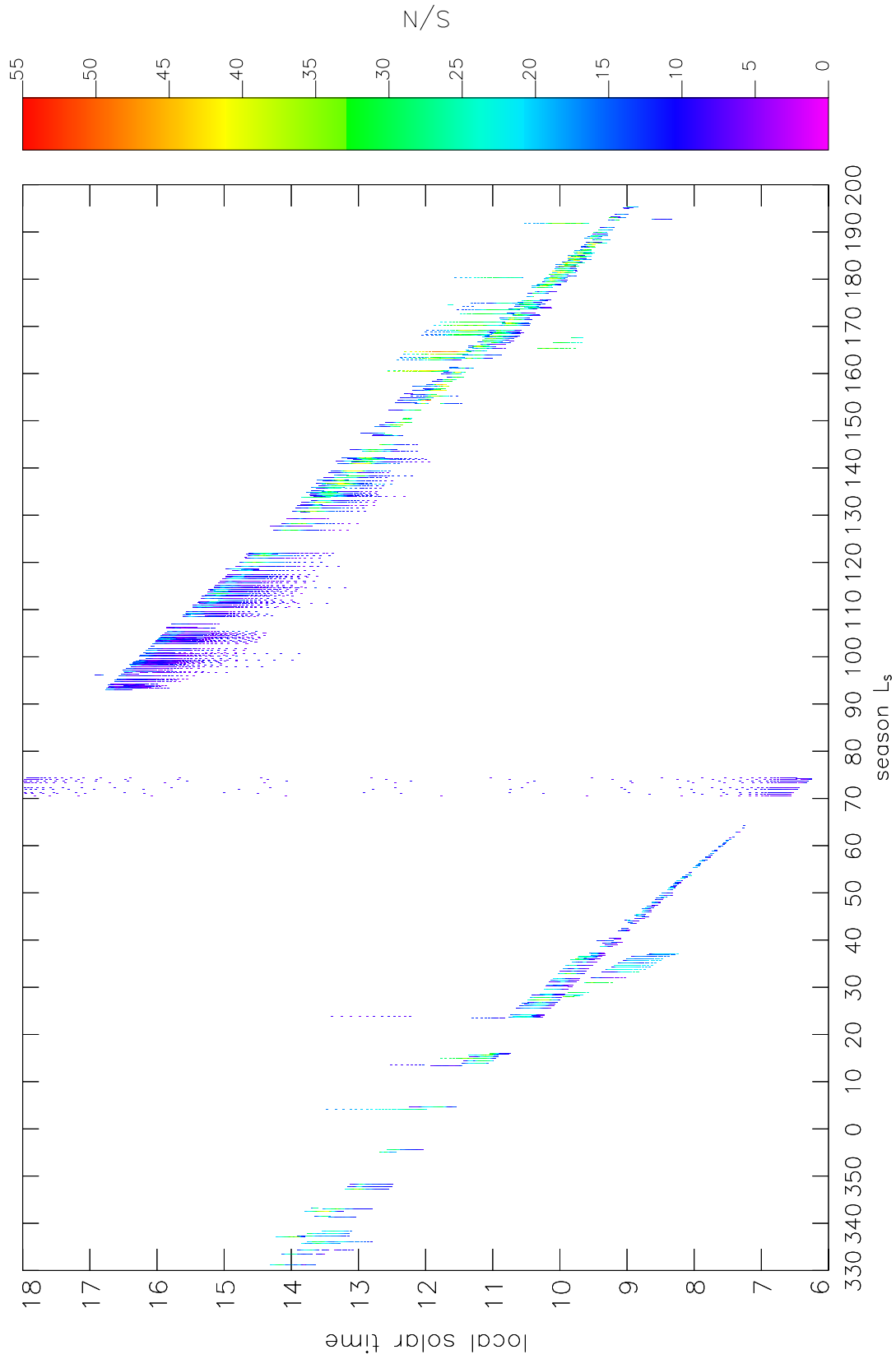


Figure 4.7: The PFS coverage of local solar time versus season  $L_s$  of all datapoints and their corresponding signal-to-noise ratio.



## 5 Data analysis

Although PFS covers a large wavelength range with several water absorption bands for this work only the 2.6  $\mu\text{m}$  band was used because it is expected to be free of mineralogical features. In addition, the other SW bands are not suitable for retrievals, as explained in the previous chapter, and the PFS/LW is analysed by an independent team (Fouchet et al. 2006). Compared to the LW channel the advantage of the 2.6  $\mu\text{m}$  band is the relatively weak dependence of the spectral lines of the thermal structure of the atmosphere since it is part of the reflected solar light. This fact also allows retrievals over cold surfaces like the poles. However, at the poles the high incidence angle of the radiation often causes a low signal strength. In this chapter the performed reduction and analysis of the PFS/SW spectra are described.

### 5.1 Introduction to spectroscopy

For the following descriptions several spectroscopic terms will be required which makes a brief introduction into this field inevitable. The general description of infrared radiation measured by a detector orbiting a planet starts from the fundamental radiative transfer equation:

$$\mu \frac{dI_v(\tau, \mu, \varphi)}{d\tau_v} = -I_v(\tau, \mu, \varphi) + S_v \quad (5.1)$$

Here  $I_v(\tau, \mu, \varphi)$  is the monochromatic intensity after a single passage through an atmosphere of optical depth  $\tau$  into the observers's direction determined by the cosine of the zenith angle  $\mu = \cos \theta$  and the azimuth angle  $\varphi$ . The optical depth which is in turn dependent on the wavelength is defined as the vertical integral over the extinction coefficient  $k_v$  from the atmospheric level  $z$  to the top of the atmosphere

$$\tau_v(z) = \int_z^\infty n(z') k_v(z') dz' \quad (5.2)$$

with  $n(z')$  the molecule density at the atmospheric level  $z'$ . How the optical depth is being calculated will be subject of the following section 5.3.2.

The last term of equation 5.1 is the monochromatic source function  $S_v$  determining how much radiation is emitted and absorbed between the source and the receiver. In the case of a planetary atmosphere it is a combination of the thermal emission of the atmosphere  $I_{TA}$  and radiation originating from three forms of scattering. Those are first the solar radiation  $I_{sun}$  which is backscattered at a certain level, second the single scattering of radiation from the background source ( $I_{SS}$ ) and third the multiple scattering ( $I_{MS}$ ) of

photons before propagating into the  $(\theta, \varphi)$ -direction. The formal solution of equation 5.1 is

$$I_\nu(\tau_\nu(\infty), \mu, \varphi) = I_\nu(\tau_\nu(0), \mu, \varphi) \cdot e^{-\tau_{\nu, total}/\mu} + \int_{\tau_\nu(\infty)}^{\tau_\nu(0)} S_\nu(\tau_\nu) \cdot e^{-(\tau_\nu - \tau_\nu(\infty))/\mu} d\tau_\nu \quad (5.3)$$

where  $\tau_{\nu, total} = \tau_\nu(0) - \tau_\nu(\infty)$  is the total optical depth between the surface (at level 0) and the top of the atmosphere (at infinity). Hence  $\tau_\nu(\infty)$  is generally zero.

In the equation the first term describes the attenuation of the background source by the transmittance function  $exp(-\tau_{\nu, total}/\mu)$ . For optically thin atmospheres this source is both the blackbody radiation of the planet and sunlight reflected off the surface. Depending on the part of the infrared spectrum, thermal or non-thermal, either one of those or even both have to be taken into account. The second term of the equation treats the complex interplay between emission, scattering, and attenuation of radiation in the atmosphere. A detailed mathematical formulation of this general solution, including the source function  $S_\nu = I_{TA} + I_{sun} + I_{SS} + I_{MS}$  in an explicit way, can be found in Hanel et al. (2003). For our work any scattering was neglected which sets the source function to zero. Furthermore, the  $2.6 \mu\text{m}$  water band is in an IR region where the thermal emission is negligible to first order because its maximum is roughly around  $17 \mu\text{m}$  for Mars (covered by the LW channel) which makes the solar radiation the only background source. Out of this reason the solution to the radiative transfer equation is simplified to:

$$I_\nu(\tau_\nu(\infty), \mu, \varphi) = I_{sun}(\tau_\nu(0), \mu, \varphi) \cdot e^{-\tau_{\nu, total}/\mu} \quad (5.4)$$

with  $I_{sun}(\tau_\nu(0), \mu, \varphi)$  the intensity of the solar radiation as it is reflected from the surface<sup>1</sup>. For planetary observations this reflected solar light resembles the solar constant (outside the atmosphere) attenuated by the passage through the atmosphere and by the absorption from the surface.

All the monochromatic intensities form the infrared spectrum where absorption lines – and in principle also emission lines – are present. In the IR the lines are produced by vibrational transitions combined with rotational ones (for water lines in the SW range see appendix A.2). In case individual lines can spectroscopically be resolved they show their typical Voigt profile. It is a convolution of the Gaussian-shaped Doppler function which dominates the line center and the Lorentz line profile that shapes the wings of a spectral line. The first one is due the influence of temperature  $T$  on the velocity distribution of the molecules and the resulting Doppler broadening of the natural line width. The Lorentz function is mainly governed by the pressure  $p$  of the medium that causes molecular collisions and has the following form:

$$\mathcal{F}_{L_i}(p, T, \nu) = \frac{1}{\pi} \cdot \frac{\Gamma_{L_i}}{(\nu - \nu_{0_i})^2 + \Gamma_{L_i}^2} \quad (5.5)$$

Here  $\nu_{0_i}$  denotes the wavenumber of the line center and  $\Gamma_{L_i}$  the FWHM of the line which can be written more explicitly as

$$\Gamma_{L_i}(p, T) = \Gamma_{0_i} \cdot \frac{p}{p_0} \cdot \left(\frac{T_0}{T}\right)^{\beta_i} \quad (5.6)$$

---

<sup>1</sup>In general, the more correct term would be the layer where the medium becomes optically thick, e.g. also a layer of suspended aerosols.

with  $\Gamma_{0_i}$  the FWHM at basic conditions ( $p_0, T_0$ ). The exponent  $\beta_i$  is a matter of determination in the laboratory. Thus for practical computations this parameter has to be taken from catalogues of spectral lines, e.g. the HITRAN or GEISA databases<sup>2</sup>.

Finally, the inclusion of the Doppler profile yields the Voigt profile. This more precise description of a spectral line is written as:

$$\mathcal{F}_{V_i}(p, T, \nu) = \frac{\sqrt{\ln 2} \cdot a}{\pi^{3/2} \cdot \Gamma_D} \cdot \int_{-\infty}^{\infty} \frac{\exp(-y^2) dy}{(x - y)^2 + a^2} \quad (5.7)$$

with

$$x = \frac{(\nu - \nu_{0_i}) \sqrt{\ln 2}}{\Gamma_D}, \quad a = a(p, T) = \frac{\Gamma_{L_i} \sqrt{\ln 2}}{\Gamma_D}$$

and the FWHM of the Doppler function  $\Gamma_D$ , given by:

$$\Gamma_D = 3.58 \cdot 10^{-7} \cdot \nu_{0_i} \sqrt{\frac{T}{m}}$$

where  $m$  is the molecular weight of the molecules.

## 5.2 The retrieval algorithm and the preparation of the PFS measurements

For the aim of retrieving the water vapour column density of an averaged spectrum a procedure was developed that consists of the following main steps:

1. Extraction of a vertical temperature and pressure profile from the European Mars Climate Database (EMCD, version 4.1, described in appendix A.3) for the given time and location
2. Line-by-line calculation of monochromatic opacities both for CO<sub>2</sub> and H<sub>2</sub>O under consideration of saturating conditions
3. Convolution of the created transmittance spectrum with the solar spectrum and the PFS instrumental function
4. Normalization of both the synthetic spectrum and the averaged PFS spectrum
5. Finding the H<sub>2</sub>O mixing ratio (below the saturation level) which yields the best fit and correction of the PFS continuum in the corresponding way

These steps will be described in sections 5.3 to 5.5 in greater detail. Please note that the influence of dust has not been incorporated in the procedure because a dust-free atmosphere was assumed and the considered airmasses were low (generally 3.1, in special cases 3.7).

Before the start of the retrieval algorithm two things have to be done to prepare the PFS spectra for analysis. First, it is necessary to increase the signal-to-noise ratio which

---

<sup>2</sup>The **H**igh-resolution **T**ransmission molecular absorption database, version 12, contains 1 734 469 spectral lines for 37 different molecules. GEISA contains 702 550 spectral lines of 14 molecules.

is proportional to  $\sqrt{n}$  of the number of spectra  $n$ . Thus a mean PFS spectrum out of 15 individual spectra is created and forms a so-called datapoint (explained in chapter 4.4).

The second issue is that after orbit 634 the motion of the SW pendulum is controlled by the LW laser diode (see chapter 4.3). Out of this reason the PFS spectrum appeared shifted with respect to the synthetic spectrum. This shift differs between individual orbits in an inconsistent way but is relatively stable within the observation run of a single orbit. As a consequence the H<sub>2</sub>O retrieval would give incorrect results. So to correct this problem the wavenumber grid has to be tuned by changing the laser diode temperature (LDT) in formula 4.1 (page 49). This is done before the actual retrieval algorithm by calculating synthetic spectra for the water mixing ratio estimated by the EMCD and for different laser diode temperatures separated by 0.1 K in the range between 284 K and 289 K. The optimum LDT is then determined as the one belonging to the synthetic spectrum which fits the measured spectrum in the best way (same criterion as described later in chapter 5.5). The measure of the LDT adjustment was performed on the entire processed dataset, even for the orbits earlier than number 634 in order to optimize the achieved fit quality.

## 5.3 The synthetic spectrum

### 5.3.1 Vertical atmospheric profiles

Before the creation of a synthetic spectrum is possible all the input parameters have to be known. For a single datapoint of PFS measurements they are as follows. Both the spatial coordinates (latitude and longitude) and the point in time (solar longitude and martian local time) of the individual spectra are binned to mean values which are used to calculate the surface altitude from the MOLA  $1/4^\circ \times 1/4^\circ$  database and to provide input for the EMCD, version 4.1. For the provided coordinates this global circulation model yields a temperature and pressure profile with in our case 56 defined layers. The vertical resolution of the profile increases from the upper atmosphere with 4 km resolution in 120 km altitude towards the surface where the resolution is 5 m.

At this point a focus on the behaviour of water vapour, and especially its vertical distribution, is necessary which is described in detail in Bohren and Albrecht (1998). Although from daily life one is used to the term relative humidity to quantify water in the air it is not used as a scientific expression. The measurement units used in this work – mixing ratio and column density – are explained in appendix A.4. The H<sub>2</sub>O vapour pressure  $p_g$  can vary between zero and a maximum value, known as the saturation pressure  $p_s$ . That term is defined as the pressure where the gaseous water is in equilibrium with the liquid or solid phase for the given temperature condition. Recent measurements by Mauersberger and Krankowsky (2003) for low temperatures  $T$  [K] provided two relations which were used to determine the saturation pressure over ice in this work (given in [Pa]):

$$\begin{aligned} 169\text{K} \leq T \leq 273.15\text{K} : \quad \log p_s &= -\frac{2663.5 \pm 0.8}{T} + (12.537 \pm 0.011) \\ 164.5\text{K} \leq T < 169\text{K} : \quad \log p_s &= -\frac{3059 \pm 26}{T} + (14.88 \pm 0.15) \end{aligned} \quad (5.8)$$

These are the special solutions of the Clausius-Clapeyron equation for water vapour pres-

sure over ice which has the general form:

$$p_S = C \cdot \exp\left(-\frac{m_w L_v}{kT}\right)$$

where  $C$  is a constant,  $m_w$  the molecular mass of water,  $L_v$  the enthalpy of sublimation per unit mass and  $kT$  the average molecular kinetic energy. Now the altitude in the atmosphere where the partial pressure equals the saturation pressure is called saturation or condensation level. One has to keep in mind, though, that this is only correct if there are condensation nuclei present where the vapour can condense. In case of their absence a higher vapour pressure is feasible which makes the air supersaturated. However, planetary atmospheres provide generally plenty of condensation nuclei in the form of aerosols.

Therefore the thermal structure of the atmosphere, the microphysics of nucleation, and the formation of suspended ice crystals along with turbulent mixing and large-scale atmospheric motion determine the vertical distribution of water vapour. On Mars it was believed that vapour is uniformly mixed within the atmosphere but as observations have shown there is also a confinement within the lower few kilometers possible. In principle this is spectroscopically measurable by comparison of line strengths of different H<sub>2</sub>O bands. However, in the retrieval procedure of this work the water vapour is ab initio considered as uniformly mixed with carbon dioxide as long as its partial pressure is below the saturation pressure. Above the saturation level in the higher troposphere the mixing ratio is only determined by the saturation pressure.

### 5.3.2 The monochromatic transmittance spectrum

When it comes from theory to real application one has to make certain assumptions and simplifications to make radiative transfer calculations feasible within reasonable computing time consumption. Thus Titov and Haus (1997) developed a fast technique for transmittance calculations which was specifically refined for the application in the *MEX/PFS* mission, both for the LW and SW channels (Haus and Titov 2000). For the purpose of getting the spectral opacities  $\tau_\nu(z)$  of the selected trace gases with equation 5.2 their monochromatic absorption coefficient  $k_\nu(z)$  has to be calculated. Basically it is dependent on pressure, temperature, and wavenumber:

$$k(p, T, \nu) = \sum_i Q_i(T) S_i(T) \mathcal{F}_i(p, T, \nu) \chi(\nu - \nu_{0i}) = \sum_i A_i(T, \nu) \mathcal{F}_i(p, T, \nu) \quad (5.9)$$

with the suitable form function  $\mathcal{F}_i(p, T, \nu)$  which has either Lorentz (equation 5.5) or Voigt (equation 5.7) shape, the product of vibrational and rotational energy states  $Q_i(T)$ , the temperature-depending line intensity  $S_i(T)$  and also a factor  $\chi(\nu - \nu_{0i})$  for possibly necessary corrections of the absorption cross section in case of deviation from nominal conditions. In the following the last three terms are combined into one term  $A_i(T, \nu)$ . Now the trick to avoid the complex calculation of  $k(p, T, \nu)$  is done by separating the variables and turning the absorption cross section into a product of two functions

$$k(p, T, \nu) = G(p) \cdot F(T, \nu) = \frac{p}{p_0} \cdot F(T, \nu) \quad (5.10)$$

To achieve this in the case of the Lorentz halfwidth, which is also dependent on pressure according to equation 5.6, one has to assume a pressure model  $p_M(T)$  depending on temperature. Also for weak lines it is necessary to take into account the precise line shape and pursue correct calculations. With this pressure assumption the Lorentz FWHM becomes

$$\Gamma_{L_i}(T) = \Gamma_{0_i} \cdot \frac{p_M(T)}{p_0} \cdot \left(\frac{T_0}{T}\right)^{\beta_i} \quad (5.11)$$

and turns the above factor  $F(T, \nu)$  into:

$$F(T, \nu) = \frac{1}{\pi} \cdot \sum_i A_i(T, \nu) \left(\frac{T_0}{T}\right)^{\beta_i} \frac{\Gamma_{0_i}}{(\nu - \nu_{0_i})^2 + \Gamma_{L_i}^2(T)} \quad (5.12)$$

As for the error induced to the transmittance due to an insufficiently determined temperature profile Titov and Haus (1997) conclude that it is negligible in the case of Mars. For the Voigt profile the separation of variables can be performed, too. The use of the same pressure model  $p_M(T)$  allows one to transform the factor  $a$  in the Voigt function 5.7 into  $a(p, T) = a(p_M(T), T) = a_M(T)$  being only dependent on the temperature. Thus

$$\mathcal{F}_{V_i}(p, T, \nu) = \frac{p}{p_0} \cdot \frac{\ln 2 \cdot \Gamma_{0_i}}{\pi^{3/2} \cdot \Gamma_D^2} \cdot \left(\frac{T_0}{T}\right)^{\beta_i} \cdot \int_{-\infty}^{\infty} \frac{\exp(-y^2) dy}{(x - y)^2 + a_M^2} \quad (5.13)$$

Now the absorption coefficient at wavenumber  $\nu_j$  caused by many individual lines can be calculated (line-by-line model). For this purpose a matrix  $F(T_i, \nu_j)$  with  $i$  temperature steps is created. All values for temperatures  $k$  in between are gained by linear interpolation between the  $T_i$  levels. Therefore the absorption coefficients are

$$k(p, T_k, \nu_j) = \frac{p}{p_0} \cdot \text{interpolation}\langle F(T_i, \nu_j) \rangle \quad (5.14)$$

and they can be calculated very rapidly with the use of the look-up matrix that has to be computed only once. Particularly for this work the calculated spectral stepsize is the highest with  $0.01 \text{ cm}^{-1}$  in the line centers decreasing towards the flanks. The calculations for an individual wavenumber were performed until a cutoff distance of  $50 \text{ cm}^{-1}$  to the red and blue side. Altogether this sums up to 55 710 wavenumber steps between  $3700 \text{ cm}^{-1}$  and  $4100 \text{ cm}^{-1}$  and 10 temperature points between 120 K and 300 K. The line strengths and widths for  $\text{H}_2\text{O}$  and  $\text{CO}_2$  were taken from the HITRAN 2004 database (Rothman et al. 2005).

Finally an important issue for atmospheric sounding of terrestrial planets apart from Earth has to be mentioned. All the spectral line databases are created for an atmosphere with terrestrial composition. Hence for other planets like Mars with its  $\text{CO}_2$ -dominated air there has to be a correction introduced, namely the line broadening parameter. This factor determines by how much the line width has to be increased. For this work it was set to 1.5, according to the values calculated by Gamache et al. (1995). However, one has to keep in mind that the precise value is unknown and even different from line to line.

The last procedure before the creation of a transmittance spectrum  $T(\nu)$  is the calculation of the optical depth  $\tau(\nu)$  for each considered atmospheric constituent  $i$  with equation 5.2. Then those optical depths are in turn multiplied with the mixing ratio  $f_i$  of the

corresponding gas and finally summed up in the following equation:

$$T(\nu) = \exp \left[ -\alpha \cdot \left( \sum_i f_i \cdot \tau_i(\nu) \right) \right] \quad (5.15)$$

Here the factor  $\alpha$  denotes the airmass which is a measure for the pathlength through an atmosphere covered by a ray of light from source to detector. Because it is calculated as the angular distance from zenith ( $\mu = \cos \theta$ ) for spacecraft observations both the incidence angle onto the surface  $\theta_{in}$  and the emission angle towards the detector  $\theta_{em}$  are relevant. Thus in first order the airmass is given by:  $\alpha = (1 / \cos \theta_{in}) + (1 / \cos \theta_{em})$ .

At this point it is important to note that equation 5.15 is only correct for homogeneous gas mixing without saturation. With the presence of a condensation level the vertically changing mixing ratio is incorporated in the molecule density  $n(z')$  in equation 5.2. In this case the optical depths depend on the vertical gas distribution and are simply summed up and multiplied with the airmass to form the transmittance spectrum.

### 5.3.3 Convolution with solar spectrum and instrumental function

In the 2.6  $\mu\text{m}$  region only  $\text{CO}_2$  and  $\text{H}_2\text{O}$  play a role and the atmospheric profiles from EMCD are input parameters for the line-by-line calculation of the transmittance spectrum in the range from  $3700 \text{ cm}^{-1}$  to  $4100 \text{ cm}^{-1}$ . In these computations the  $\text{H}_2\text{O}$  mixing ratio  $f_{\text{H}_2\text{O}}$  above the surface is the variable to be determined in the algorithm.

In figure 5.1 the monochromatic transmittance spectrum is displayed individually between  $3820 \text{ cm}^{-1}$  and  $3900 \text{ cm}^{-1}$  for  $\text{CO}_2$  in black and  $\text{H}_2\text{O}$  with a mixing ratio of 500 ppm in blue. The considered airmass is 2.0, the surface temperature 240 K and the pressure 5.8 mbar. A zoom on the same transmittance in the range from  $3850 \text{ cm}^{-1}$  and  $3860 \text{ cm}^{-1}$  is displayed in figure 5.2. Obviously the narrow  $\text{CO}_2$  lines are not saturated here while some of the  $\text{H}_2\text{O}$  are saturated others are not. The saturation depends on the airmass and the mixing ratio, of course. At last, the joint transmittance spectrum for  $\text{CO}_2$  and  $\text{H}_2\text{O}$  convolved with the apodized PFS instrumental response function (see figure 4.4 on page 50) is presented for illustration in figure 5.3, now for 4 mixing ratios: 100 ppm, 200 ppm, 500 ppm and 1000 ppm. When the mixing ratio is increased from 100 ppm to 200 ppm the mean transmittance changes by 1.6% and the maximum by 12%, for the increase from 500 ppm to 1000 ppm the mean transmittance change is 3.3% and the maximum 25%.

In the final step of creating the synthetic spectrum the atmospheric transmittance is multiplied with a high-resolution solar spectrum  $S(\nu)$ , which is corrected for the solar distance and has a grid spacing of  $0.005 \text{ cm}^{-1}$  (Fiorenza and Formisano 2005), the infrared reflectance and the cosine of the incidence angle on the surface – whereas the reflection is assumed to be Lambertian<sup>3</sup>. After that the absolute synthetic spectrum  $I_{\text{synth}}(\nu)$  is created by the convolution of the theoretical spectrum with the apodized instrumental function  $R_{\text{PFS}}$ :

$$I_{\text{synth}}(\nu_0) = \int (T(\nu) \cdot S(\nu)) R_{\text{PFS}}(\nu - \nu_0) d\nu.$$

<sup>3</sup>Lambertian reflectance means isotropic reflectance independent of the angle of view.

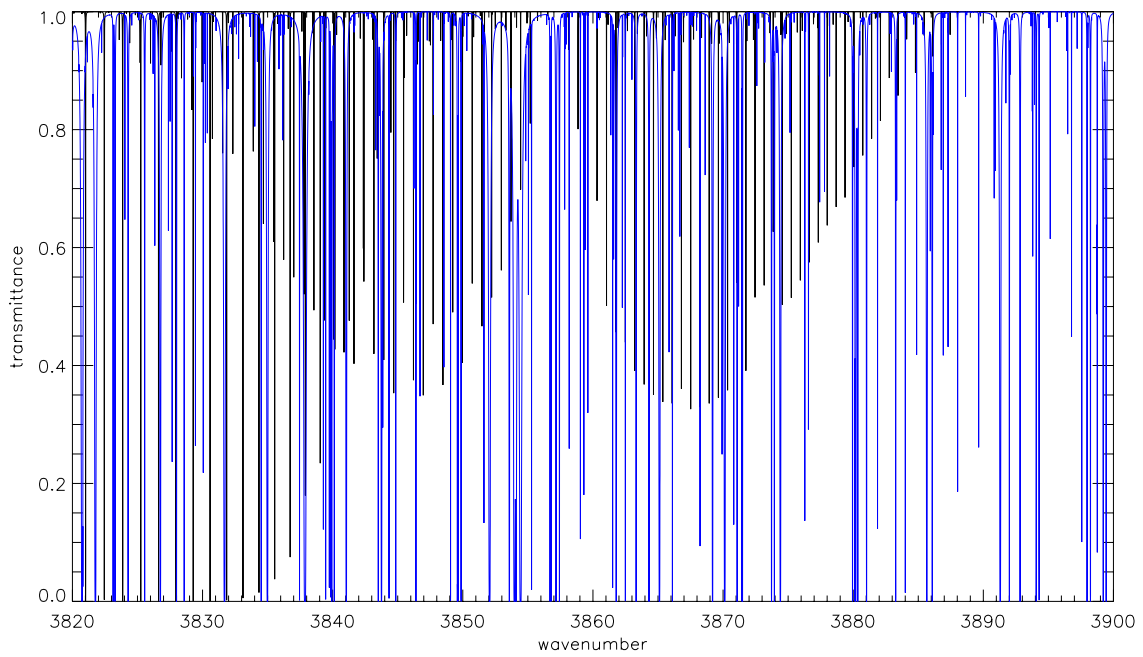


Figure 5.1: The transmittance spectrum for CO<sub>2</sub> (black) and H<sub>2</sub>O with a mixing ratio of 500 ppm (blue) and an airmass of 2 in the wavenumber range from 3820 to 3900 cm<sup>-1</sup>.

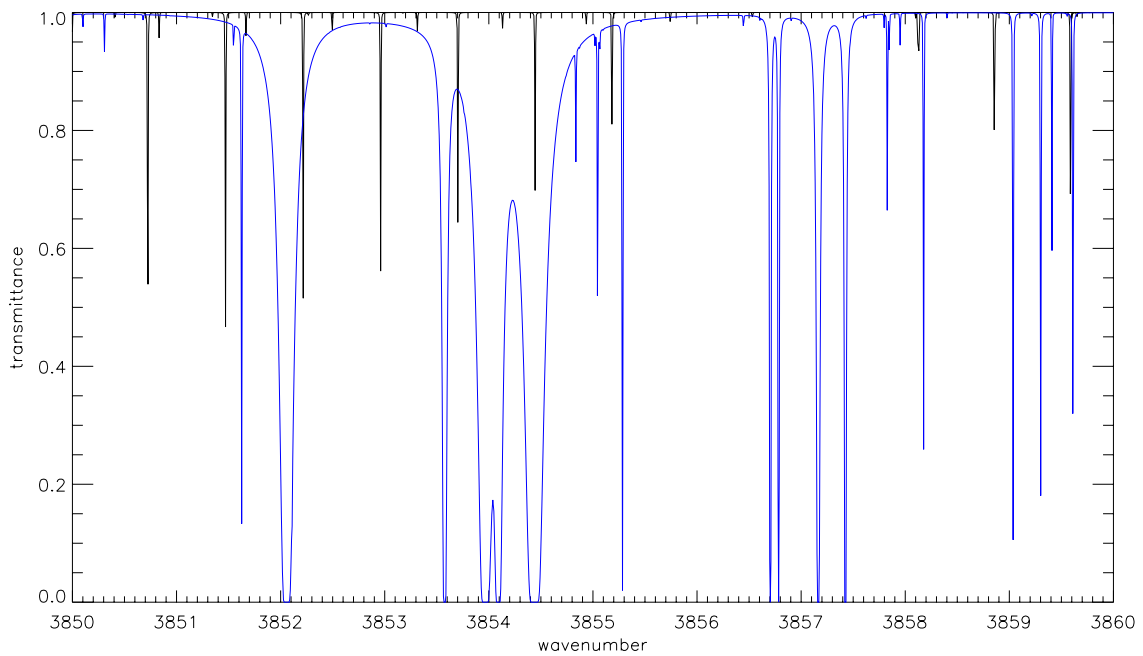


Figure 5.2: The transmittance spectrum for CO<sub>2</sub> (black) and H<sub>2</sub>O with a mixing ratio of 500 ppm (blue) and an airmass of 2 in the wavenumber range from 3850 to 3860 cm<sup>-1</sup>.

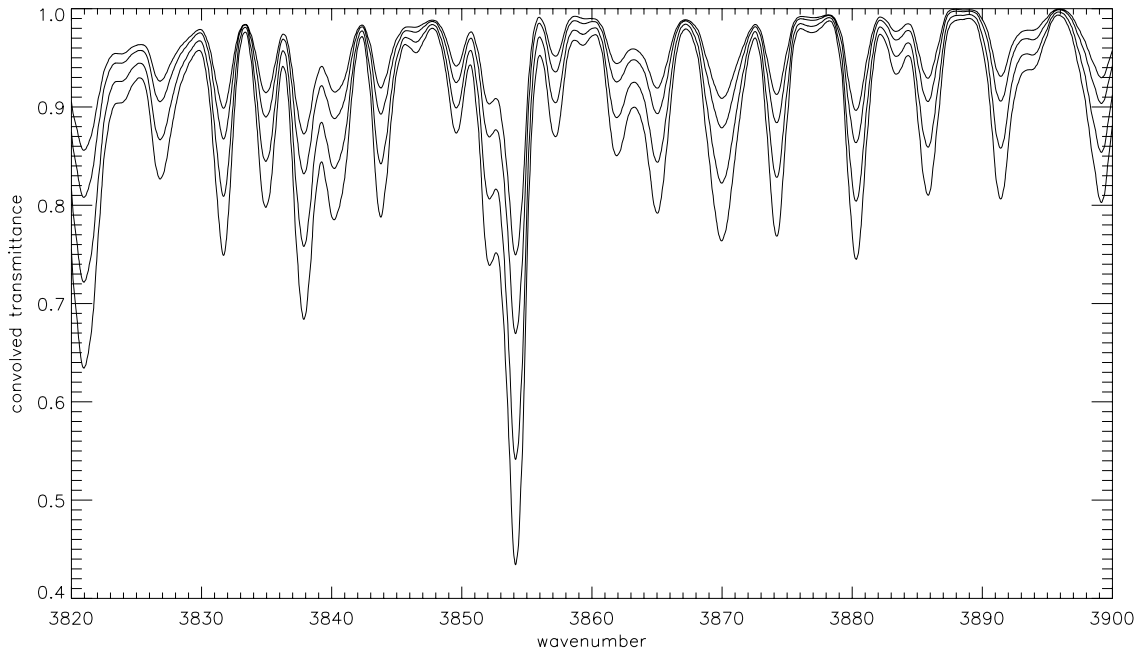


Figure 5.3: The convolved transmittance spectrum (apodized) between  $3820\text{ cm}^{-1}$  and  $3900\text{ cm}^{-1}$  for the mixing ratios 100 ppm, 200 ppm, 500 ppm and 1000 ppm (airmass=2).

## 5.4 Normalization of the spectra

In order to prepare both the synthetic spectrum and the absolute PFS spectrum for the retrieval they are divided by individual continua to get a normalized synthetic spectrum  $N_{synth}(\nu)$  and a normalized measured spectrum  $N_{PFS}(\nu)$ . This measure of normalization was applied because the calibration of the PFS/SW channel did not work after the launch of *MEX* (cf. chapter 4.3). Hence the absolute spectral values are rather uncertain while relative band depths provide a more reliable basis for analysis.

In case of the synthetic spectrum the continuum must fulfill the criterion of being approximately the Planckian solar continuum which is assumed as linear in the considered wavelength range. Thus two points at the edges of that range that are not influenced by  $\text{H}_2\text{O}$  absorption are selected as defining points of the synthetic continuum. In figure 5.4 these points are marked as blue crosses and define the linear continuum (green line) of the solar spectrum, shown in red. The calculated synthetic spectrum (drawn in black) corresponds to a mixing ratio of 300 ppm. The continuum definition points (around  $3774\text{ cm}^{-1}$  and  $3908\text{ cm}^{-1}$ ) have clearly the weakest absorption.

For the normalization process the synthetic spectrum has to be shifted to have the same radiance<sup>4</sup> as the measured one. The responsible parameter is the reflectance  $A$  of the martian surface which can be considered as wavelength-independent because the used wavenumber range is quite narrow. Now first the absolute synthetic spectrum  $I_{syn}$  is corrected for the incidence angle onto the surface ( $\cos \theta_{in}$ ). Then this spectrum and the abso-

<sup>4</sup>Radiometric terminology is explained in appendix A.6.

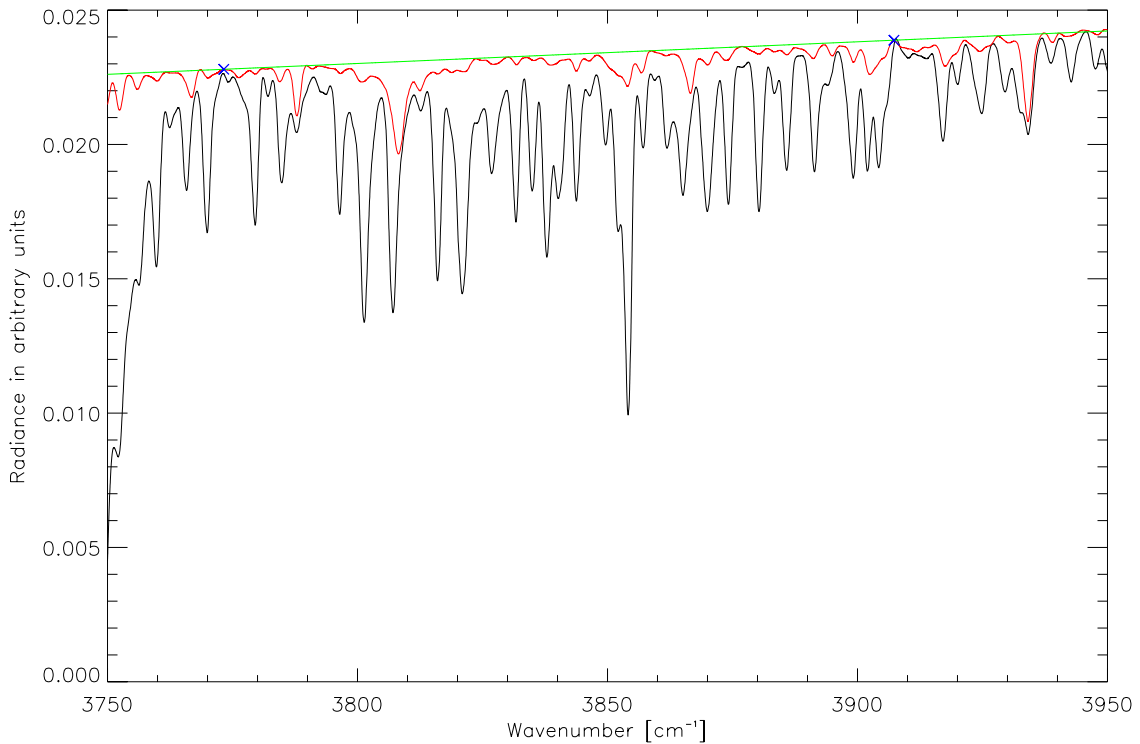


Figure 5.4: Normalization of the synthetic spectrum (black): definition of continuum (green) of the solar spectrum (red) by two points that are not affected by water absorption (blue crosses at around  $3774 \text{ cm}^{-1}$  and  $3908 \text{ cm}^{-1}$ ).

lute PFS spectrum  $I_{PFS}$  are averaged over a certain wavelength range and if the equation  $I_{PFS} = A \cdot I_{syn}$  is satisfied the result is the reflectance  $A$ . This certain wavelength range was selected from  $3860 \text{ cm}^{-1}$  to  $3960 \text{ cm}^{-1}$  because there the water band is not that strong and also shows a periodic behaviour. This provides a reliable mean value. Please note that due to the absence of an absolute calibration the retrieved reflectance values are no real measurements but rather constitute relative differences within individual orbits.

In contrast to that, the continuum of the averaged absolute PFS spectrum  $I_{PFS}(\nu)$  is composed of a piecewise defined function  $C(\nu)$  from local maximum to local maximum. Such a maximum is defined as a spectral point  $\nu_M$  which has a higher radiance than a certain number of its adjacent spectral points<sup>5</sup>. This certain number marks the "strength" of the local maximum and determines the fineness of the piecewise function, i.e. the number of its pieces. Generally the number of 5 points was found to be most reasonable which means that the local maximum is higher than its 5 adjacent points on each side. For example, a number of 6 points would result in a coarser approximation of the PFS spectrum and therefore yield a less accurate fit. Now mathematically the normalized PFS spectrum is created by  $N_{PFS}(\nu) = I_{PFS}(\nu) / C(\nu)$  where the wavenumber gridpoints  $\nu$  are linearly interpolated between the wavenumbers of local maxima  $\nu_M$ . An example of a corrected piecewise continuum is shown in figure 5.5 as the blue curve (the blue crosses mark the continuum definition points). The measured PFS spectrum (red curve) is divided by this

<sup>5</sup>The stepsize of the wavenumber grid is  $1.02 \text{ cm}^{-1}$ .

continuum resulting in the normalized PFS spectrum (green curve). Please note that the shown continuum is corrected which will be explained in the next section 5.5.

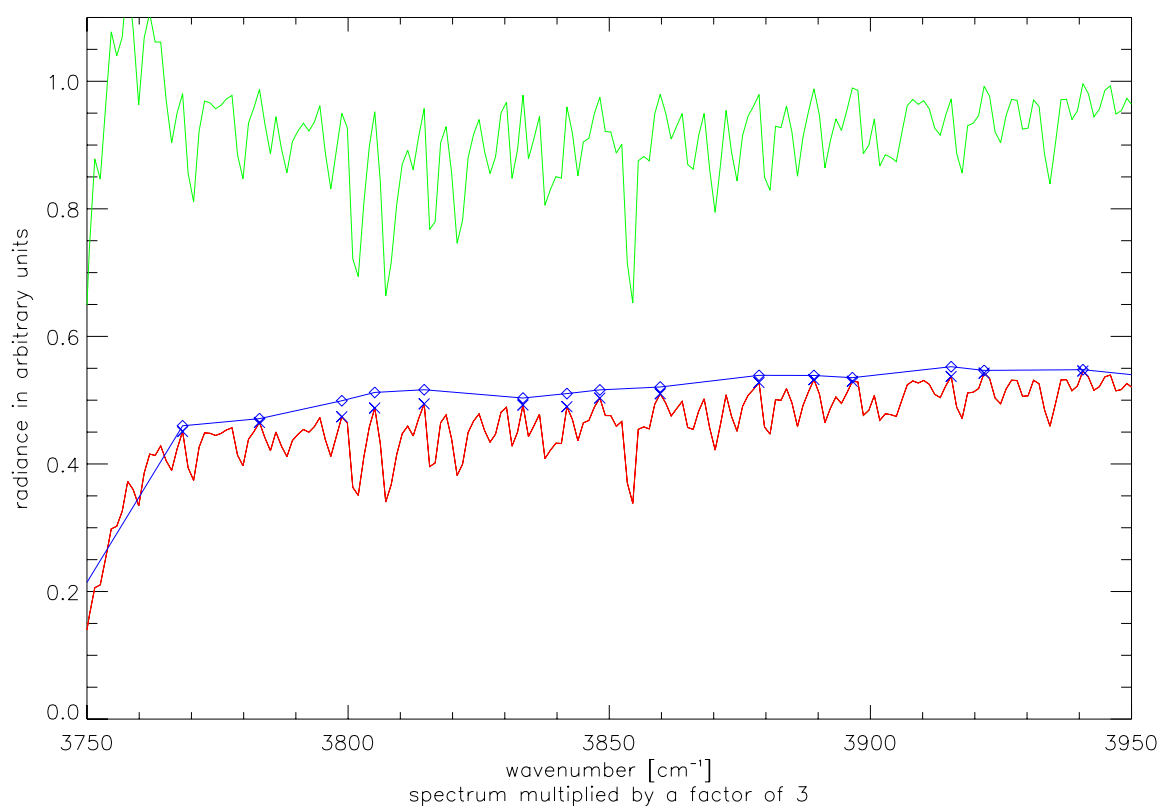


Figure 5.5: The normalized PFS spectrum (green curve), displayed between  $3850\text{ cm}^{-1}$  and  $3950\text{ cm}^{-1}$ , is created from the average of the absolute PFS spectra 134–148 of orbit 1549 (red curve) by its division through the piecewise defined continuum (blue line). In the first iteration the continuum definition points are selected (blue crosses) and in the second iteration corrected for  $\text{H}_2\text{O}$  continuum absorption (blue diamonds). If the shown absolute PFS spectrum is divided by a factor of 3 the radiance unit [ $\text{erg/s/cm}^2/\text{sr/cm}^{-1}$ ] is valid for the y-axis yielding a signal-to-noise ratio of about 30.

## 5.5 Data fitting and continuum correction

In the performed least-square-fit the fitting criterion is the standard deviation of the absolute difference of the normalized measured and synthetic spectra. It is applied in the range between  $3820\text{ cm}^{-1}$  and  $3900\text{ cm}^{-1}$  because there the water vapour lines are most pronounced and the influence of the solar spectrum is not too strong.

Now the computation of the synthetic spectrum and its normalization are iterated in a loop using the steepest descent method to find the best fit (with Fibonacci minimization). As the gradient the difference of the fitting criteria of the corner points of the respective interval is used. The iteration stops when the optimum fit of the two spectra provides

the H<sub>2</sub>O mixing ratio with an accuracy of 1 ppm. The quality of fit is then equal to the resulting fitting criterion.

Initially the continuum used to normalize the measured spectrum is drawn through the local maxima of spectral points without considering water absorption (first iteration). However, absorption in continuum channels is typically of about a few percent. This absorption is taken into account by using the best fit synthetic spectrum from the first iteration and adjusting the continuum with a slight increase of its level which leads to effectively deeper spectral details. This new continuum  $C_{new}(\nu)$  is calculated by the linear interpolation between corrected local maxima points  $\nu_M$ . The radiance in those points is given by

$$C_{new}(\nu_M) = I_{PFS}(\nu_M) / N_{synth}^{opt}(\nu_M)$$

where  $I_{PFS}(\nu_M)$  is the radiance of the absolute (averaged) PFS spectrum and  $N_{synth}^{opt}(\nu_M)$  the radiance of the normalized synthetic spectrum with the optimum H<sub>2</sub>O mixing ratio fit. Now the new corrected continuum is used to normalize the PFS spectrum again and repeat the water vapour retrieval loop a second time.

An example of the corrected continuum is shown in figure 5.5 as the blue piecewise defined line. The blue crosses on the raw spectrum (red line) mark the definition points for the continuum in the first loop while the blue diamonds denote the adjusted continuum points for the second loop. Clearly in the region between 3790 cm<sup>-1</sup> and 3890 cm<sup>-1</sup> the continuum had to be shifted upwards for the purpose of getting an appropriate normalized spectrum (upper green line) which follows the expected band depth of a few percent.

## 5.6 Examples of spectral fits

After the fitting loop is performed with the corrected continuum the final result is the mixing ratio below saturation that provides the best fit. The computation of the resulting column density must include the temperature and pressure profiles. It is described in detail in appendix A.4.

A typical example of a fit result with the described procedure is presented in figure 5.6. There the normalized average of the uncalibrated observational spectra 61–75 of orbit 278 between 3750 cm<sup>-1</sup> and 4000 cm<sup>-1</sup> (green line) is fitted by the synthetic spectrum (black line). The atmospheric profiles are calculated for latitude 6.7°N and longitude 15.5°W, during  $L_S=15.7^\circ$  and local solar time (in the plots abbreviated with LST) of 11:03. The LDT was tuned to 287.8 K, as explained in section 5.2. The fit yields a H<sub>2</sub>O mixing ratio of 225 ppm which results in a column density of 19.0 pr.  $\mu\text{m}$  and a saturation level at ~19 km above the local surface (the error estimation for these values will be subject of section 5.8). However, despite the good agreement a few features remain not well fitted, e.g. the broader absorption at around 3810 cm<sup>-1</sup> or the more narrow line at 3852 cm<sup>-1</sup>. The origin of these features lies most likely in unknown instrumental behaviour but might also be a hint to unknown contribution of atmospheric gases.

Some more examples are displayed in the following. A very good fit with a high signal-to-noise ratio (S/N) of ~50 was achieved for the spectra 123–137 of orbit 1415, presented in figure 5.7. The fit result are a mixing ratio of 270 ppm or a column density of 13.9 pr.  $\mu\text{m}$  with a saturation level at 16 km altitude. Representing a mean S/N ratio of about 18 are spectra 258–272 of orbit 1549 where 156 ppm of water were detected that

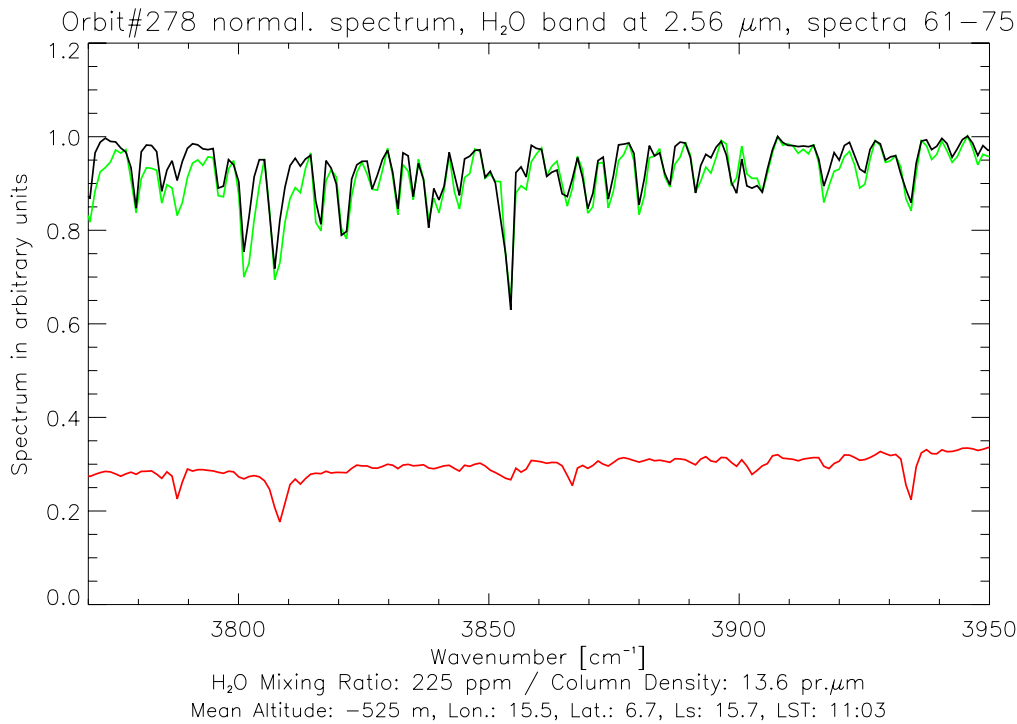


Figure 5.6: Green curve: normalized PFS average spectrum constructed of 15 observational spectra (numbers 61–75) of orbit 278. Black curve: fitted synthetic spectrum for the given conditions. Red curve: arbitrarily shifted solar spectrum (along the y-axis). For the H<sub>2</sub>O fitting the region between 3820  $\text{cm}^{-1}$  and 3900  $\text{cm}^{-1}$  was used yielding a mixing ratio of 225 ppm corresponding to a column density of 19.0 pr.  $\mu\text{m}$  at a saturation level of 19 km above the surface.

are equal to 8.0 pr.  $\mu\text{m}$  and a saturation occurring at 35 km. The fit is shown in figure 5.8. At last, also bad fits due to a low signal or unknown instrumental behaviour shall be displayed. A S/N ratio of only 1.3 is recorded in spectra 93–107 of orbit 1008 (figure 5.9). The resulting mixing ratio of 442 ppm and column density of 19.6 pr.  $\mu\text{m}$  with a saturation level at 9 km are therefore rather doubtful. The same is true for the result of 782 ppm (column density of 52.7 pr.  $\mu\text{m}$  and saturation level at 7.3 km) of spectra 153–167 recorded in orbit 912. This spectrum, displayed in figure 5.10, has a slightly higher S/N of approximately 3 but clearly shows an unexplainable instrumental behaviour of large scattering.

## 5.7 Fitting improvements

Before turning towards the estimation of errors a brief overview of how the above described fit was developed over time shall be given. In the beginning a simple fit was done using an altitude-depending surface temperature and the barometric formula for the surface pressure. The synthetic spectrum was produced from a band model with isolated Lorentz lines where the spectral lines were taken from the HITRAN 2000 database and no solar spectrum was included. An example of the fitting result with these conditions is shown in figure 5.11: the average of 15 calibrated and normalized PFS spectra of orbit 278

## 5 Data analysis

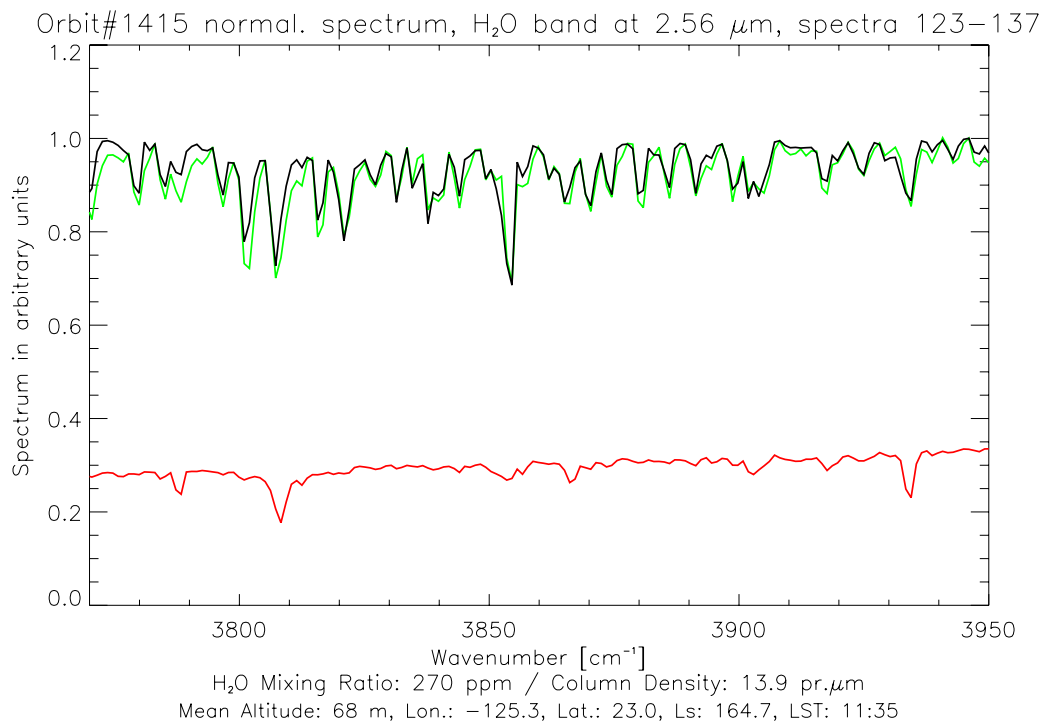


Figure 5.7: The average spectrum 123–137 of orbit 1415 with a high S/N=50 caused by water with 270 ppm or 13.9  $\text{pr}.\mu\text{m}$  (saturation level at 16 km).

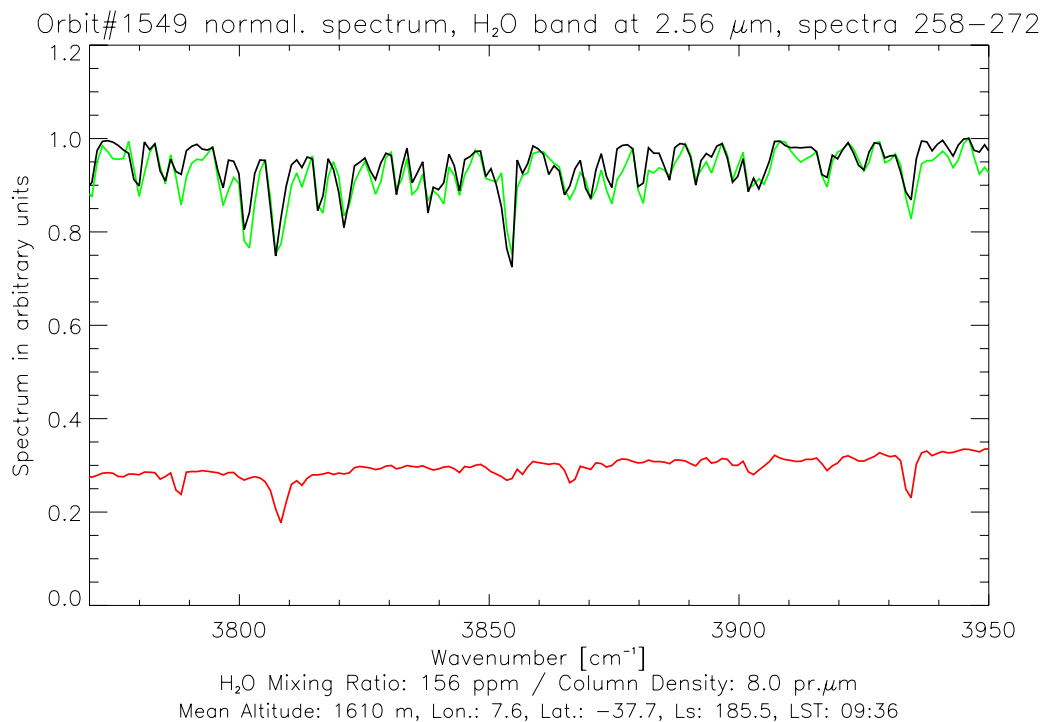


Figure 5.8: The average spectrum 258–272 of orbit 1549 with a mean S/N=18 caused by water with 156 ppm or 8  $\text{pr}.\mu\text{m}$  (saturation level at 35 km).

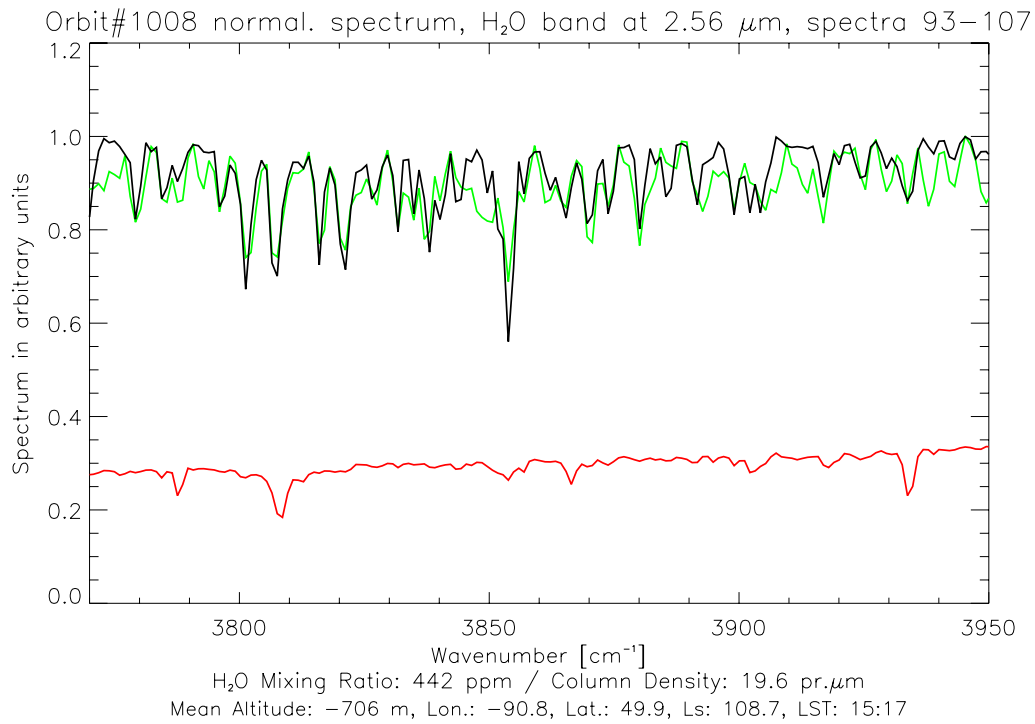


Figure 5.9: The average spectrum 93–107 of orbit 1008 with a low S/N=1.3 caused by water with 442 ppm or 19.6 pr.  $\mu\text{m}$  (saturation level at 9 km).

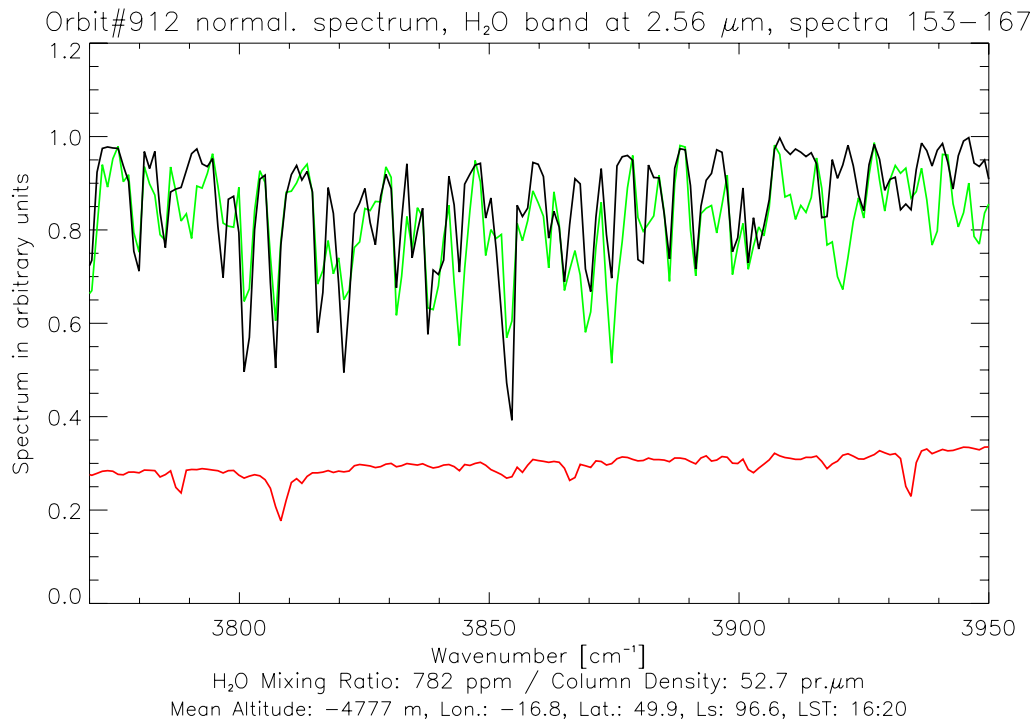


Figure 5.10: The average spectrum 153–167 of orbit 912 with a low S/N=3.1 caused by water with 782 ppm or 52.7 pr.  $\mu\text{m}$  (saturation level at 7.3 km).

between  $3750\text{ cm}^{-1}$  and  $4000\text{ cm}^{-1}$  (green line) is fitted by a band model spectrum (black line). The retrieved water vapour mixing ratio is  $300.3\text{ ppm}$  corresponding to a column density of  $19.0\text{ pr. }\mu\text{m}$  with uniform vertical mixing. The generally bad fit (compared with figure 5.6) and especially features like the unfitted  $\text{CO}_2$  wing at  $3750\text{ cm}^{-1}$  or the missing solar lines (solar spectrum drawn in red) clearly proved the need for improvements.

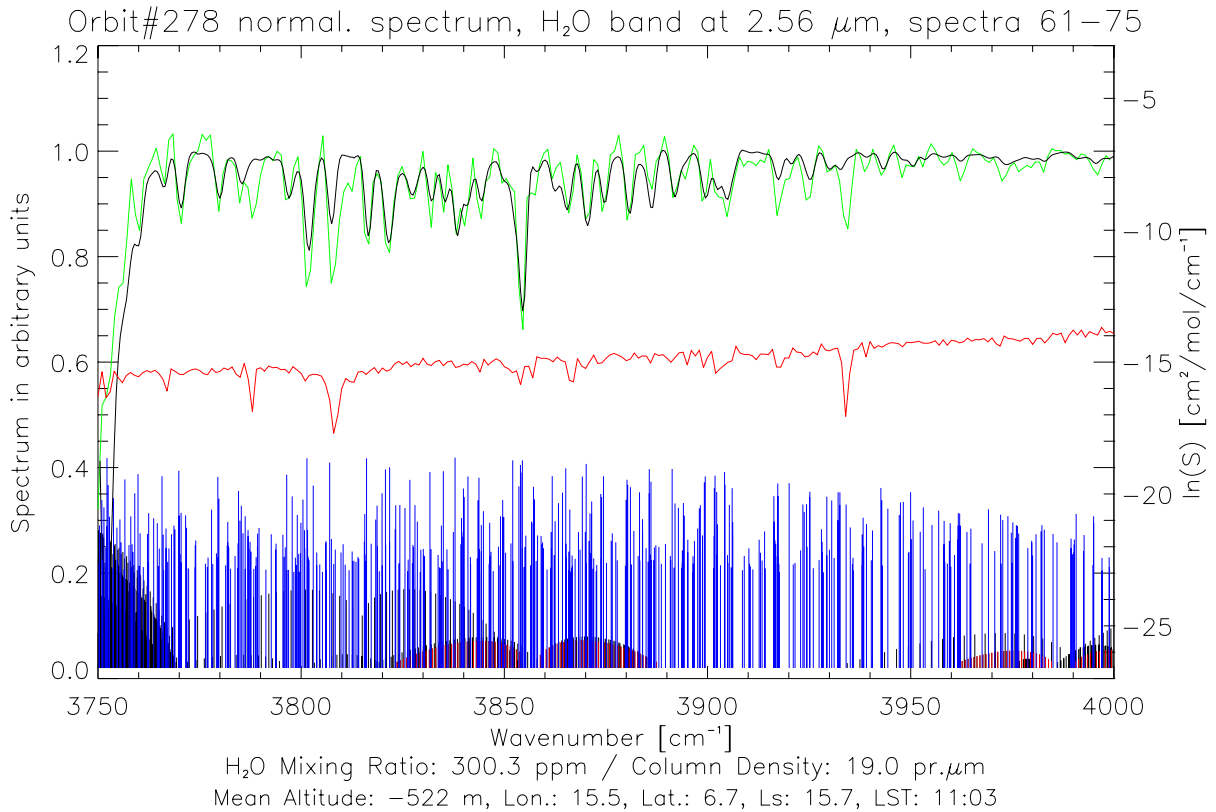


Figure 5.11: The normalized average of calibrated PFS spectra 61–75 of orbit 278 (green line) between  $3750\text{ cm}^{-1}$  and  $4000\text{ cm}^{-1}$  is fitted by the synthetic spectrum (black line). For explanation of some unfitted features, e.g. at  $2935\text{ cm}^{-1}$ , the arbitrarily shifted solar spectrum is drawn in red. At the bottom of the plot the absorption lines of water (blue) and two carbon dioxide isotopes ( $^{16}\text{O}^{12}\text{C}^{16}\text{O}$  in black,  $^{16}\text{O}^{12}\text{C}^{18}\text{O}$  in red) are depicted. For the given conditions the fit yields a H<sub>2</sub>O column density of  $19.0\text{ pr. }\mu\text{m}$

To achieve a better fit with narrower spectral line features a line-by-line calculation was found to be superior as its spectral resolution is much higher. Additional improvements were made by taking into account the different line broadening parameter between a nitrogen/oxygen atmosphere and a  $\text{CO}_2$  atmosphere and by including the solar spectrum. This made it necessary to have the reflectance as another free parameter, though.

In the end the main focus was the normalization of the PFS spectra meaning the definition of the continuum by which the absolute PFS spectrum is divided (a description of the finally used method was given in chapter 5.4). In the first tests a two- or three-dimensional polynomial fit was applied to the selected continuum points. This method has the advantage of smoothing out possible spikes in the spectrum. On the other hand those kind of features might be real and the exact amount of error cannot be quantified anyway.

A comparison of results using a polynomial function with those applying a piecewise continuum showed that with a second order polynomial the final column density values are by about 0.3–2% lower, based on more than 3000 datapoints. Finally, the averaging of apodized spectra and the choice of a wavelength-independent reflectance have led to the selection of a piecewise defined continuum in order to account for unknown spectral features due to mineralogy or instrumental effects.

## 5.8 Discussion of uncertainties

### 5.8.1 Uncertainties from numerical models

An important issue of PFS/SW data reduction is the estimation of errors and uncertainties. A comparison of different databases for spectral lines, namely HITRAN 2000, GEISA and HITRAN 2004 has shown minimal discrepancies for common pressure, temperature and airmass. In figure 5.12 these three different transmittances are presented between  $3845\text{ cm}^{-1}$  and  $3860\text{ cm}^{-1}$ . Regarding the calculation of transmittances the largest error

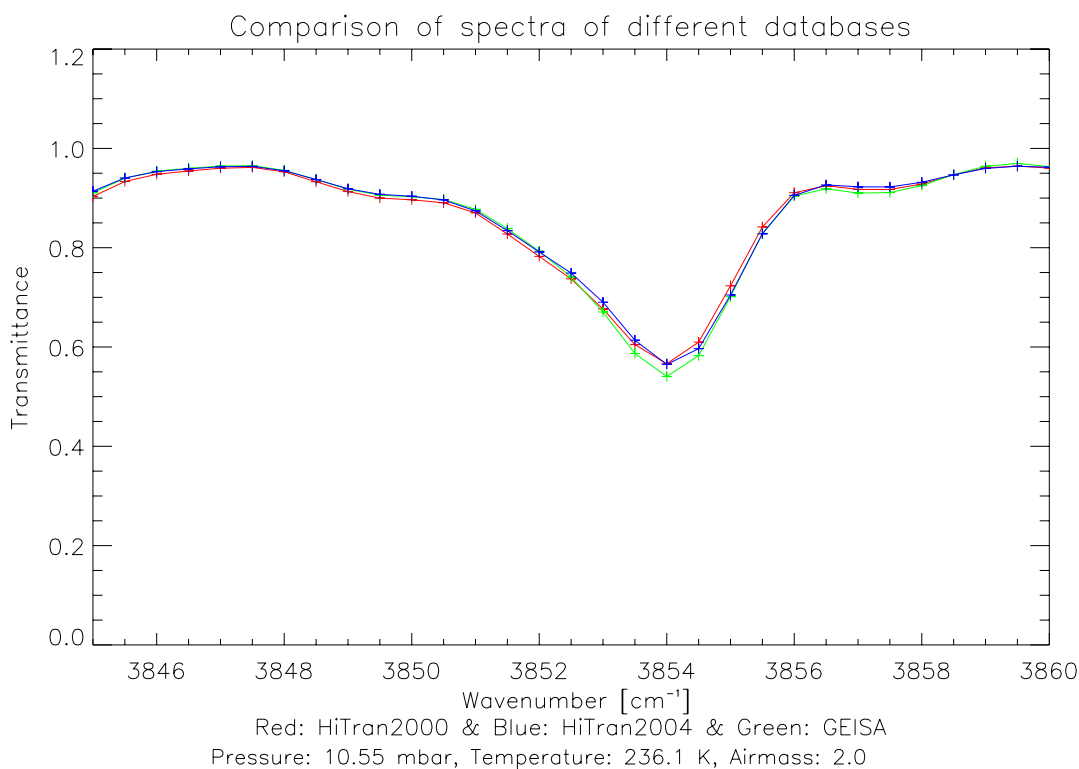


Figure 5.12: A comparison of the transmittances using three different spectroscopic databases for around  $3854\text{ cm}^{-1}$ : for a mixing ratio of 300 ppm at a pressure of 10.55 mbar and a temperature of 236.1 K the difference between HITRAN 2000 (red), HITRAN 2004 (blue) and GEISA (green) is minimal.

source is certainly the factor for the line broadening of spectral lines in  $\text{CO}_2$  atmospheres compared to Earth's atmosphere for which the HITRAN database is created. Although it is an important spectroscopic parameter there is little information or even agreement on its

exact value in the considered wavenumber range. For our calculations a value of 1.5 was considered reasonable. In case this value should prove incorrect the water column density is supposed to decrease linearly in first order with an increasing broadening factor, i.e. a change from 1.5 to 1.4 would yield column densities which are by 10% higher than the current ones.

Also the effects of potential intrinsic errors of the used climate model were investigated. The pressure uncertainty of EMCD is estimated to be 10–20 Pa (private communication, Forget 2006). As a consequence the column density results are less than 2% lower for a pressure shift of +10 Pa because increasing pressure means a larger total number of absorbing H<sub>2</sub>O molecules. The temperature accuracy is more difficult to estimate but it plays a minor role for the line shape in the SW channel, anyway. Yet for the determination of the saturation level it is essential. For this purpose the temperature profile was shifted by  $\pm 3$  K, and as a result the column density has changed by approximately 5%, decreasing with increasing saturation altitude. Here it shall be mentioned that the error in the formula for the determination of the saturation pressure (equation 5.8) is lower than the one due to the temperature uncertainty. For future investigations it is certainly desirable to include the PFS/LW temperature inversion tools to retrieve the correct temperature profiles, e.g. as provided by Grassi et al. (2005) or Ignatiev et al. (2005). Also the pressure could in principle be determined from the 2.0  $\mu\text{m}$  CO<sub>2</sub> band but this is not usable due to spacecraft vibrations, as was shown in figure 4.3 (page 49).

Apart from the intrinsic model uncertainties there is another cause contributing to pressure and temperature errors, namely the provided geometry information (Maturilli et al. 2002). Depending on its accuracy the surface altitude might vary and therefore the calculated pressure. However, since there are always several spectra averaged this error is considered not important because also the surface altitude is a mean value. It certainly poses a problem for abruptly changing landforms like the giant volcanoes and the Vallis Marineris because these topographic features are covered by only a few spectra and have dramatic altitude differences. Moreover, also the EMCD has only a limited spatial resolution and is unreliable in these areas. So in these cases the retrieved water amounts are only considered as a rough estimation<sup>6</sup>.

Finally, in more elaborate theoretical models also the influence of dust should be included because the increased pathlength of light scattered by aerosols would lead to an overestimation of water amounts if it's not considered in the retrieval. On the other hand dust can obscure the real surface (in the SW regime) and thus cause an underestimation of the real column density. Yet in this work the effects of dust were neglected because a low opacity was assumed and also the dust extinction in the 2.6  $\mu\text{m}$  band is smaller than at shorter wavelengths. In those cases both Fedorova et al. (2004) and Sprague et al. (2006) concluded that the airmass must be in the order of 4 to 6 to cause a significant effect. Also Fedorova et al. (2006) have shown with spot-pointing observations of SPICAM that retrievals for airmasses below 3.5 deliver consistent results. In this work the maximum considered airmass was 3.7. In conclusion, the contribution of uncertainties induced by the theoretical input (apart from the broadening factor) is small with respect to the other errors as explained in the following.

---

<sup>6</sup>Spectrometers with higher spatial resolution like OMEGA on *MEX* or CRISM on the *Mars Reconnaissance Orbiter* are more suitable for this task.

### 5.8.2 Instrumental errors

Apart from the theoretical uncertainties the ones due to instrument behaviour and the retrieval method are far more dominating. As shown in figure 4.5 (page 50) the PFS noise equivalent radiance in the  $2.6\ \mu\text{m}$  band is around  $0.02\ \text{erg/s/cm}^2/\text{sr/cm}^{-1}$ . Depending on the observation conditions the measured spectral radiance of a single spectrum from Mars is on average around  $0.0926\ \text{erg/s/cm}^2/\text{sr/cm}^{-1}$  with a standard deviation of  $0.0476\ \text{erg/s/cm}^2/\text{sr/cm}^{-1}$ . Since there are generally 15 individual spectra averaged the signal-to-noise ratio is improved by a factor of  $\sim 4$ . Thus a mean statistical error of 5.6% has to be assumed for a single datapoint. Considering the distribution of the S/N ratios the statistical error ranges between about 4% and up to 20% (at half maximum of the distribution). Figure 5.13 presents the relation between the S/N ratio of all datapoints with the quality of the corresponding spectral fit (in arbitrary units). This quality of the fit was defined in section 5.5, and low values correspond to a good fit quality. Clearly there is a strong correlation between these quantities, i.e. a high S/N ratio leads to a better fit. In

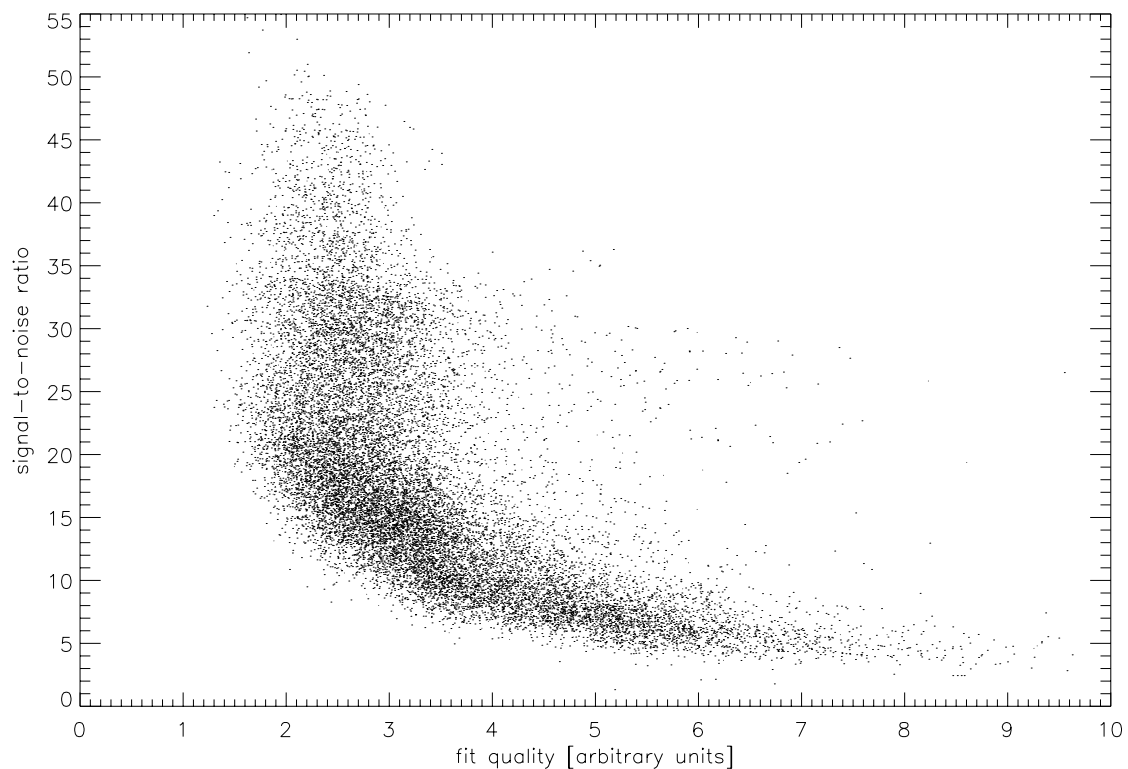


Figure 5.13: The signal-to-noise ratio of all datapoints as a function of the quality of the spectral fit (in arbitrary units).

addition another error source had to be introduced because the SW channel operations are controlled by the LW laser diode for orbits later than 634, as described in chapter 5.2. The shift of the PFS spectra compared to the wavenumber grid of the synthetic spectrum requires the adjustment of the laser diode temperature. With the reasonable assumption of an achieved LDT fitting accuracy of 0.25 K the result of the water amount has an uncertainty of maximum 1.5%.

Furthermore, at this point it has to be stressed that due to the lack of calibration of the SW channel and the presence of microvibrations on *MEX* there could still be systematic problems that are impossible to quantify (cf. chapter 4.3). Out of this reason residual unexplained spectral features are compensated by using a piecewise function for the PFS spectrum normalization.

### 5.8.3 Uncertainties of the retrieval method

In the course of the method evaluation it was identified that the sources of systematic errors with the strongest impact are the definition of the continuum both for the PFS spectra and for the synthetic spectra. For the creation of the synthetic spectrum the infrared reflectance has to be deduced. It is a single wavelength-independent value determined from the comparison of the mean radiance between  $3860\text{ cm}^{-1}$  and  $3960\text{ cm}^{-1}$  of the measured and the synthetic spectrum. Testing small changes of this range showed only a marginal effect of 0.1% on the retrieved reflectance and of 0.4% on the resulting water vapour amount.

For the purpose of the normalization of the synthetic spectrum a linear function between two points of the corrected solar spectrum is considered as the continuum. These points are located at around  $3774\text{ cm}^{-1}$  and  $3908\text{ cm}^{-1}$  as they are least affected by atmospheric absorption (see figure 5.4). Yet the final result of water vapour can vary by around 6% depending on the location of the points defining the linear function, for example by changing the second point from  $3908\text{ cm}^{-1}$  to  $3876\text{ cm}^{-1}$ .

The normalization of the PFS/SW spectrum has proved to be most problematic. As explained in the description of the retrieval method a piecewise defined continuum and its correction for  $\text{H}_2\text{O}$  absorption was selected. Extensive testing with various forms of continua and variations of applied criteria showed strong differences in the results. So obviously the exact level and form of the continuum governs the retrieved water vapour amount most strongly. Particularly, the choice of which spectral grid-points should be adjusted (cf. chapter 5.5) proved to be difficult. To determine the necessity of adjustment the term *sigmalevel* is introduced. It is defined as the factor by which the difference between the normalized PFS spectrum and the normalized synthetic spectrum differs from the noise level of the continuum ("*sigma*"). For example a *sigmalevel* of 0.5 means that only these points of the continuum get adjusted where the difference between the measured and the synthetic spectrum is larger than 0.5 *sigma*. For comparison the mean difference between synthetic and measured spectra for several PFS spectra of different signal-to-noise ratios is shown in figure 5.14. Clearly there is only a weak dependence on the selected *sigmalevel* with a weak minimum around *sigmalevel* 0.5 – at least for high S/N. After rigorous testing the solution was to simply adjust every point that defines the continuum (*sigmalevel* 0.0) despite the fact that a more strict adjustment criterion provides better spectral fits. For example a change from *sigmalevel* 0.0 to *sigmalevel* 0.5 yields 12% lower column density results with about 4.4% better fits. These numbers are based on ~15% of the dataset with various S/N ratios. Figure 5.15 presents the results of mixing ratio corresponding to figure 5.14. Obviously, with a more strict continuum adjustment criterion (lower *sigmalevels*) the results increase. This increase is the stronger for lower S/N ratios.

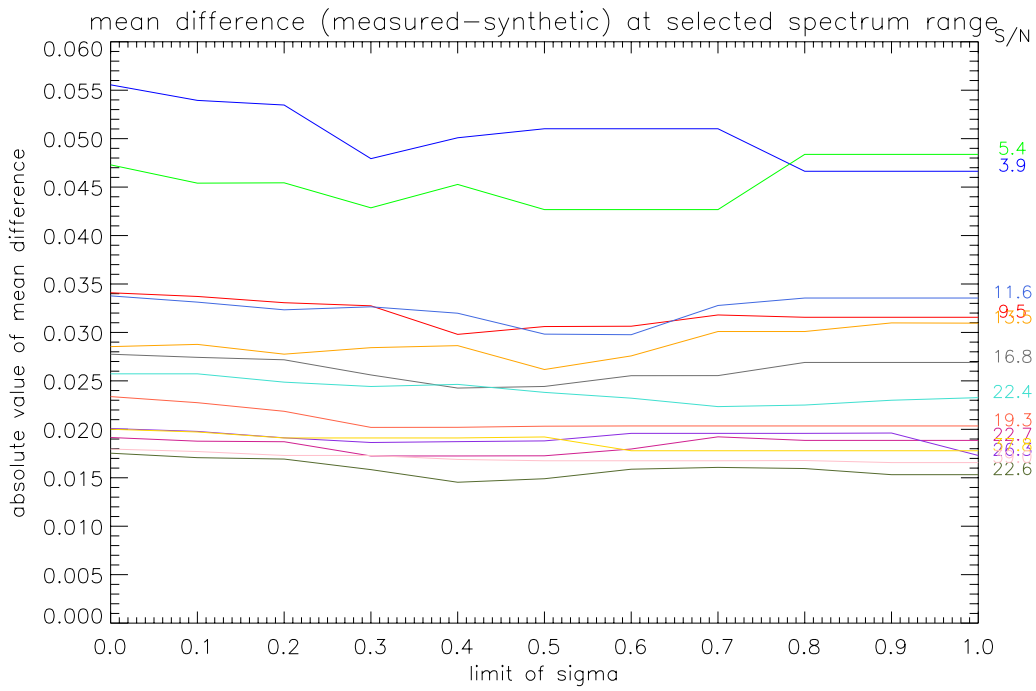


Figure 5.14: The mean difference between synthetic and measured spectra plotted versus sigmalevels 0.0 to 1.0 for several PFS spectra of different signal-to-noise ratios (3.9–39.0).

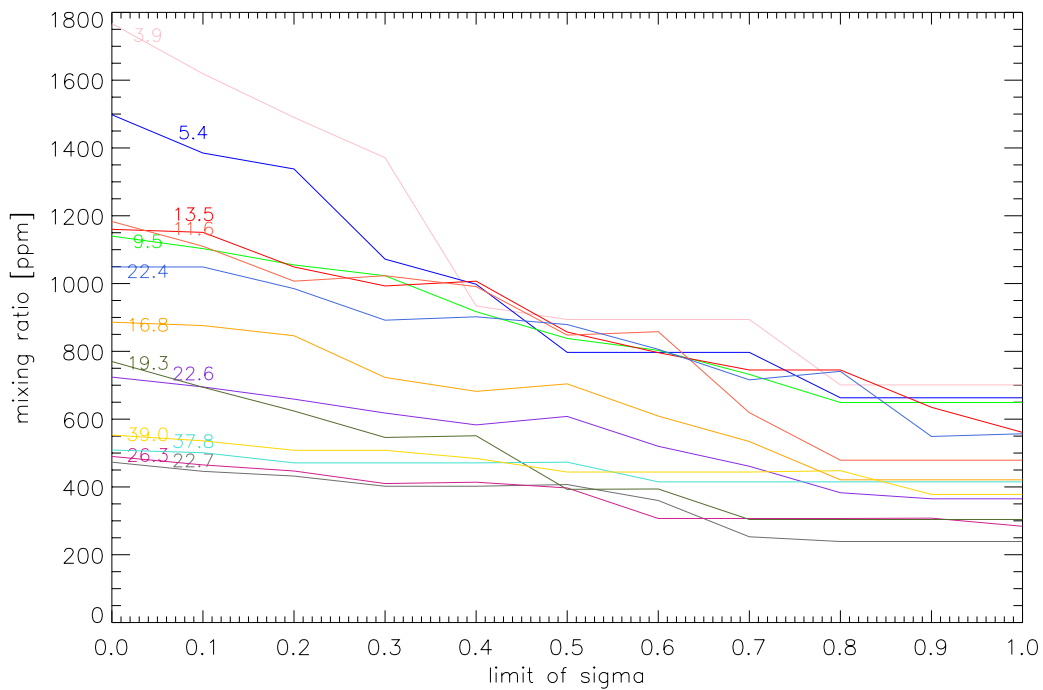


Figure 5.15: The resulting mixing ratios for several PFS spectra of different signal-to-noise ratios plotted versus sigmalevels 0.0 to 1.0.

An example of the resulting spectra is given for the average of the PFS/SW observations 119 to 133 of orbit 1023. Here the LDT was tuned to 286.4 K and the S/N ratio is 22.7. Now a sigmalevel of 0.0 yields a mixing ratio of 473 ppm (the standard deviation of the absolute difference of the spectra is 0.0304), shown in figure 5.16, while a sigmalevel of 0.5 gives 407 ppm (with a standard deviation of the absolute difference of the spectra of 0.0260), shown in figure 5.17. Although in both cases the spectral fit looks satisfactory the resulting water amounts differ quite strongly.

At last, also the fitting loop itself caused some error, namely when the correct mixing ratio lies near the edge of the mixing ratio interval containing the best fit. In this case an uncertainty of 10 ppm is assumed which results at a maximum uncertainty of 6%.

As a conclusion it was shown that even subtle changes in the form or level of the continuum can cause quite different results for the retrieved water vapour amount. This makes the definition of the continuum the major error source apart from the uncertainty due to the CO<sub>2</sub> line broadening factor. Considering all contributions the total error for each data point is therefore conservatively estimated to be in the order of 20–30% depending on the S/N ratio. Please note that all these systematical errors would result in an offset from the results presented in the next chapter. This means that the relative temporal and spatial changes of water vapour are still true.

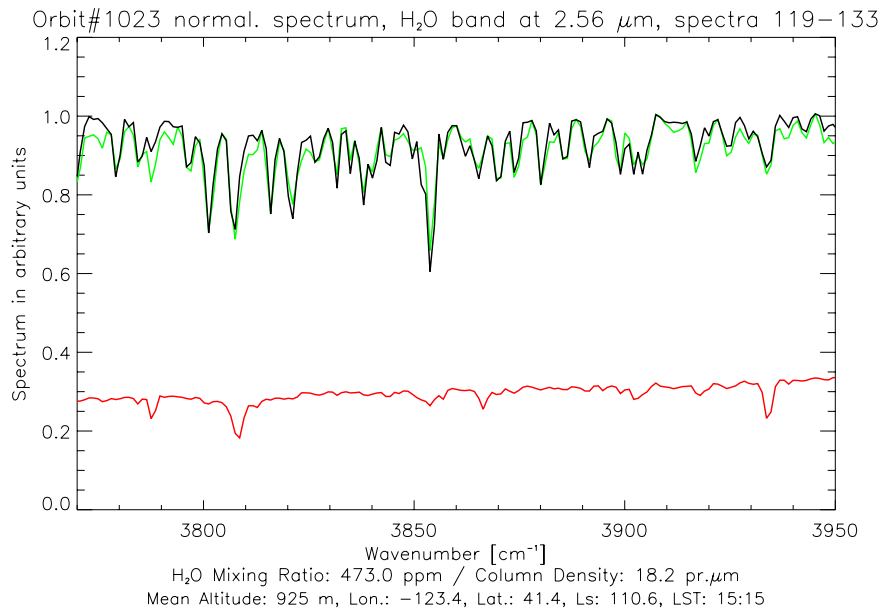


Figure 5.16: Green curve: normalized PFS spectrum, average of spectra spectra 119–133 of orbit 1023. Black curve: fitted synthetic spectrum for the given conditions. Red curve: arbitrarily shifted solar spectrum. The applied sigmalevel of 0.0 results in a mixing ratio of 473 ppm corresponding to a column density of 18.3 pr.  $\mu\text{m}$  at a saturation level of  $\sim 9$  km.

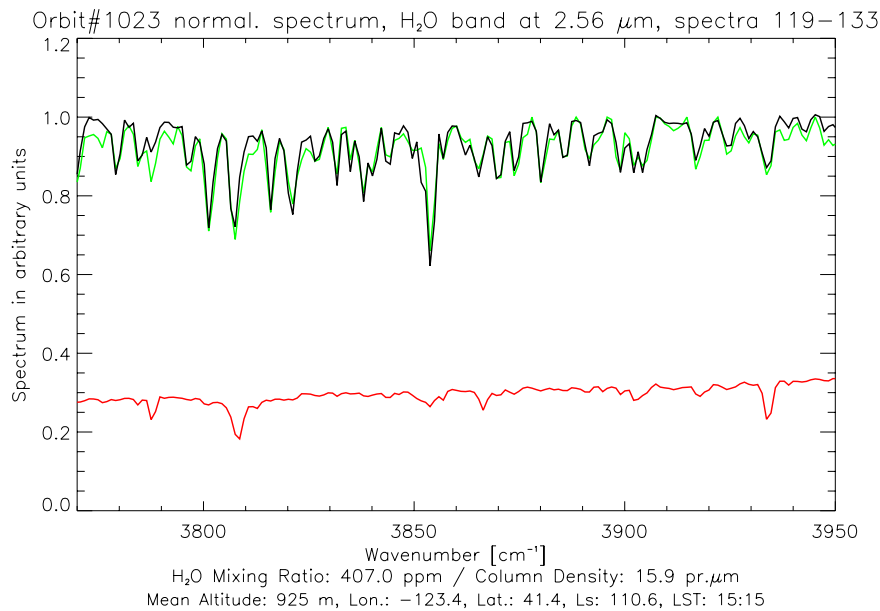


Figure 5.17: Green curve: normalized PFS spectrum, average of spectra spectra 119–133 of orbit 1023. Black curve: fitted synthetic spectrum for the given conditions. Red curve: arbitrarily shifted solar spectrum. The applied sigmalevel of 0.5 results in a mixing ratio of 407 ppm corresponding to a column density of 15.9 pr.  $\mu\text{m}$  at a saturation level of  $\sim 9$  km.



## 6 Results and discussion

In the previous chapter it was seen how individual results of the spectral fitting look like (see figures 5.6 to 5.10). Now after processing the entire available dataset all those results were used for global analysis that fulfill the following criteria: the individual fit quality of a spectrum (defined in chapter 5.5) has to be better than the mean plus five times the standard deviation of all fit qualities, and the S/N ratio must be higher than one.

### 6.1 Seasonal cycle

The main goal of this work was to study the seasonal behaviour of water vapour on Mars. This was achieved for the time between the end of MY 26 at  $L_S=331^\circ$  until the middle of MY 27 at  $L_S=196^\circ$ . The seasonal map of atmospheric water is presented in figure 6.1 where the retrieved water column densities are binned by  $2^\circ$  in solar longitude ( $L_S$ ) and  $2^\circ$  in geographic latitude. Such a bin contains on average 13 individual datapoints (maximum 88). Although the maximum binned column density is around 68 pr.  $\mu\text{m}$  the colour scaling goes only up to 60 pr.  $\mu\text{m}$  to emphasize minor variations in the seasonal behaviour.

The average column density for the entire dataset is 16.2 pr.  $\mu\text{m}$  and in general the familiar evolution of the water cycle is followed – despite the gaps in coverage. For the time earlier than a solar longitude of  $70^\circ$  there is a mean  $\text{H}_2\text{O}$  content of 8.2 pr.  $\mu\text{m}$  detected whose homogeneous latitudinal and seasonal distribution makes this period suitable to look for diurnal variations. Please note that the strong increase during  $L_S=347\text{--}356^\circ$  is due to the noisy spectra of orbits 72, 97, 100, 103 and 148 whose fits resulted in higher values. Although there is only a sparse coverage around  $L_S=70\text{--}75^\circ$  it is clear that at this time the increase of atmospheric water content begins. The  $\text{H}_2\text{O}$  enhancement takes place at latitudes between  $70^\circ\text{N}$  and  $80^\circ\text{N}$  with mean values around 24 pr.  $\mu\text{m}$ . This latitude range is also the region where the maximum values are reached later in high summer. Now after  $L_S=90^\circ$  the northern summer is well covered. Until about  $L_S=130^\circ$  the latitudinal distribution is characterized by a large gradient, spanning from column densities of 45–65 pr.  $\mu\text{m}$  north of  $65^\circ\text{N}$ , via 30–45 pr.  $\mu\text{m}$  between  $55^\circ\text{N}$  and  $65^\circ\text{N}$  and 20–30 pr.  $\mu\text{m}$  between  $40^\circ\text{N}$  and  $55^\circ\text{N}$  to values of 10–20 pr.  $\mu\text{m}$  between  $0^\circ\text{N}$  and  $40^\circ\text{N}$  and lower than 10 pr.  $\mu\text{m}$  south of the equator. During  $L_S=130\text{--}140^\circ$  the northern summer maximum drops rapidly to low amounts. This time span corresponds to about 3 weeks on Earth. At the same time the tongue-like peak of 15–20 pr.  $\mu\text{m}$  develops with a center around  $45^\circ\text{N}$  that migrates down to the equator arriving at about  $L_S=190^\circ$ . Thus a peak progression of  $0.8^\circ$  latitude per degree solar longitude can be inferred. This development is displayed in figure 6.2 where the maximum column density was set to 34 pr.  $\mu\text{m}$  to present the spike more clearly.

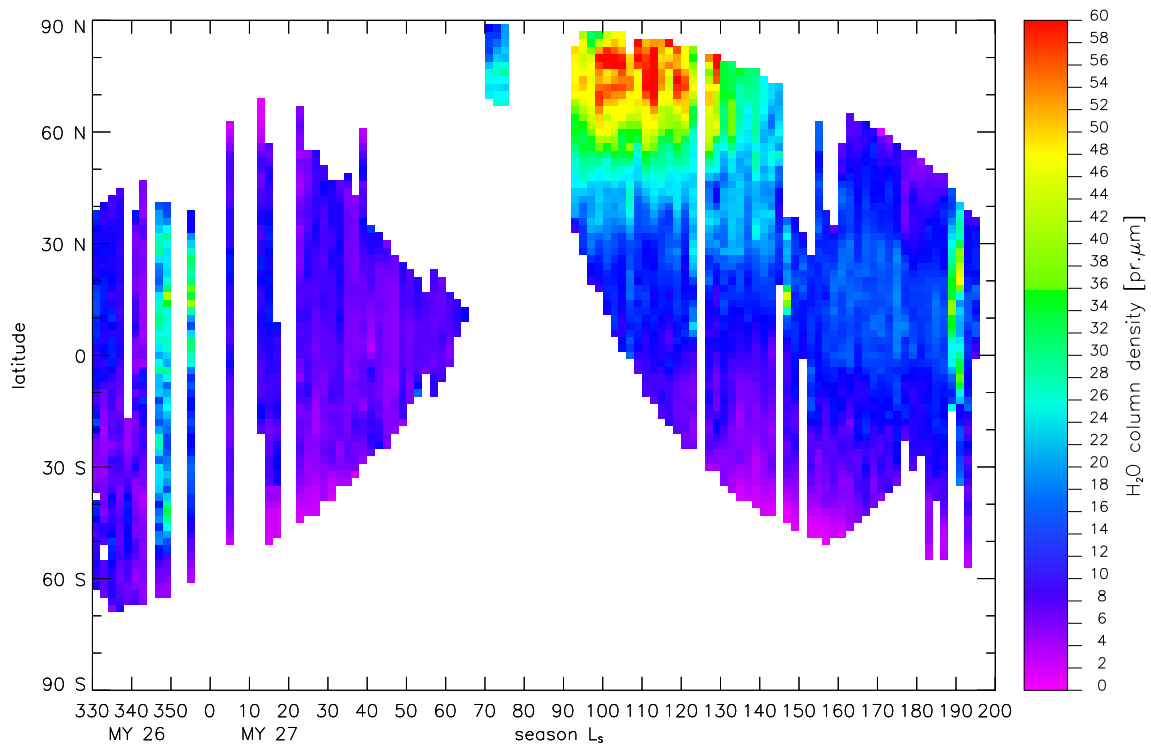


Figure 6.1: The seasonal map of water vapour between  $L_S=330^\circ$  of MY 26 and  $L_S=200^\circ$  of MY 27. Apart from deviations at around  $L_S=350^\circ$  and  $L_S=190^\circ$  due to instrumental behaviour the martian  $H_2O$  cycle is well covered.

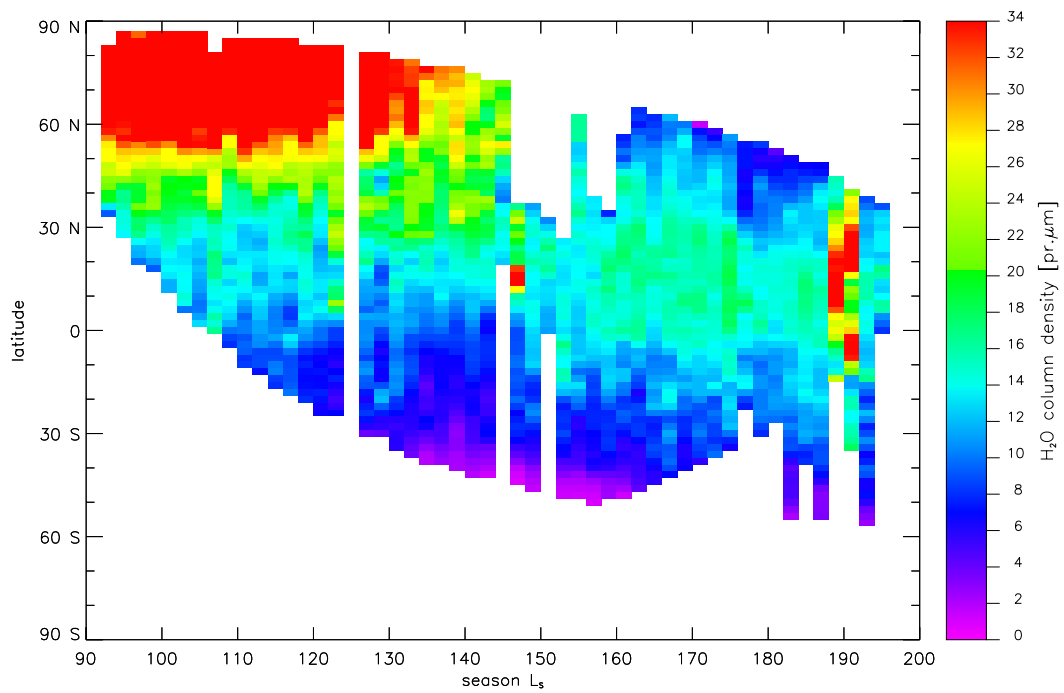


Figure 6.2: The seasonal map of water vapour for  $L_S=90-200^\circ$  with a column density cut-off at  $34 \text{ pr.}\mu\text{m}$  emphasizes the southward moving peak after the northern high summer.

At this point the high column densities between  $10^{\circ}\text{S}$  and  $30^{\circ}\text{N}$  around  $L_S=190^{\circ}$  should be mentioned: they are most likely due to instrumental problems and do not represent a real increase. These high values influence not only the previous seasonal maps but also the following investigation of the progressing water peak.

To study the amount of water, that is transported from the north polar region towards the equator, in a quantitative way the column densities were binned within  $5^{\circ}$  of solar longitude and averaged in the three latitudinal bands of  $0\text{--}30^{\circ}\text{N}$ ,  $30\text{--}60^{\circ}\text{N}$  and  $60\text{--}90^{\circ}\text{N}$ . After that these mean column densities were multiplied with the respective surface area of the bands in order to estimate the total amount of atmospheric water contained in these latitudes. The resulting mass quantities are given in units of  $10^{14}$  g of water and are displayed as a function of season in figure 6.3.

During the height of the northern summer the mass of water mixed in the polar atmosphere is about  $5 \cdot 10^{14}$  g in total (upper panel). In the latitudes between  $30^{\circ}\text{N}$  and  $60^{\circ}\text{N}$  (middle panel) they can even go up to  $7 \cdot 10^{14}$  g. Although there the  $\text{H}_2\text{O}$  column densities have lower values than further poleward (cf. figure 6.2) this fact is more than compensated by the larger surface area. During  $L_S=130\text{--}145^{\circ}$  the northern values drop rapidly to  $\sim 2 \cdot 10^{14}$  g while at the same time in the band of middle latitudes the total mass is still  $\sim 5 \cdot 10^{14}$  g. This marks the beginning of the southward progressing peak. Interesting is now a look at the lower panel. At  $0\text{--}30^{\circ}\text{N}$  the total mass experiences only a weak rise from  $\sim 4.5 \cdot 10^{14}$  g to approximately  $5.5 \cdot 10^{14}$  g between  $L_S=110\text{--}130^{\circ}$  and  $L_S=155\text{--}180^{\circ}$ . During the same time the amounts in the middle latitudes drop by about  $2.5 \cdot 10^{14}$  g.

All in all, the strong decrease of total mass in the polar region between summer and vernal equinox ( $\sim 4 \cdot 10^{14}$  g) is not balanced by an equal increase in the middle latitudes and tropics later in the season. In these lower latitudes the atmospheric water content rises only by about  $1 \cdot 10^{14}$  g. Therefore, one can tentatively conclude that only a low percentage of water vapour is transported southward via the atmospheric circulation while the majority of the water ( $\sim 3 \cdot 10^{14}$  g) has to be stored on the surface, either adsorbed by the regolith or deposited as ice of the seasonal polar cap.

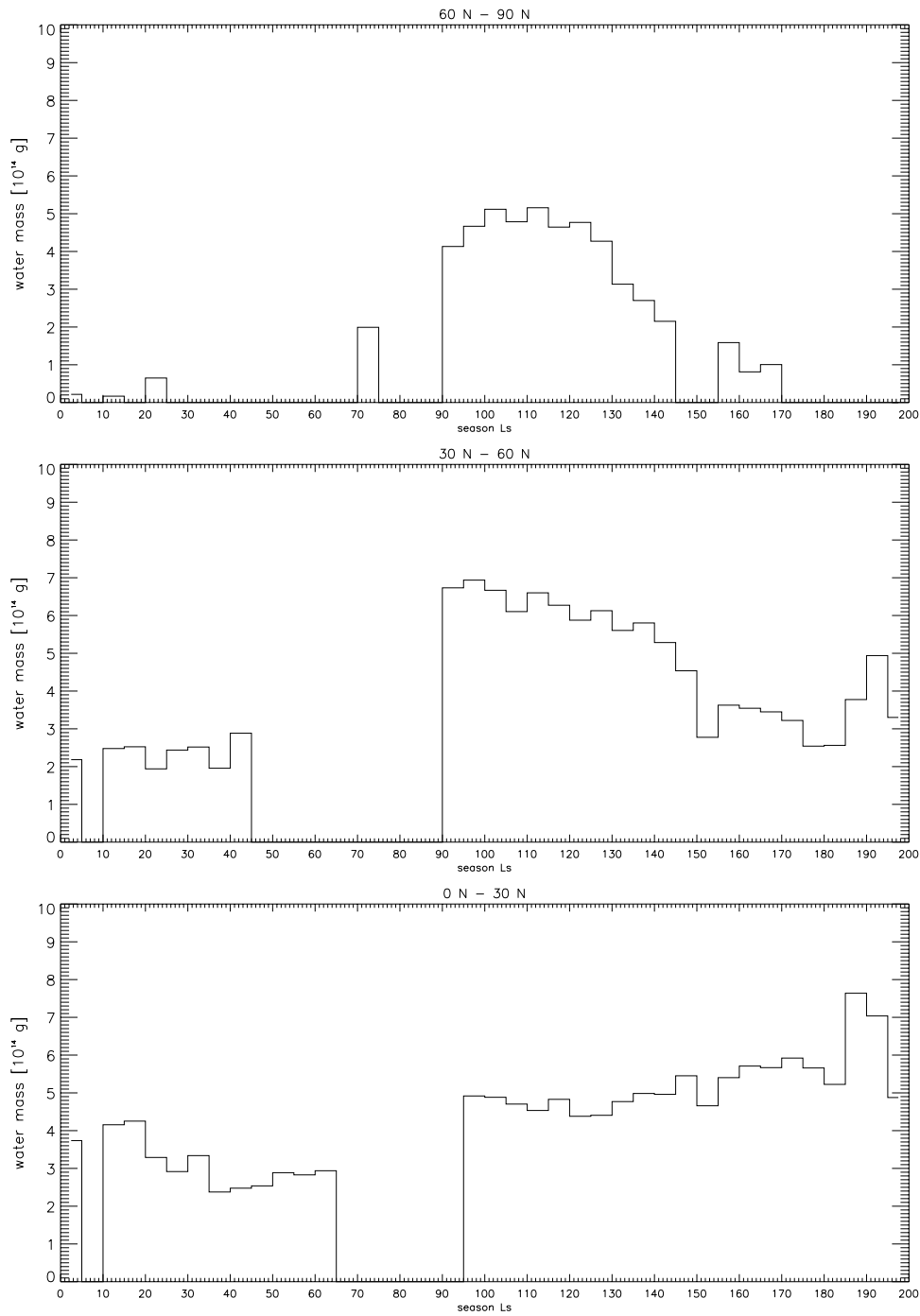


Figure 6.3: For the three latitude bands of 60–90°N (upper panel), 30–60°N (middle panel) and 0–30°N (lower panel) the retrieved column densities were binned within 5° of  $L_S$  and multiplied with the respective area to get the total amount of water contained in the atmosphere of that latitude (given in  $10^{14}$  g). Lack of data coverage causes the gaps before  $L_S = 90^\circ$  and the lower amounts around  $L_S = 150^\circ$ . The high values at  $L_S = 185$ – $195^\circ$  result from instrumental problems. Further explanations are given in the text.

## 6.2 Retrieved reflectance

In chapter 5.4 it was explained that due to the inclusion of the solar spectrum also relative reflectances in the 2.5  $\mu\text{m}$  band are retrieved. However, one has to keep in mind that they are not real measurements but rather show relative differences within orbits. The reason for this can be found in the problems with the absolute calibration and the lower than expected radiance (cf. chapter 4.3). Still the resulting map is presented in figure 6.4 where the relative reflectance for each datapoint is plotted over the map of the visible albedo (in the greyscale a high albedo is marked with light grey and a low albedo with dark grey). Despite some outliers and expected disagreements between individual orbits the match is remarkable, i.e. high relative reflectance corresponds to a high albedo and vice versa. Out of this reason these values could be used for an estimation of a correlation of water amounts with reflectance (or an anti-correlation with thermal inertia). After all, fine-grained material, that has a higher albedo than coarse sand (Christensen et al. 2003), is expected to store larger amounts of  $\text{H}_2\text{O}$  by adsorption than coarse sand because it has a larger surface (cf. chapter 3.3). However, this dataset gives no clear indication for such a correlation because for the latitudes between  $30^\circ\text{S}$  and  $30^\circ\text{N}$  the correlation coefficient is only 0.16.

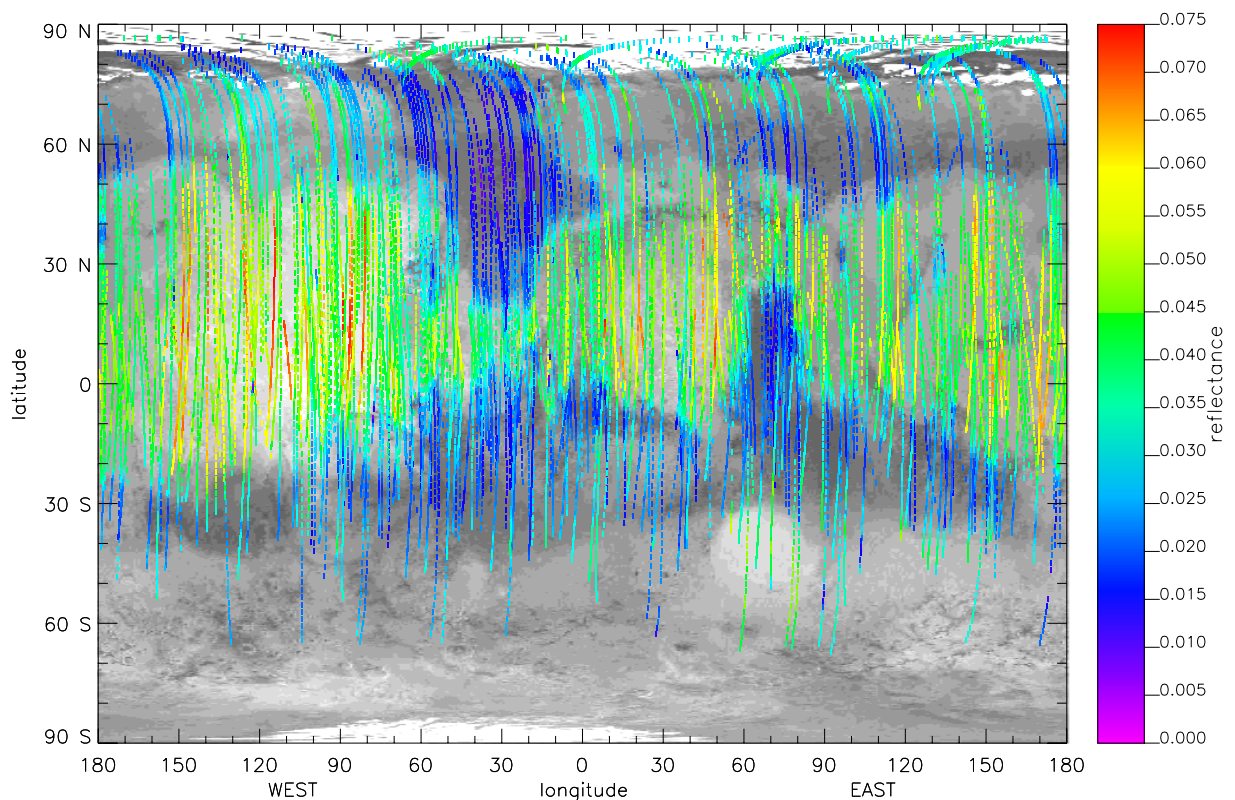


Figure 6.4: The retrieved relative reflectance and the underlying visible albedo map show a remarkably good agreement.

### 6.3 Spatial variations

For the purpose of comparing spatial distributions it is useful to bin the averaged spectra in  $2^\circ$  longitude and  $2^\circ$  latitude within seasons that show little variability. In addition, to rule out topographic effects a scaling to 6.1 mbar is performed, i.e. the retrieved value of each datapoint is multiplied with  $6.1/p_s$ , with  $p_s$  [mbar] the surface pressure for the datapoint. The results, plotted over the albedo map of Mars, are displayed for  $L_S=330-75^\circ$  in figure 6.5 (without the noisy orbits 72, 97, 100, 103 and 148), for  $L_S=90-135^\circ$  in figure 6.7 and for  $L_S=135-200^\circ$  in figure 6.6. In each figure the colour scaling is adapted to the mean  $H_2O$  values. One feature is obvious in the first and third of these figures: over Arabia Terra (about  $0^\circ-80^\circ$  E,  $20^\circ$ S –  $30^\circ$ N) there is an enhancement of a factor of about two compared to the mean column density. Over the Tharsis highlands (between  $70^\circ$ W and  $130^\circ$ W around the equator) another local maximum can be distinguished which is less pronounced, though. Even in the map of northern summer (figure 6.7) there are maxima found in those areas with a statistically meaningful enhancement. The two maxima were also found by Smith (2002, 2004) and for an explanation of these features there are three possibilities: an exchange between adsorbed water in the regolith; stationary planetary waves due to large-scale variations of topography and thermal inertia; a combination of both effects.

First of all, an influence of diurnal variations can basically be excluded because they were not observed in the  $L_S=135-200^\circ$  period, in spite of the good coverage of local times (see section 6.4). Furthermore, the same area was sampled at different local times with progressing orbits. For the increase over Arabia Terra the regolith interaction, that was explained in chapter 3.3, is a reasonable explanation due to the strong correlation with hydrogen in the uppermost soil. Feldman et al. (2004) and Mitrofanov et al. (2004) used the neutron spectrometers onboard *Mars Odyssey* to map the hydrogen content of the soil by measuring the neutron flux from the surface. In the latitude range of  $\pm 45^\circ$  from the equator the detectors found a large concentration of hydrogen in the Arabia Terra region. As these hydrogen atoms are most likely part of water molecules their distribution maps can be regarded as maps of water in the soil. Such a global distribution is presented in figure 6.9 where another minor enhancement is visible in the Medusae Fossae area, southwest of Olympus Mons. However, at this location there is no increased water vapour amount observed. Even more, the Tharsis plateau with its  $H_2O$  maximum is more or less devoid of hydrogen. These arguments in turn support the influence of atmospheric circulation and the presence of stationary waves (explained in chapter 2.4.1) which cause an accumulation of wet air over certain areas (Fedorova et al. (2004) and references therein). The map with all results shown together (apart from the orbits 72, 97, 100, 103 and 148) is displayed in figure 6.8 and strongly implies the existence of a stationary wave with two maxima and minima in the tropical latitudes. Yet Fouchet et al. (2006) performed simulations with the EMCD and showed that models alone cannot explain the large observed amplitudes. Therefore a combination of both water exchange with the soil and circulation effects are the best explanation for the observations (Basilevsky et al. 2006) but also further research and modelling seem to be necessary for a full understanding.

Now in figure 6.7 the northern summer maximum remains to be discussed. Clearly the highest column densities occur between  $60^\circ$ N and  $85^\circ$ N, centered around  $75^\circ$ N. This means that bulk of the atmospheric water is located off the edges of the permanent polar

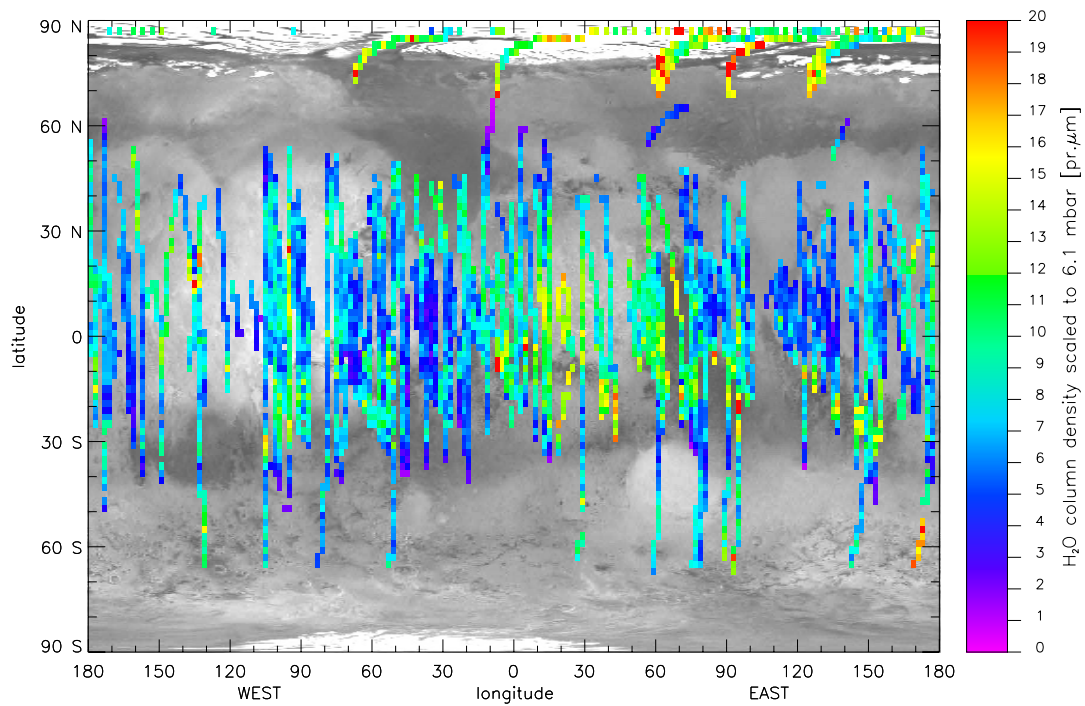


Figure 6.5: The spatial distribution of water vapour around spring equinox for  $L_S=330-75^\circ$ . The column densities, normalized to 6.1 mbar, are displayed up to 20 pr.  $\mu\text{m}$ .

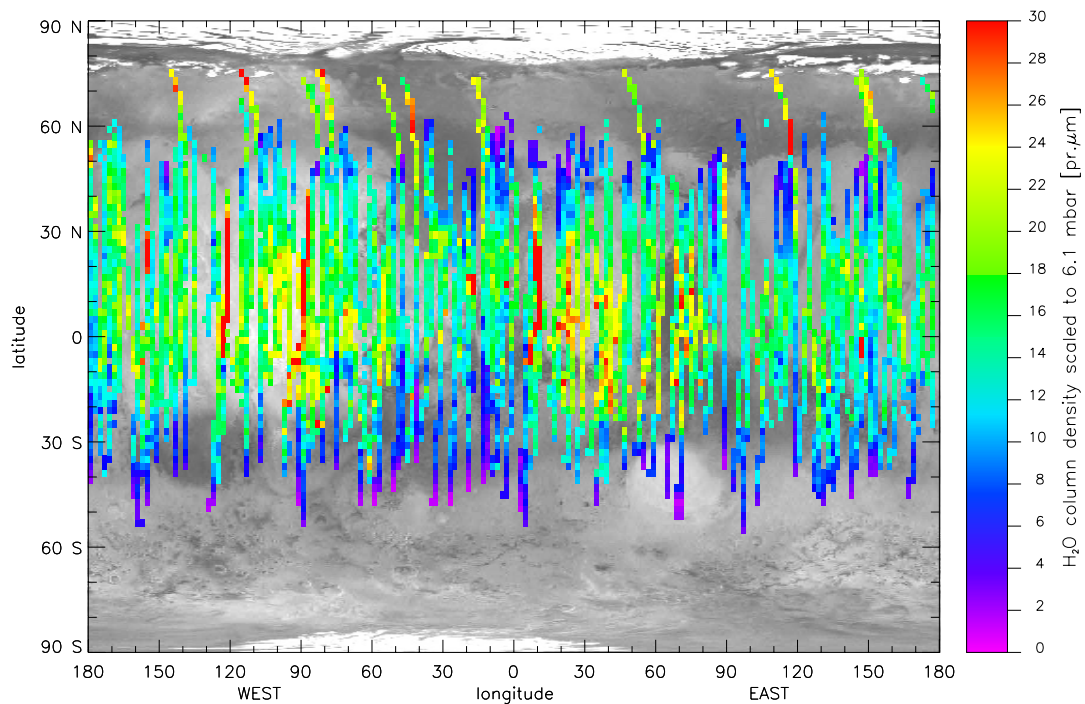


Figure 6.6: The spatial distribution of water vapour around autumn equinox for  $L_S=135-200^\circ$ . The column densities, normalized to 6.1 mbar, are displayed up to 30 pr.  $\mu\text{m}$ .

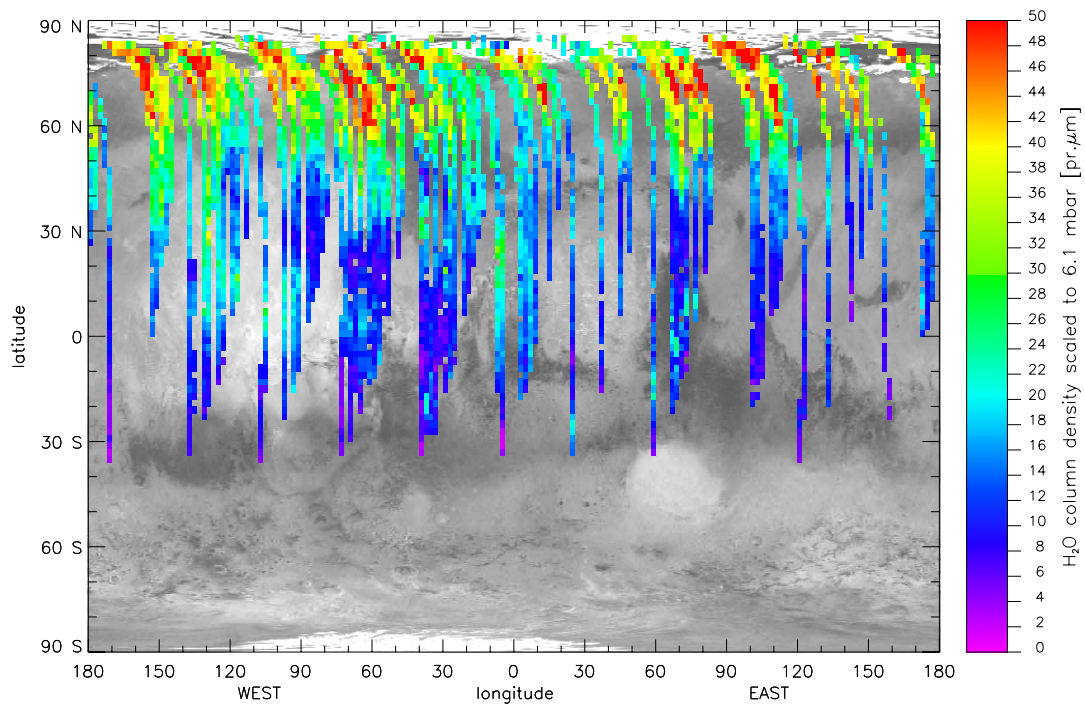


Figure 6.7: The spatial distribution of water vapour for the northern summer at  $L_S=90-135^\circ$ . The column densities, normalized to 6.1 mbar, are displayed up to 50  $\text{pr.}\mu\text{m}$ .

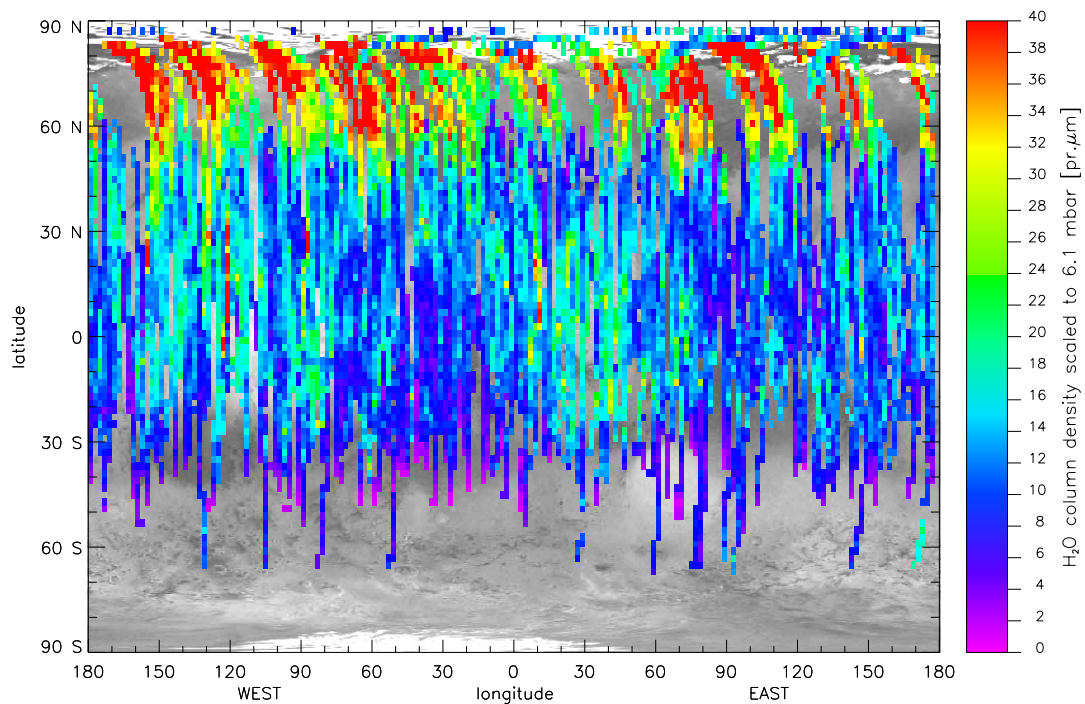


Figure 6.8: The spatial distribution of water vapour for the entire processed dataset. The column densities, normalized to 6.1 mbar, are displayed up to 40  $\text{pr.}\mu\text{m}$ .

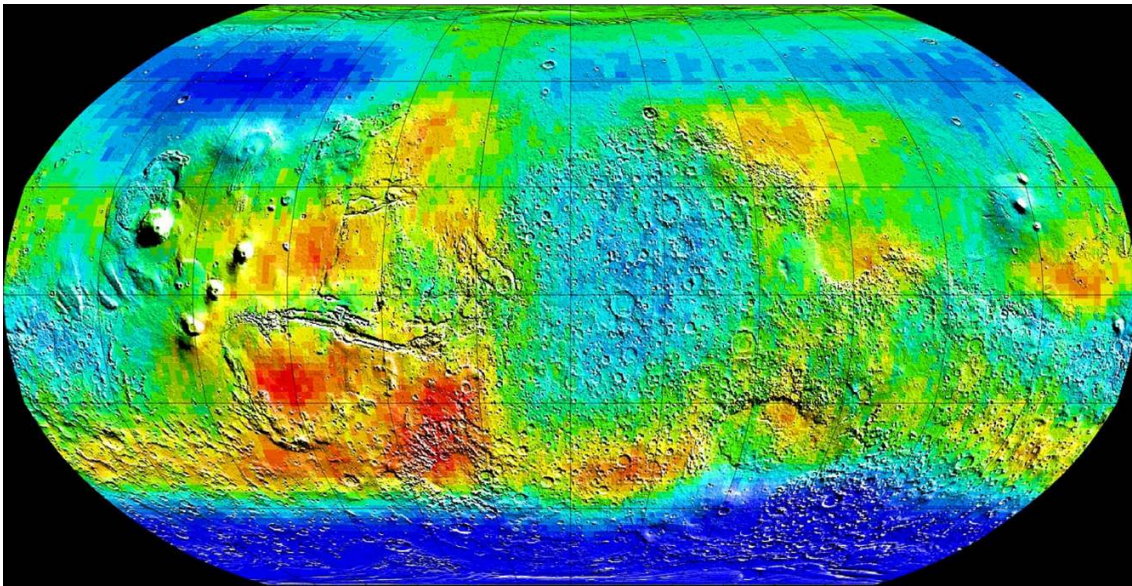


Figure 6.9: The epithermal neutron map based on data from the Neutron spectrometer of *Mars Odyssey* (adopted from Boynton et al. (2002)): blue regions correspond to a high amount of hydrogen in the uppermost soil; they are most pronounced poleward of  $60^\circ$  but also present over Arabia Terra (center of map) and the Medusae Fossae region (left edge of map; southwest of Olympus Mons).

cap which extends only to about  $80^\circ\text{N}$ , and around  $L_S=90^\circ$  the seasonal cap is already fully retreated as can be seen in images taken by the *Hubble Space Telescope* (see image 6.10). This leads to the conclusion that the subliming ice from the seasonal cap does not remain in the atmosphere. If this would be the case then one should see higher column densities than the observed maximum of 29 pr.  $\mu\text{m}$  at  $L_S=70-75^\circ$ . Montmessin et al. (2004) presented a convincing solution for this problem: the water vapour from the sublimation is transported by circulation further poleward and deposited on the cold permanent ice cap. Later during the height of summer also this ice sublimates and produces the observed  $\text{H}_2\text{O}$  peak ( $\sim 60$  pr.  $\mu\text{m}$ ). In addition, also subliming ice from the permafrost ground influences the polar water cycle because the summer maximum above  $40$  pr.  $\mu\text{m}$  reaches down till  $\sim 60^\circ\text{N}$  and is not confined to the direct vicinity of the polar cap.

Another very interesting point is the longitudinally inhomogeneous distribution of the water vapour near the polar cap. Between  $30^\circ\text{W}$  and  $10^\circ\text{E}$  there is a relative depletion which is not a seasonal effect as the orbits occurred at various times within  $L_S=90-135^\circ$ . Another but weaker minimum is located at  $110-120^\circ\text{W}$ . On the other hand also maxima can be identified, namely at  $120-160^\circ\text{W}$  which is identical with the maximum reported by Melchiorri et al. (2006), at  $45-100^\circ\text{W}$  and at  $60-110^\circ\text{E}$ . This unequal distribution might be a hint towards inhomogeneities in the process of sublimation and deposition in the polar area. These can be in turn caused by atmospheric wave phenomena, that accumulate moisture over certain preferred regions, or by properties of the underlying soil, like its composition and adsorption capability. A comparison with the next northern summer and an possible repeatability will give more clues to this matter.

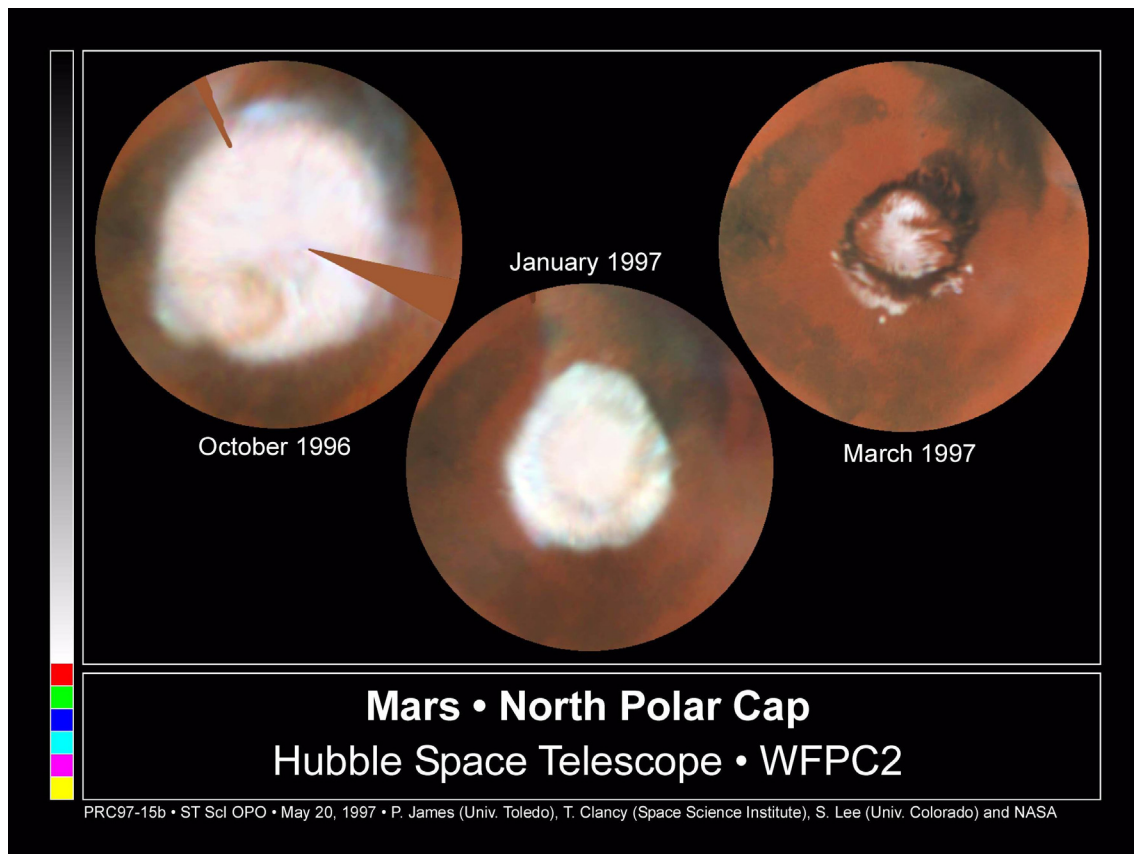


Figure 6.10: The development of the seasonal north pole cap in MY 23 as imaged by the *Hubble Space Telescope* (the maps extend from 50–90°N). The seasonal cap recedes from ~60°N at  $L_S=22^\circ$  (first image), to ~70°N at  $L_S=60^\circ$  (second image) and is completely sublimated by  $L_S=97^\circ$  (third image). Only the permanent cap remains (80–90°N).

## 6.4 Diurnal variations

Another topic which has been subject of earlier water vapour investigations is the presence of a diurnal variability caused by the exchange of  $H_2O$  molecules between the soil and the atmosphere (described explicitly in chapter 3.4). As mentioned before, the kind of orbit of *MEX* is not ideally suited for this task because the observations during a certain season cover only a short interval of local times (cf. figure 4.7). So for the time after  $L_S=90^\circ$  there is not evidence for diurnal variations (not explicitly shown). This is mainly caused by the insufficient coverage of local time and the strong seasonal variations.

However, between solar longitudes 335° and 70° a variation appears to be present, as can be seen in figure 6.11. Here the  $H_2O$  amounts, binned to a resolution of 0.1 hours, are given in column densities scaled to 6.1 mbar in order to remove possible topographic influences. Also those orbits have not been considered that are either very noisy (no. 72, 97, 100, 103 and 148) or are possibly showing the disappearing secondary maximum of the previous southern summer (no. 10, 20, 24, 30, 32, 37, 38, 41, 145, 202). Still, the remaining orbits tentatively indicate an increase of water vapour from the morning until early afternoon (13:30) by about 2–3  $\mu\text{m}$ . As the retrieval error of 20–30% for a datapoint

is further reduced by the binning of the results this H<sub>2</sub>O rise is significant. It is taking place between 45°S and 40°N (only around 20°S there is actually a decrease observed). However, this increase is certainly not by a factor of 2–3 like reported from previous measurements. Seasonal and spatial influences cannot be ruled out completely due to the few available orbits. New observations in future martian year should help to clarify this issue. If this lower than previously reported increase of abundances from morning to midday should be confirmed it would set new upper limits on the capability of the regolith to adsorb water.

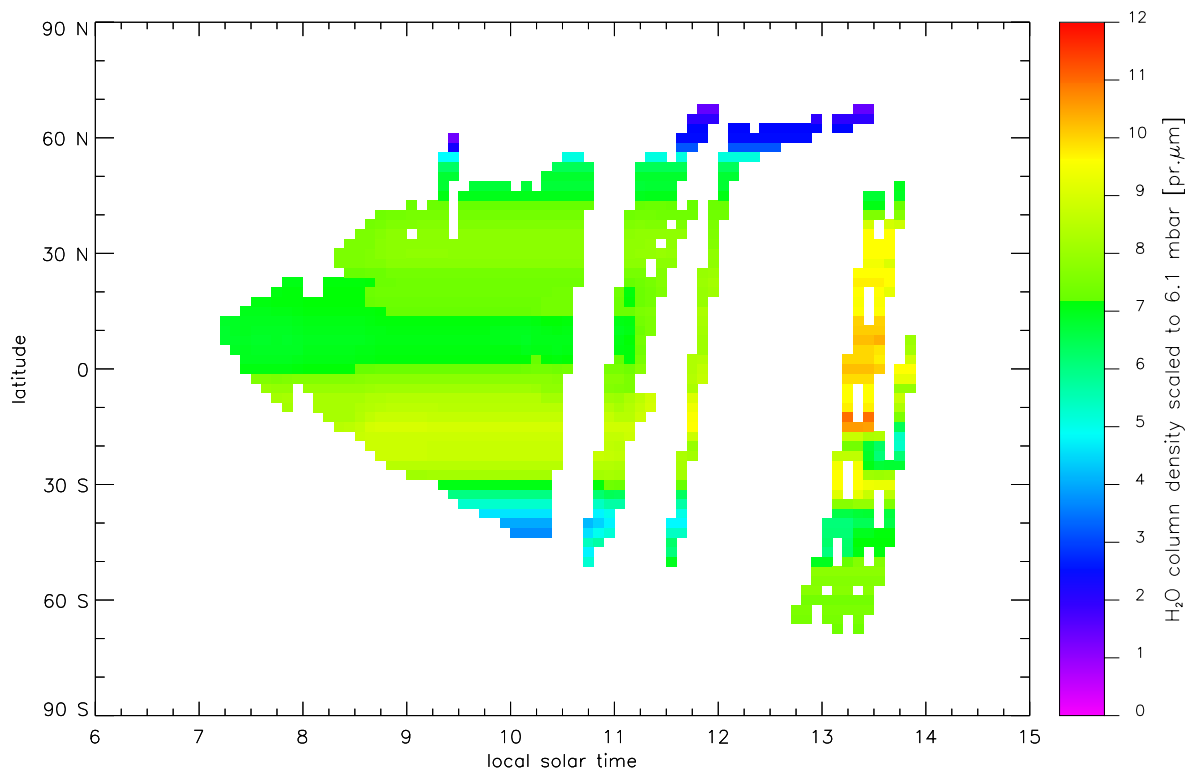


Figure 6.11: The covered local solar time for  $L_S=330-70^\circ$ . The column density, scaled to 6.1 mbar, is clearly rising from the morning hours until 13:30 by 2–3 pr.  $\mu\text{m}$ .

## 6.5 Comparison of results from individual orbits

The *Mars Express* mission has the great advantage of operating three spectrometers in parallel that are capable of measuring atmospheric water. This enables a direct comparison of their results<sup>1</sup>. In figures 6.12 to 6.20 the retrievals are marked like this:

<sup>1</sup>This work was initiated in the workshop "Water in the Martian atmosphere: comparison of recent datasets" at the ISSI in Bern (organized by O. Korabiev) that brought together research teams working about water vapour on Mars with the *MEX* spectrometers, TES and groundbased observations.

symbol	instrument	working group
dark grey plus signs	PFS/LW (F)	Thierry Fouchet
light green plus signs	PFS/LW (I)	Nikolay Ignatiev
red triangles	<i>MGS</i> /TES	Mike Smith (corrected database)
blue crosses	PFS/SW	this work
green boxes	EMCD 4.1	general circulation model
orange diamonds	OMEGA	Luca Maltagliati
brown asterisk	SPICAM	Anna Fedorova

In the upper panels of the figures the saturation cutoff was determined by the temperature profile (described in chapter 5.3.1). In the lower panels all the water was confined below a height of 2.5 km above the surface. The implication of this confinement to the boundary layer of the atmosphere is subject of section 6.7 while in this section only the upper panels are relevant. In the figures there is also the surface altitude plotted below the results (solid black line), including the saturation level if it is lower than one scale height above the surface (dotted black line).

Not only are the retrieved H<sub>2</sub>O amounts of the three spectrometers shown but also the corrected ones of TES because there is an overlap in seasonal coverage up to *MEX* orbit 770. However, the TES spectra were recorded constantly at 14:00 local solar time and are not precisely from the same locations. The TES results are binned within  $\pm 2.5^\circ$  of solar longitude and  $\pm 3.75^\circ$  of topographic longitude. In addition, also the theoretically expected column densities of the EMCD 4.1 database are presented. The following description of results refers only to the upper panels of the figures because there the saturation determination is the same for all instruments.

At this point it is appropriate to briefly describe the correction of the TES database because this correction resulted from the intercomparison of all datasets at ISSI in Bern. Originally, the TES results were based on measurements at a resolution of either  $6.25\text{ cm}^{-1}$  or  $12.5\text{ cm}^{-1}$ , using the water bands at  $250\text{ cm}^{-1}$ ,  $280\text{ cm}^{-1}$ ,  $300\text{ cm}^{-1}$  and  $330\text{ cm}^{-1}$ . With the  $6.25\text{ cm}^{-1}$  resolution these four bands yield consistent results. Yet with the  $12.5\text{ cm}^{-1}$  resolution the measurements in the bands of  $300\text{ cm}^{-1}$  and  $330\text{ cm}^{-1}$  give much larger H<sub>2</sub>O amounts than those in the  $250\text{ cm}^{-1}$  and  $280\text{ cm}^{-1}$  bands. Neglecting the  $300\text{ cm}^{-1}$  and  $330\text{ cm}^{-1}$  bands, and using only the data with  $12.5\text{ cm}^{-1}$  resolution the retrieved abundances are by about 30% lower than originally published. A more detailed statement is given by Fouchet et al. (2006).

Another obvious result of the intercomparisons is the need to improve the EMCD model since its calculated water amounts are systematically higher than the measured ones. Up to now the EMCD water determination was calibrated with the TES database. In general, the new remote sensing results are consistent in the shape of the latitudinal distribution but show disagreements, too. Particularly interesting for this work is the comparison between PFS/LW and PFS/SW results<sup>2</sup>. Apart from orbits 348 (figure 6.14) and 357 (figure 6.15), that are in good agreement, the SW results are always slightly higher than the LW ones. The reason for this lies in the pursued retrieval methods with their ample room for errors as both LW and SW expect uncertainties in the order of 25%. So within error bars there is an agreement of the measurements for most of the orbits.

<sup>2</sup>The PFS/LW results are in agreement independently of the working group (Fouchet or Ignatiev).

However, pronounced disagreements are visible northward of  $50^{\circ}\text{N}$  in the northern summer as seen for example in orbit 1023 (figure 6.18) which cannot be solely explained by retrieval uncertainties. Here a physical reason seems more likely which will be addressed in section 6.7.

Now a few words about the other instruments. SPICAM amounts represent always the lowest boundary, apart from high latitudes in the northern summer, due to stray light and instrumental effect. Contrary to that, the column densities of TES appear to be slightly higher; only orbit 397 is in good agreement. This difference can certainly be accounted to the different local solar times, footprint locations and applied techniques. Lastly, the OMEGA results, that are retrieved from the  $2.6\mu\text{m}$  band under consideration of saturation, are mainly in agreement with the results of this work (orbits 37, 357, 1023, 1200), sometimes higher (orbit 1177) and sometimes lower (orbit 278). As the same  $\text{H}_2\text{O}$  band is analysed the most likely explanation of the discrepancies are again retrieval uncertainties, especially since the general shape of the latitudinal distribution is consistent with this work<sup>3</sup>.

In summary, the retrievals of all the instruments have errors in the order of 20–30%. Within these uncertainties the results are mainly consistent. However, in some cases the difference is much larger than the estimated error, which affects especially the PFS/LW and PFS/SW results. An explanation for these cases will be given in chapter 6.7.

---

<sup>3</sup>The higher amounts north of  $\sim 28^{\circ}\text{N}$  of orbit 357 are caused by instrumental problems of OMEGA.

## 6 Results and discussion

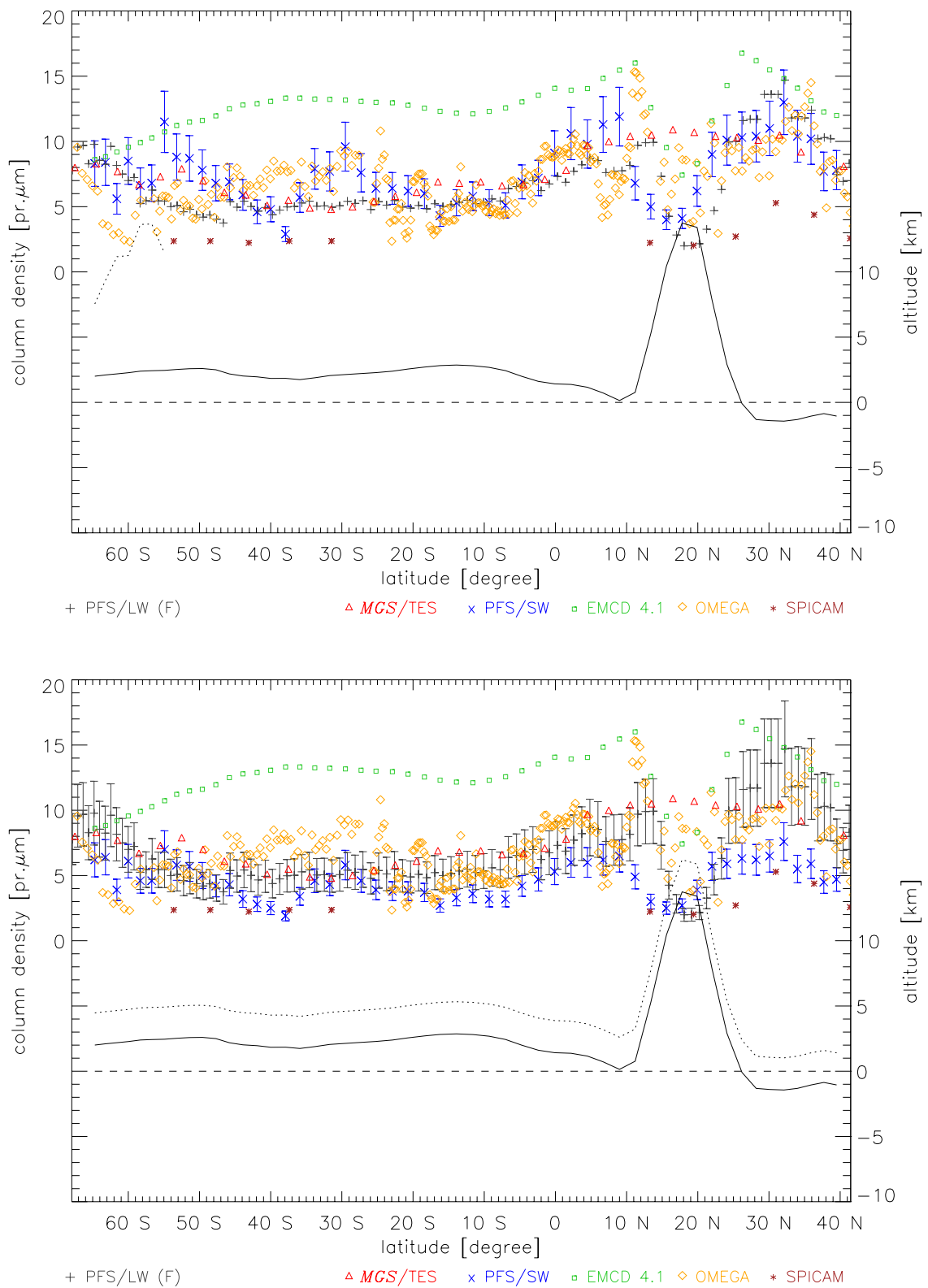


Figure 6.12: Results of various instruments for orbit 37 ( $L_S=337^\circ$ ) with regular saturation cutoff (upper panel) and with a confinement below 2.5 km (lower panel). For clarity only the lower panel contains PFS/LW error bars. This orbit passed over Olympus Mons.

## 6.5 Comparison of results from individual orbits

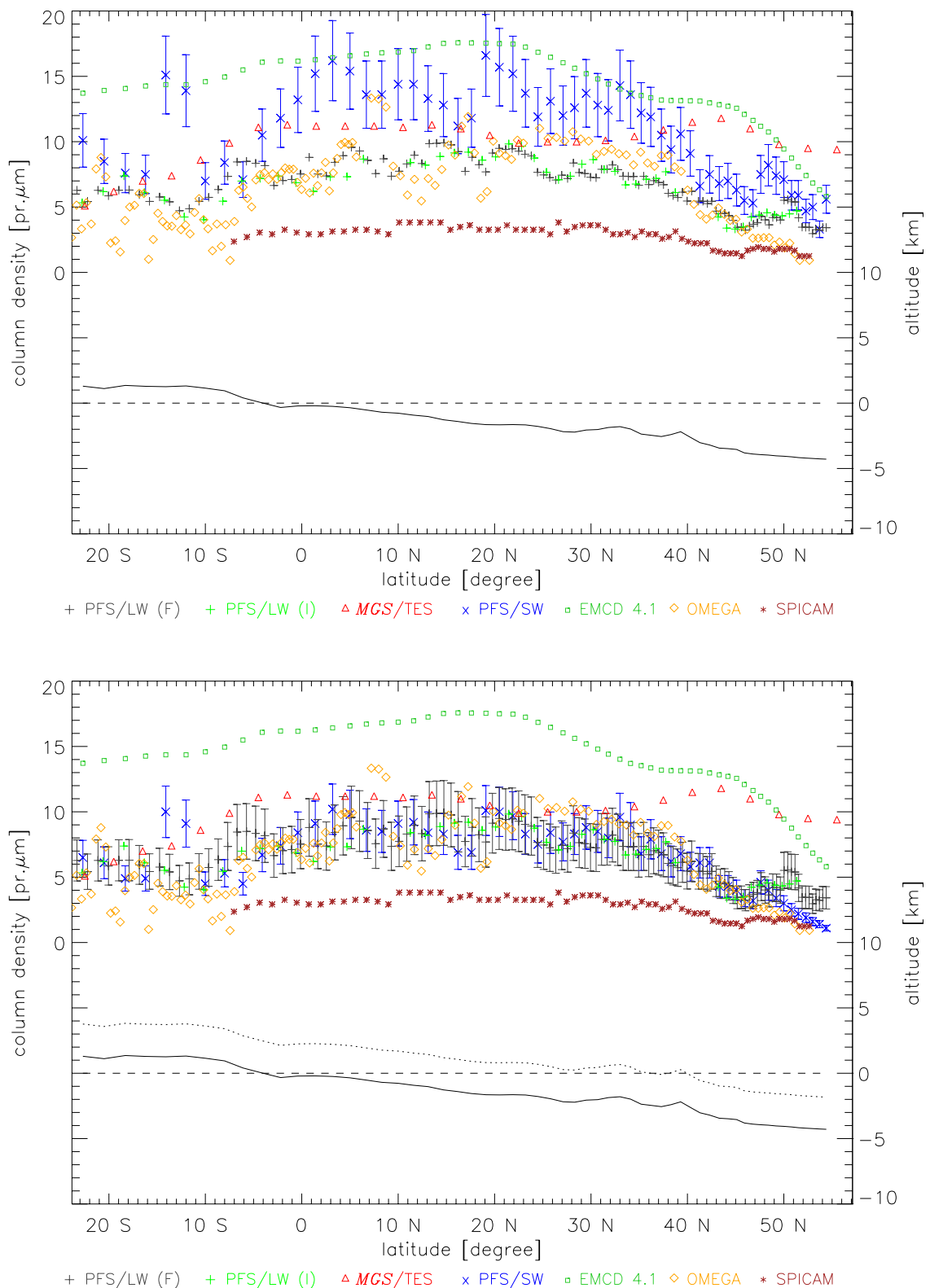


Figure 6.13: Results of various instruments for orbit 278 ( $L_S=16^\circ$ ) with regular saturation cutoff (upper panel) and with a confinement below 2.5 km (lower panel). For clarity only the lower panel contains PFS/LW error bars. This orbit passed over Arabia Terra.

## 6 Results and discussion

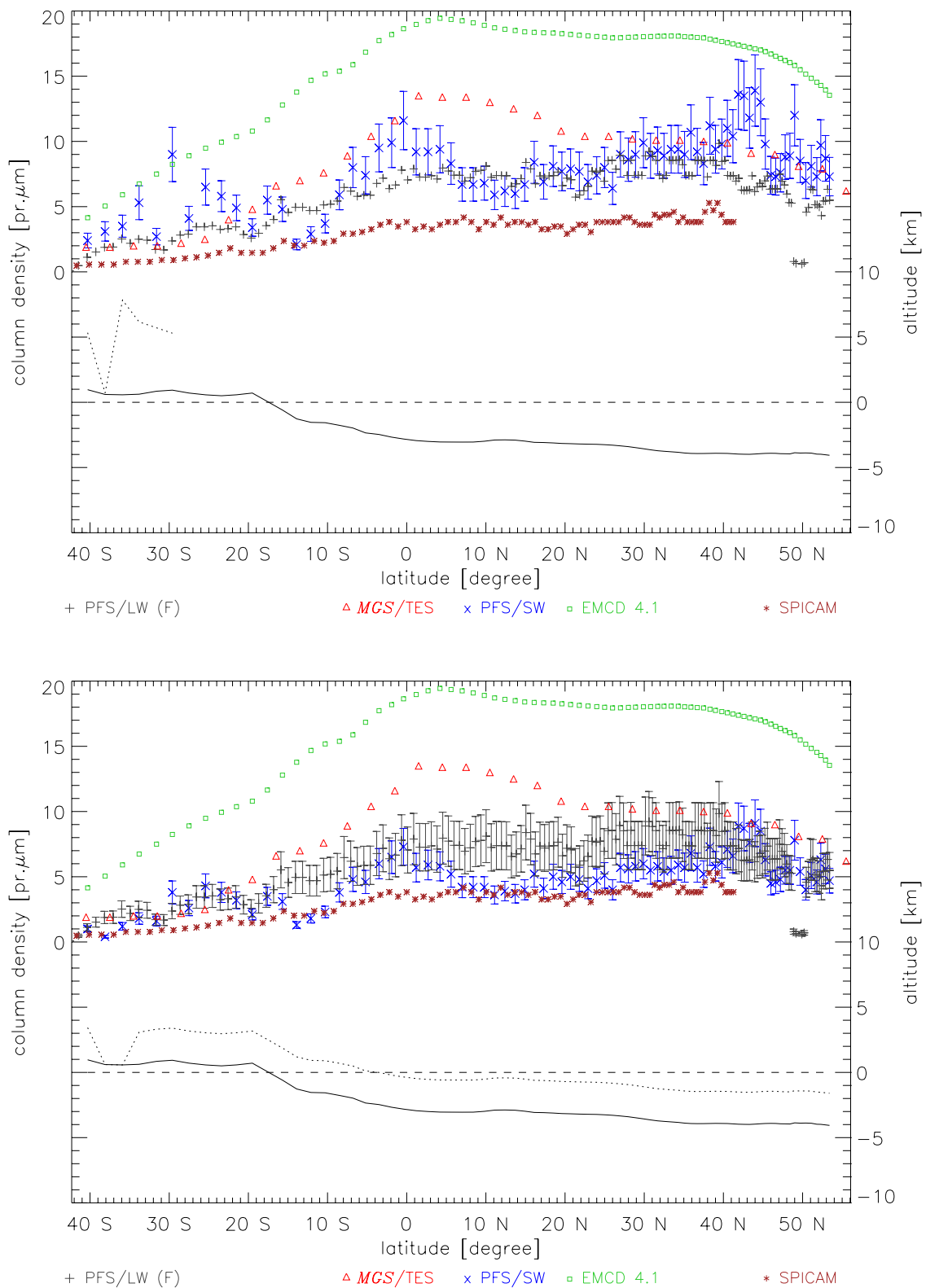


Figure 6.14: Results of various instruments for orbit 348 ( $L_S=26^\circ$ ) with regular saturation cutoff (upper panel) and with a confinement below 2.5 km (lower panel). For clarity only the lower panel contains PFS/LW error bars.

## 6.5 Comparison of results from individual orbits

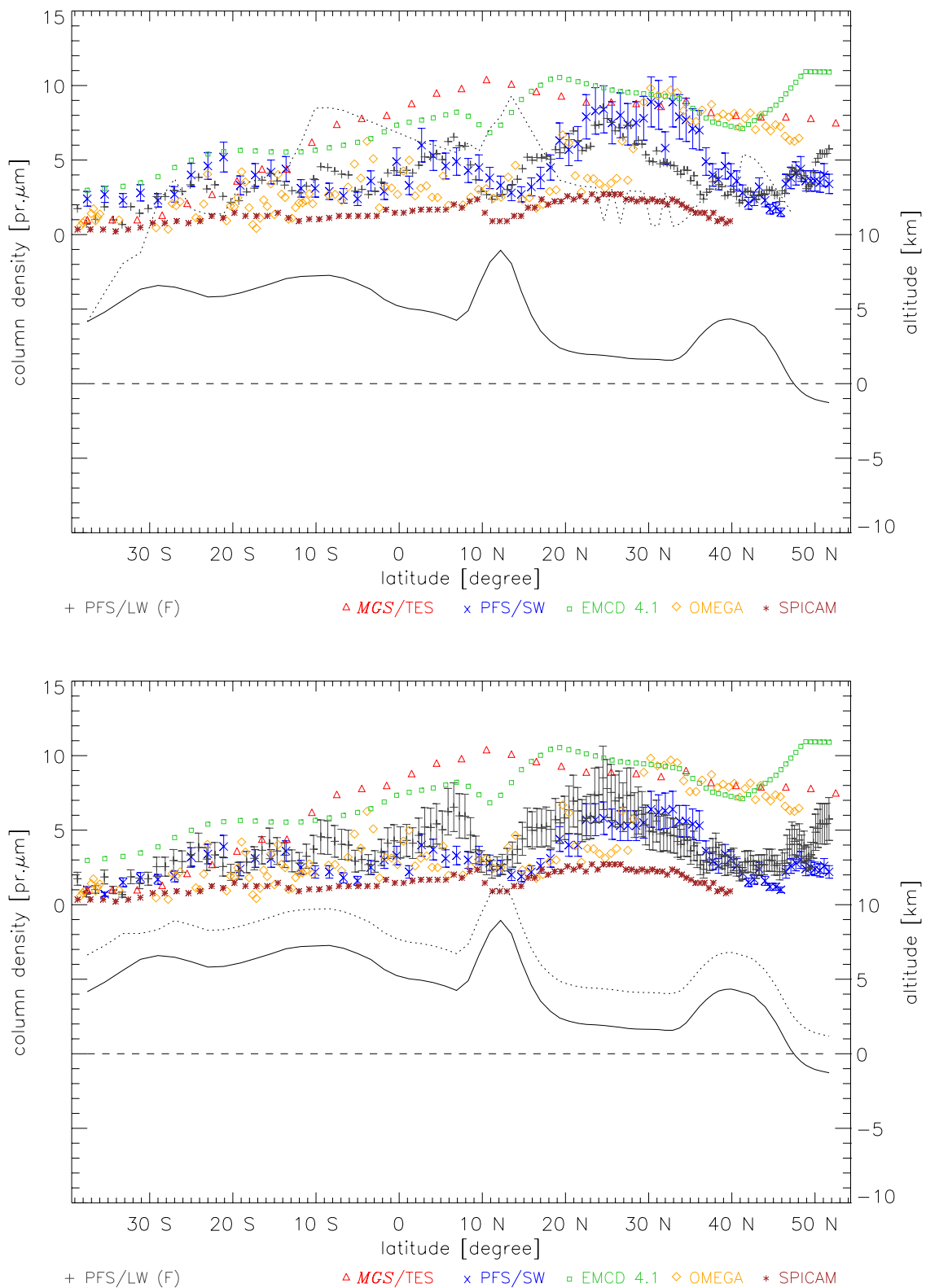


Figure 6.15: Results of various instruments for orbit 357 ( $L_S = 27^\circ$ ) with regular saturation cutoff (upper panel) and with a confinement below 2.5 km (lower panel). For clarity only the lower panel contains PFS/LW error bars. This orbit passed over Tharsis.

## 6 Results and discussion

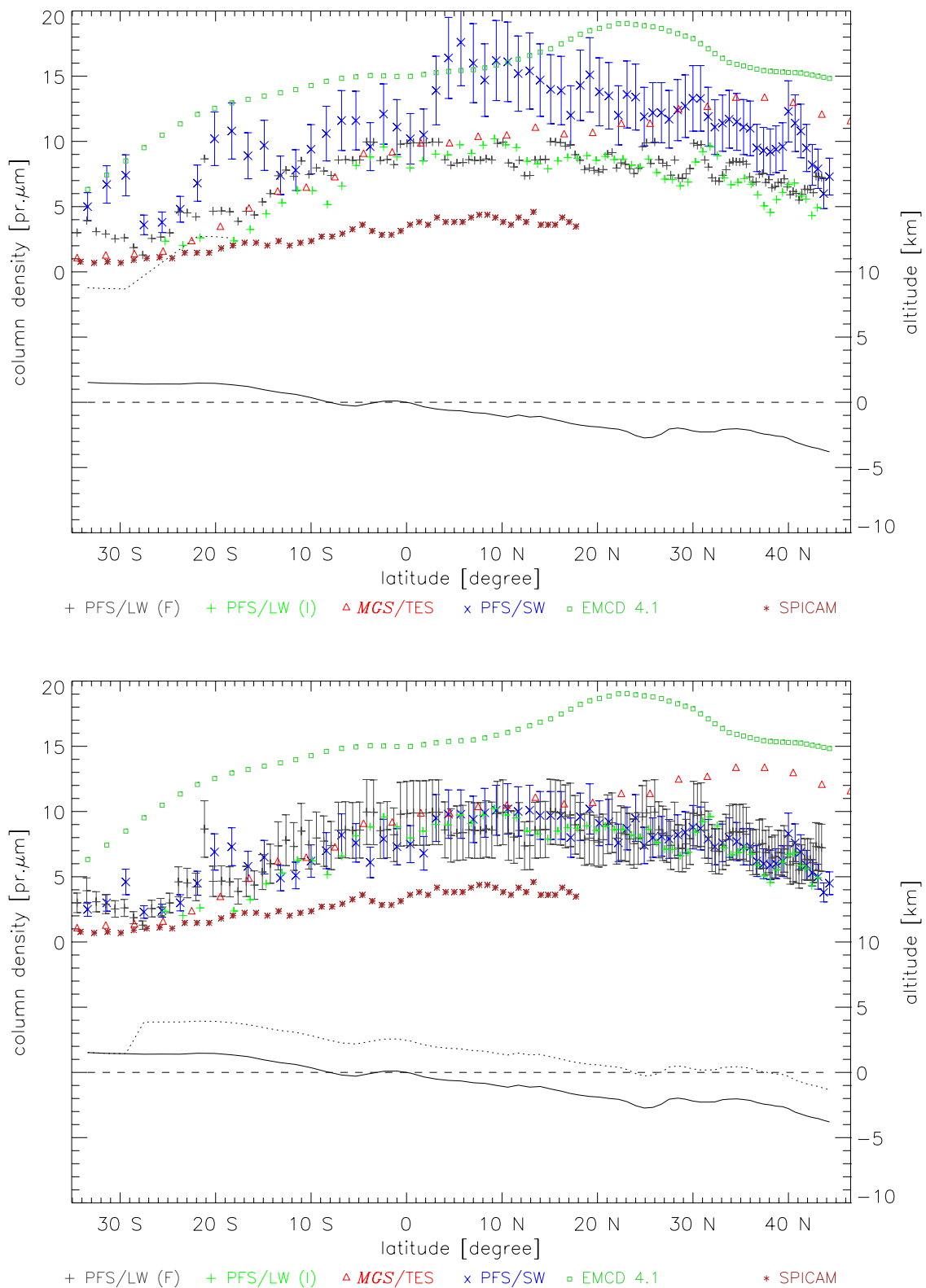


Figure 6.16: Results of various instruments for orbit 397 ( $L_S = 33^\circ$ ) with regular saturation cutoff (upper panel) and with a confinement below 2.5 km (lower panel). For clarity only the lower panel contains PFS/LW error bars. This orbit passed over Arabia Terra.

## 6.5 Comparison of results from individual orbits

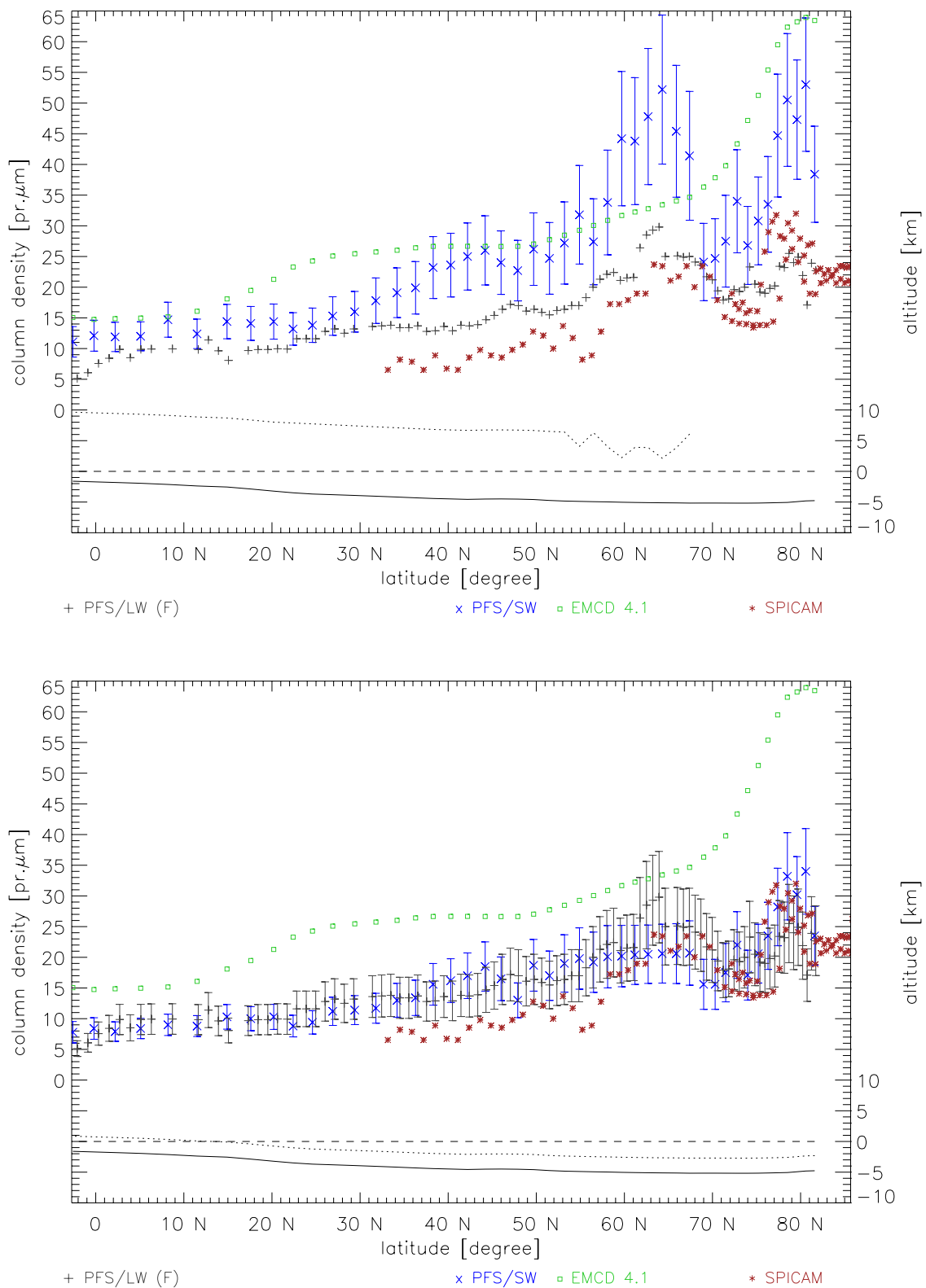


Figure 6.17: Results of various instruments for orbit 1011 ( $L_S = 109^\circ$ ) with regular saturation cutoff (upper panel) and with a confinement below 2.5 km (lower panel). For clarity only the lower panel contains PFS/LW error bars.

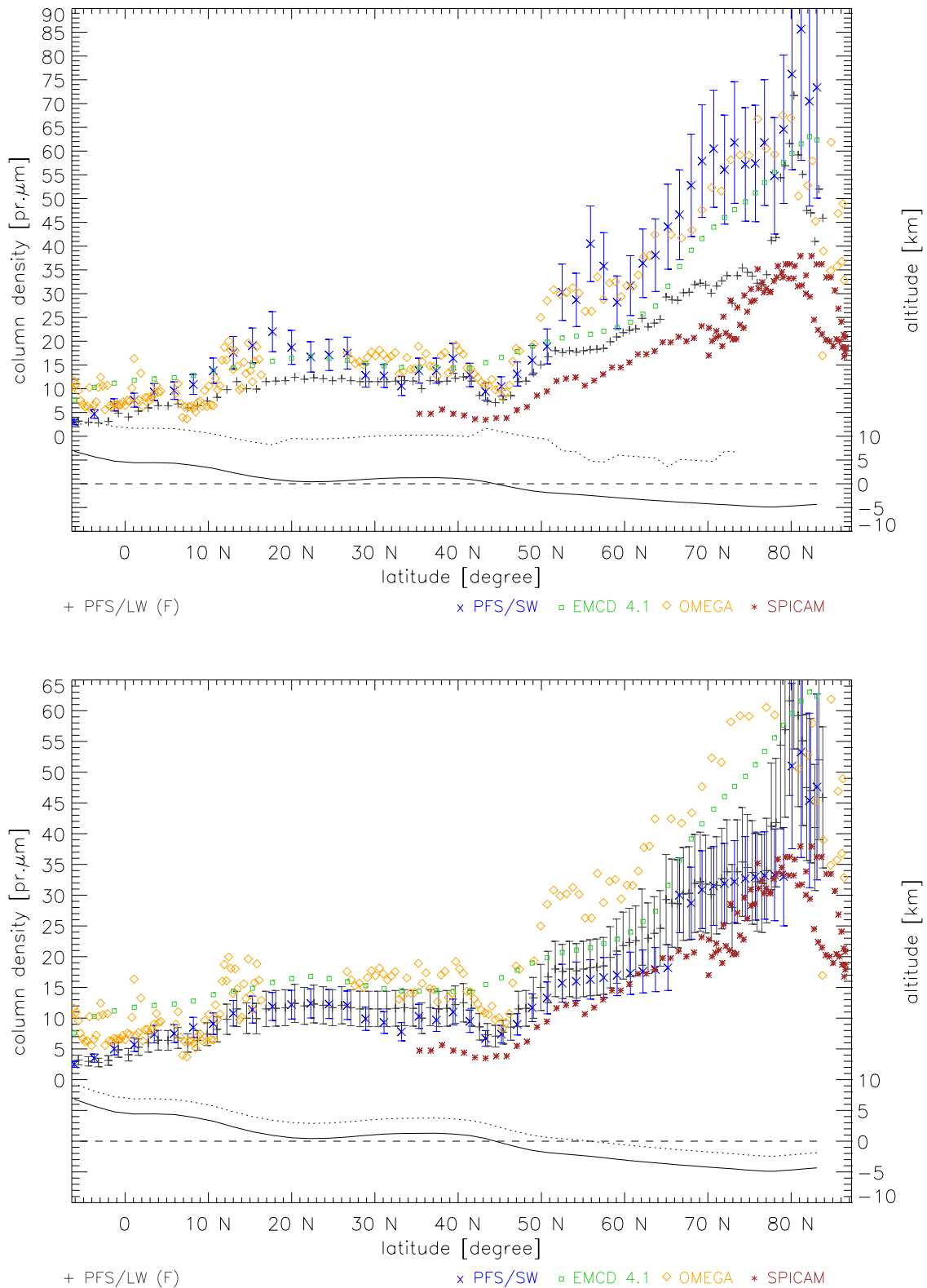


Figure 6.18: Results of various instruments for orbit 1023 ( $L_S = 111^\circ$ ) with regular saturation cutoff (upper panel) and with a confinement below 2.5 km (lower panel). For clarity only the lower panel contains PFS/LW error bars.

## 6.5 Comparison of results from individual orbits

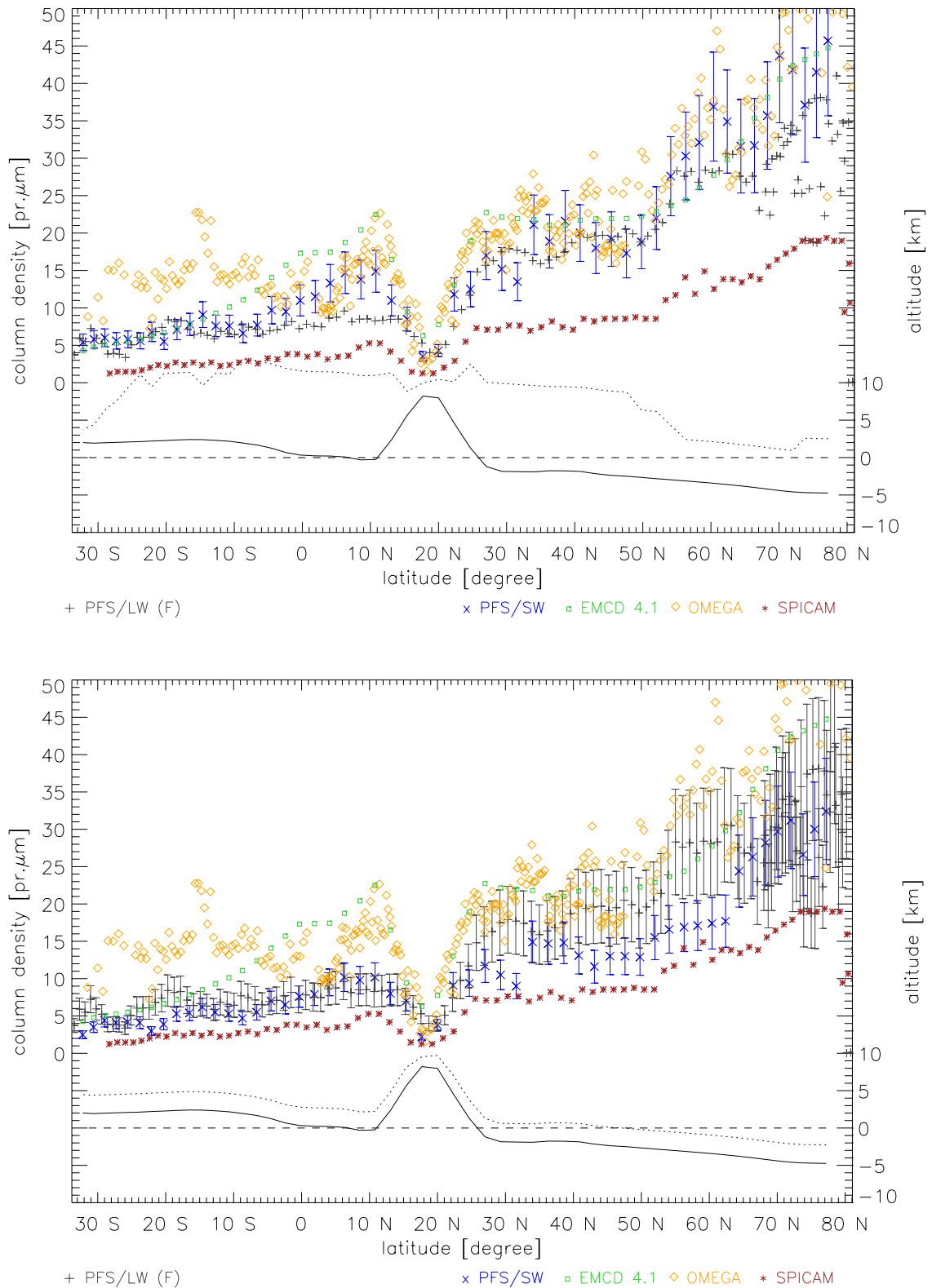


Figure 6.19: Results of various instruments for orbit 1177 ( $L_S = 131^\circ$ ) with regular saturation cutoff (upper panel) and with a confinement below 2.5 km (lower panel). For clarity only the lower panel contains PFS/LW error bars. This orbit passed over Olympus Mons.

## 6 Results and discussion

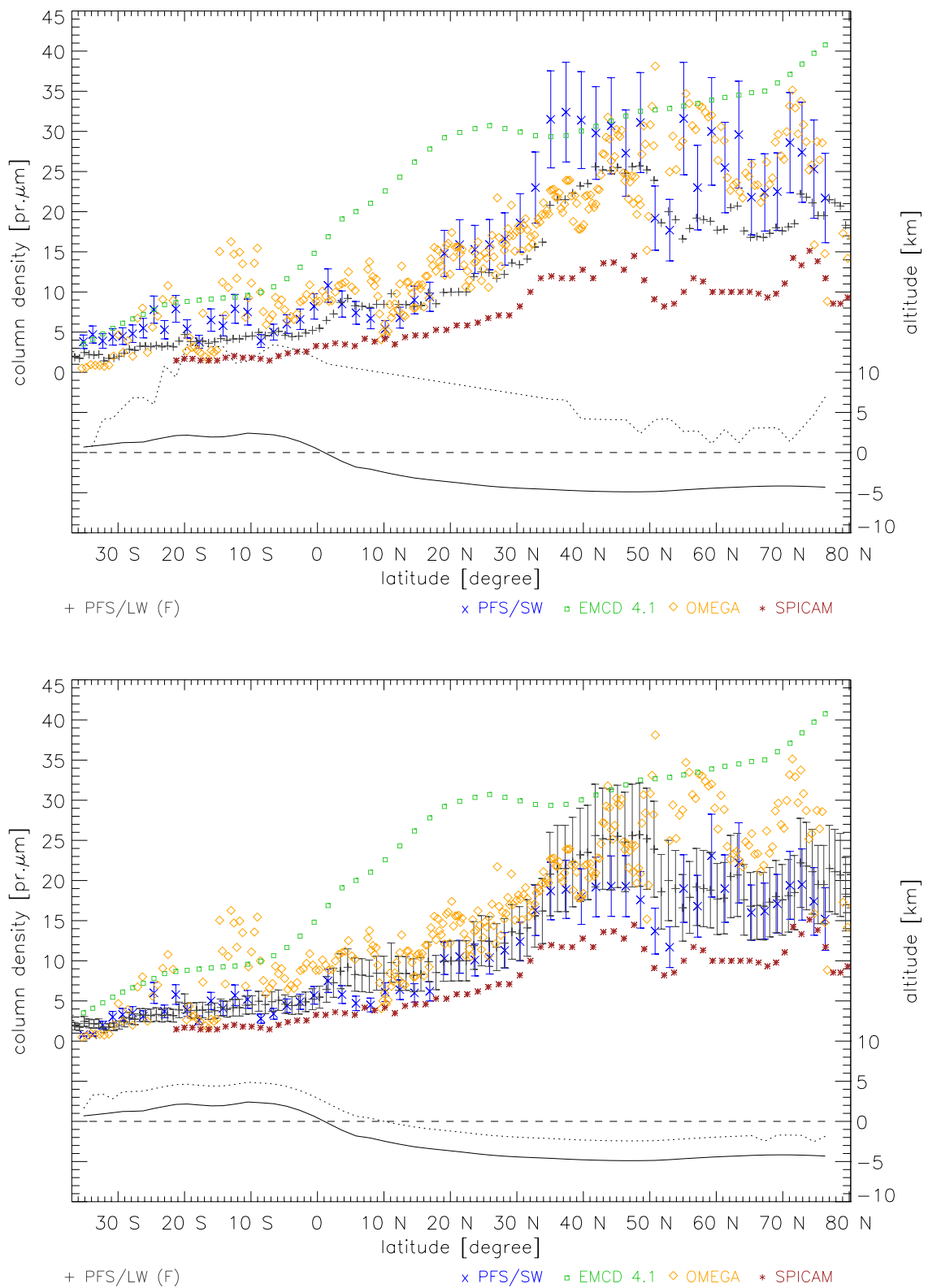


Figure 6.20: Results of various instruments for orbit 1200 ( $L_S = 134^\circ$ ) with regular saturation cutoff (upper panel) and with a confinement below 2.5 km (lower panel). For clarity only the lower panel contains PFS/LW error bars.

## 6.6 Comparison of the global water behaviour

For a quantitative comparison between results one has to keep in mind the varying applied techniques and coverage, in particular when comparing data from various times of the day and different years. Here both earlier measurements and recent results from the other *MEX* spectrometers are included in the comparison. The detailed listing of these measurements and the used instruments was given in chapter 3.1 (page 33).

The period between solar longitude  $330^\circ$  and  $60^\circ$  exhibits large variations for different observations, up to a factor of 3 among results from Rizk et al. (1991), Clancy et al. (1992), Sprague et al. (1996) and also with respect to the ones of MAWD, *Phobos 2*, and TES. Those spacecraft observations are in agreement among each other, though, and the current measurements of OMEGA and PFS/LW confirm them. Only SPICAM data give systematically lower results which happens most likely due to stray light in the instrument optics (Fedorova et al. 2006). A comprehensive analysis of the OMEGA dataset was performed by Melchiorri et al. (2006) in the  $2.6\ \mu\text{m}$  band. The findings during this season range between 3 and 15 pr.  $\mu\text{m}$ , depending on the location. Now the results of this work are generally in agreement with all those spacecraft measurements. For example, the column densities of 7–10 pr.  $\mu\text{m}$ , found by TES after the new data analysis (private communication, Smith 2006) around  $\pm 20^\circ$  latitude from the equator, agree well with the average value of 7.9 pr.  $\mu\text{m}$  found in this work. Also the  $\sim 8$  pr.  $\mu\text{m}$  at  $0\text{--}30^\circ$  reported by the PFS/LW team (Fouchet et al. 2006) are confirmed by PFS/SW (mean 8.3 pr.  $\mu\text{m}$ ). Finally, further north 5–10 pr.  $\mu\text{m}$  are detected by both TES and PFS/SW.

For the time around northern autumn equinox the measurement discrepancies for all observations are not as significant and might be due to different local times and observation spots. Between the equator and northern low latitudes they are:

- corrected MAWD 15–20 pr.  $\mu\text{m}$  (Fedorova et al. 2004)
- corrected TES 17 pr.  $\mu\text{m}$  at the Pathfinder coordinates ( $19.3^\circ\text{N}$ ,  $33.6^\circ\text{W}$ )
- Pathfinder itself only  $6\pm 4$  pr.  $\mu\text{m}$  for  $L_S=150^\circ$  (Titov et al. 1999)
- $12\pm 3.5$  pr.  $\mu\text{m}$  shortly after those measurements around  $L_S=160^\circ$  with *ISO* (Burgdorf et al. 2000)
- $12\pm 6$  pr.  $\mu\text{m}$  at  $L_S=166^\circ$  during the global dust storm of MY 25 with *SWAS* (Gurwell et al. 2005)
- $13\pm 3$  pr.  $\mu\text{m}$  at  $L_S=204^\circ$  of MY 26 with *ODIN* (Biver et al. 2005)
- $17\pm 9$  pr.  $\mu\text{m}$  at  $L_S=206^\circ$  of the same year with *IRTF* (Encrenaz et al. 2005a)
- 10–15 pr.  $\mu\text{m}$  at  $L_S=208^\circ$  by Rizk et al. (1991)
- SPICAM traces the southward movement of the post-summer maximum which reaches  $30\text{--}35^\circ\text{N}$  latitudes at  $L_S=150^\circ$ . The column density of this peak is given with 12–14 pr.  $\mu\text{m}$  (Fedorova et al. 2006).
- 10–18 pr.  $\mu\text{m}$ , depending on the location, are seen by the PFS/LW channel for the equinox period (Fouchet et al. 2006)

This work delivers slightly higher values. For example during  $L_S=140\text{--}170^\circ$  between  $30^\circ\text{S}$  and  $30^\circ\text{N}$  there are on average  $12.4\text{ pr. }\mu\text{m}$  detected by PFS/SW while PFS/LW finds values around  $10\text{ pr. }\mu\text{m}$  (Fouchet et al. 2006). For  $L_S=165\text{--}200^\circ$  the global mean values are  $13.9\text{ pr. }\mu\text{m}$  for the SW and  $\sim 12\text{ pr. }\mu\text{m}$  for the LW channel.

Due to the large variability of the results at the equinoxes it could be reasonable at the moment to use the two summer maxima for comparisons between different years and datasets. Since the northern summer is a relatively clear, dust-free season these results should be particularly suitable for intercomparisons of  $\text{H}_2\text{O}$  (anyway the southern summer is not covered by this work). In the northern summer only the detection of Sprague et al. (1996) with the maximum of  $36.4\text{ pr. }\mu\text{m}$  at  $71.2^\circ\text{N}$  at  $L_S=100^\circ$  is an outlier compared to other results. Northward of  $60^\circ\text{N}$  the following detections were made:

- summer maximum of  $\sim 75\text{ pr. }\mu\text{m}$  by MAWD (Fedorova et al. 2004)
- $40\text{--}45\text{ pr. }\mu\text{m}$  before and after summer solstice of MY 23 by Sprague et al. (2003)
- $43\text{--}76\text{ pr. }\mu\text{m}$  at  $L_S=105\text{--}115^\circ$  of MY 24 by Sprague et al. (2001, 2006)
- maximum values of  $55\text{--}65\text{ pr. }\mu\text{m}$  by TES (corrected database) in MY 24, maxima of  $65\text{--}75\text{ pr. }\mu\text{m}$  in MY 25 and  $55\text{--}75\text{ pr. }\mu\text{m}$  in MY 26
- SPICAM sees only  $55\text{ pr. }\mu\text{m}$  for the northern maximum during solar longitudes  $110^\circ$  to  $120^\circ$  and  $25\text{--}35\text{ pr. }\mu\text{m}$  at  $60^\circ\text{N}$  latitude (Fedorova et al. 2006)
- for latitudes around  $60^\circ\text{N}$  Encrenaz et al. (2005b) reported a rise from  $25\text{ pr. }\mu\text{m}$  at the beginning to  $45\text{ pr. }\mu\text{m}$  in the end of the OMEGA measurements analysed for  $L_S=94\text{--}112^\circ$  of MY 27 ; at  $80^\circ\text{N}$  a mean maximum of  $55\text{ pr. }\mu\text{m}$  was found. For all these values an error of 30% was stated.
- another OMEGA retrieval between  $L_S=93\text{--}126^\circ$  by Melchiorri et al. (2006) yielded on average  $30\text{--}50\text{ pr. }\mu\text{m}$  at  $70^\circ\text{N}$ , a maximum with  $40\text{--}70\text{ pr. }\mu\text{m}$  at  $80^\circ\text{N}$  and only  $30\text{ pr. }\mu\text{m}$  at  $90^\circ\text{N}$ . Also here an error of 30% was assumed.
- $30\text{--}60\text{ pr. }\mu\text{m}$  are detected with the LW channel of PFS (Fouchet et al. 2006)

The retrieved column densities of this work are in good agreement with all those results. They range from  $40$  to  $65\text{ pr. }\mu\text{m}$  north of  $60^\circ\text{N}$ , with the maxima localized around  $70\text{--}75^\circ\text{N}$ . Now further south around  $40^\circ\text{N}$  the reported values of previous observations are:

- $20\text{--}40\text{ pr. }\mu\text{m}$  by MAWD (during  $L_S=100\text{--}120^\circ$  as seen in Fedorova et al. (2004))
- $\sim 30\text{ pr. }\mu\text{m}$  at  $L_S=105\text{--}115^\circ$  of MY 24 by Sprague et al. (2006)
- mean values of approximately  $20\text{ pr. }\mu\text{m}$  with maxima around  $35\text{ pr. }\mu\text{m}$  by TES (consistent for all three observed northern summers)
- $12\text{--}15\text{ pr. }\mu\text{m}$  by SPICAM (Fedorova et al. 2006)
- $20\text{--}25\text{ pr. }\mu\text{m}$  at  $L_S=94\text{--}112^\circ$  by OMEGA (Encrenaz et al. 2005b)
- $\sim 20\text{ pr. }\mu\text{m}$  by PFS/LW (Fouchet et al. 2006)

Around  $40^{\circ}\text{N}$  the mean column density found in this work is  $19.8 \text{ pr. } \mu\text{m}$  with a maximum amount of  $42.4 \text{ pr. } \mu\text{m}$ , which agrees well with the other reports.

A direct comparison with PFS/LW results of Fouchet et al. (2006) shows that especially for high latitudes the SW results are systematically higher than the LW ones. In general, the seasonal cycle covered by PFS/LW in the first half martian year is in good agreement with MAWD or TES (using the corrected TES values). Also the southward transport is traced, i.e. the column density peak of  $20 \text{ pr. } \mu\text{m}$  migrates from  $55^{\circ}\text{N}$  during  $L_S=95^{\circ}$  to  $40^{\circ}\text{N}$  at  $L_S=120^{\circ}$ . Figure 6.21 shows the spatial distribution of the water vapour column density (normalized to 6.1 mbar) for the entire processed dataset ranging from  $L_S=330^{\circ}$  to  $210^{\circ}$ . As also seen in the result of this work in figure 6.8 the summer maximum shows a longitudinally inhomogeneous distribution and local maxima over the Tharsis and Arabia Terra region are clearly visible.

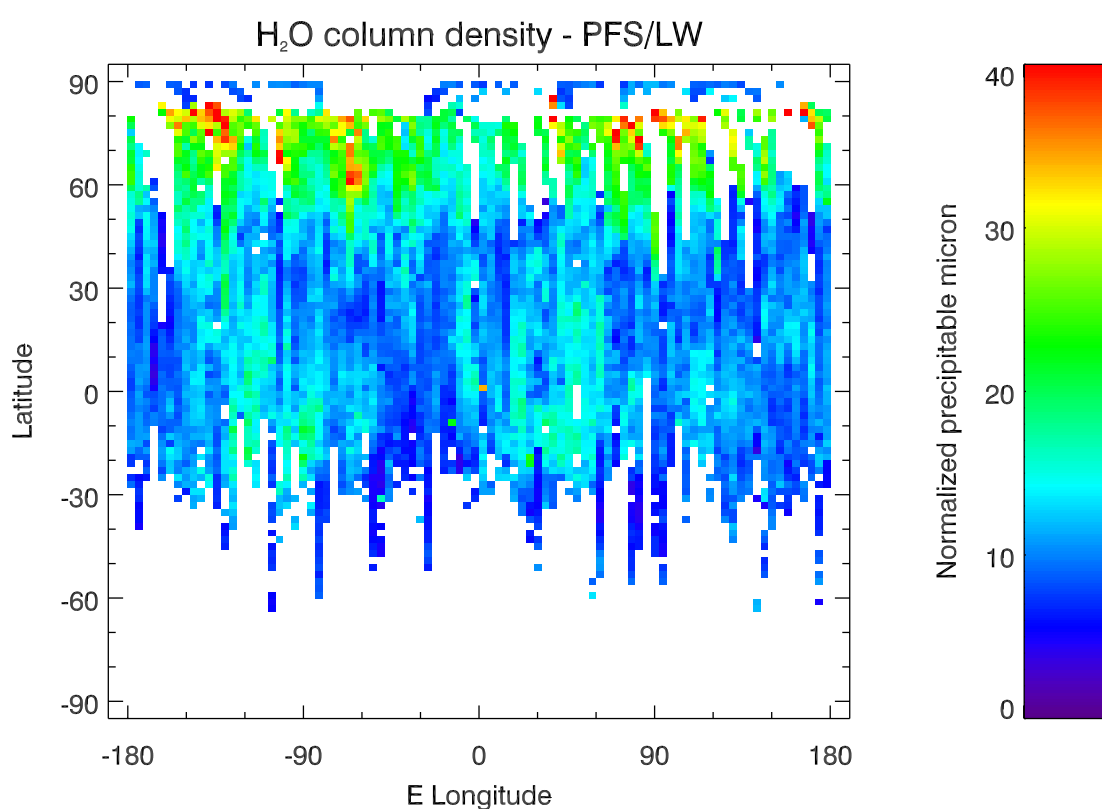


Figure 6.21: The geographic distribution of the normalized water column density for  $L_S=330\text{--}210^{\circ}$  as retrieved by PFS/LW. The northern summer maximum and local maxima over Tharsis and Arabia Terra are well visible.

In conclusion, it is difficult to see significant differences in the amplitudes of atmospheric  $\text{H}_2\text{O}$  amounts between various martian years. This is due to the large uncertainties for all retrievals (generally an error between 20% and 30% is stated), and the different samples in season and geographic location. Therefore a constantly repeating water cycle seems more likely. However, this would only be true for times with clear atmospheres. The southern summer with its varying dust content has still the largest potential for new insights but in MY 27 it was unfortunately not covered by PFS.

## 6.7 Vertical distribution

A direct retrieval of the vertical distribution of water vapour from one spectral band is only possible if the spectral lines can be resolved (like in the microwave range). However, the comparison of results from the SW bands with those of the thermal infrared (LW bands) allows in principle an assessment of the H<sub>2</sub>O profile because these channels have a different response to the temperature profile (Formisano et al. 2004). Naturally the LW retrievals depend more strongly on the temperature profile. Especially the lower 1–3 km play a significant role, where the lines can be seen in absorption, which is the assumed case, or in emission in the event of a temperature inversion. For special cases of such a temperature inversion the retrieval comparison might even be impossible, though.

Now in section 6.5 it was mentioned that the column densities retrieved by the SW channel of PFS are often significantly larger than those retrieved by the LW channel. This difference is the strongest over northern high-latitude areas during the northern summer where processing and instrumental uncertainties cannot be the only explanation anymore. Hence another vertical distribution of the water vapour was assumed, namely the confinement of all water within the lowest 2.5 km of the atmosphere and no water above this boundary. Consequently, less water is necessary to fit the observed spectral depth. The results of this forced confinement are displayed in the lower panels of figures 6.12 to 6.20 where the error bars are added for the LW retrievals (expected to be ~25%). Interestingly, the agreement with the PFS/LW results is now much better in many cases, especially for the northern summer observations.

Now one might argue that the LW retrieval incorporates a varying saturation level depending on the temperature while the SW has a fixed cutoff. However, Fouchet et al. (2006) have shown, in particular for orbit 1023, that for the LW channel the resulting H<sub>2</sub>O amounts depend only very weakly on the vertical distribution. Therefore it is reasonable to assume that for locations with large differences in column densities, like north of 50°N of orbits 1011 and 1023 or at 5°S – 35°N of orbits 278 and 397, the atmospheric water is more confined to the surface, even down to the lowest 2–3 km. Please note that the confinement to 2.5 km was arbitrarily chosen; another height value, like 1 km or 4 km, might deliver in some cases more accurate agreements between the LW and SW column densities. Yet important is the fact that the H<sub>2</sub>O molecules are confined to the boundary layer (lowest few kilometers) and do not reach the saturation level in the higher atmosphere.

A physical explanation for this phenomenon could be a fast supply of water vapour from the ground, e.g. by solar forcing, and an efficient mixing within the boundary layer due to temperature variations and turbulent eddies. The time scale for the eddy mixing is given by  $\tau = H(z)/\kappa(z)$  with the scale height  $H(z)$  (see equation 2.2 on page 21) and the eddy mixing coefficient  $\kappa(z)$  which are both a function of height (Titov et al. 1994). In the lower few kilometers of the atmosphere there is  $\kappa \approx 10^7 - 10^8 \text{ cm}^2 \text{ s}^{-1}$  while in the atmosphere above the boundary layer there is  $\kappa \approx 10^6 \text{ cm}^2 \text{ s}^{-1}$ . This yields timescales of ~1 day in the lowest few kilometers and of many days in the free atmosphere. Therefore the H<sub>2</sub>O molecules remain basically confined to the boundary layer and diffuse only rather slowly into greater altitudes. Finally, this theory is supported by the fact that orbits 1011 and 1023 occurred during the height of the northern summer and orbits 278 (longitude ~15°) and 397 (longitudes 10–13°) passed over Arabia Terra that was identified as a possible source for water vapour (cf. section 6.3).

# 7 Conclusions and outlook

## 7.1 Conclusions

In this work the available dataset of the SW channel of PFS was analysed in the  $2.6\ \mu\text{m}$  band to sound the atmosphere of Mars for water vapour. The applied technique of relative band depth fitting was explicitly described in chapter 5, including the explanation of the total error of 25–30% for each averaged spectrum. The results for the time between  $L_S=331^\circ$  of MY 26 and  $L_S=196^\circ$  of MY 27 are summarized in the following. Please note that after  $L_S=83^\circ$  only *Mars Express* was monitoring the atmosphere for water vapour in MY 27. Thus the PFS dataset is crucial for a continuous coverage of the  $\text{H}_2\text{O}$  cycle.

1. The goal of this work was to characterize the water cycle on Mars with great temporal and spatial resolution. In the covered period of a little more than the first half year of MY 27 an average column density of  $16.2\ \text{pr.}\ \mu\text{m}$  is found. This high amount is due to fact that the subliming polar cap of the northern summer dominates this time. In the relatively dry equinox season before  $L_S=70^\circ$  there is a mean water content of  $8.2\ \text{pr.}\ \mu\text{m}$  in the atmosphere. After that the northern seasonal polar cap retreats and the subliming ice enriches the atmosphere with water. The center of this  $\text{H}_2\text{O}$  increase is around  $75^\circ\text{N}$  and during  $L_S=90\text{--}130^\circ$  abundances of more than  $50\ \text{pr.}\ \mu\text{m}$  are measured in this region (maximum binned value  $68\ \text{pr.}\ \mu\text{m}$ ). Towards the equator there is a steep gradient of  $50\ \text{pr.}\ \mu\text{m}$  at  $\sim 70^\circ\text{N}$  latitude,  $20\text{--}40\ \text{pr.}\ \mu\text{m}$  between  $40^\circ\text{N}$  and  $60^\circ\text{N}$  and down to values of  $10\text{--}20\ \text{pr.}\ \mu\text{m}$  and lower southward of  $40^\circ\text{N}$ . Finally, after  $L_S=135^\circ$  the summer maximum quickly vanishes and a local peak of  $15\text{--}20\ \text{pr.}\ \mu\text{m}$  develops that moves towards the equator which is reached at approximately  $L_S=190^\circ$ . The driving force behind this movement is the atmospheric circulation. However, the net amount of transported water mass that arrives in the northern equatorial region (approximately  $1 \cdot 10^{14}\ \text{g}$ ) is much smaller than the amount released during the previous summer (about  $4 \cdot 10^{14}\ \text{g}$ ). Thus the bulk of the atmospheric water is deposited as ice on the ground or adsorbed by the soil.
2. The next major finding of this work is the fact that a diurnal variation is most likely present in the equinox season of  $L_S=335\text{--}70^\circ$  while no hints are found for the rest of the covered martian year. Around vernal equinox there is an increase of  $2\text{--}3\ \text{pr.}\ \mu\text{m}$  from morning to early afternoon between  $45^\circ\text{S}$  and  $40^\circ\text{N}$ . Because this increase is lower than previously reported diurnal changes it sets new upper limits to the adsorption capability of the regolith – if the effect is confirmed in the following martian year.

3. The quantitative comparison of results from PFS/SW and PFS/LW yielded the next important conclusion. This intercomparison of the water vapour retrievals from the thermal part of the IR spectrum with those of the near-infrared part permits an assessment of the vertical distribution of H<sub>2</sub>O. For the northern summer season the PFS/LW results northward of approximately 50°N are significantly lower than those of this work. While PFS/LW is only marginally dependent on the vertical distribution PFS/SW retrievals exhibit strong differences with changing vertical concentrations. Far better agreements between both findings (within the respective error bars) are achieved by deviating from an equally mixed H<sub>2</sub>O distribution up to the saturation level to a confinement of the water within the lower two or three kilometers above the local surface.

Interestingly, these better agreements are not only found for the northern summer high latitudes but also for the orbits crossing Arabia Terra (in the spring equinox season). A physical explanation for this phenomenon could be a rapid increase of H<sub>2</sub>O coming from the soil. This water vapour then undergoes quick vertical mixing by turbulent eddies within the boundary layer at timescales in the order of a day. However, at higher altitudes in the free atmosphere only slow mixing by diffusion takes place with timescales of many days. Therefore the water vapour stays confined to the lower few kilometers of the atmosphere.

4. The spatial distribution of water is characterized by two local maxima over Arabia Terra and the Tharsis highlands. There the column densities, scaled to 6.1 mbar, are by a factor of about two higher compared to the adjacent regions of the same latitudes. This detection confirms earlier measurements by TES and is best explained by a combination of both regolith–atmosphere interaction and atmospheric forcing by stationary planetary waves because neither of them can explain these wave-like features alone.
5. Another interesting phenomenon is that the north pole maximum between 65°N and 85°N exhibits an uneven longitudinal distribution that might be caused by inhomogeneous sublimation and deposition processes. A broad depletion of atmospheric water is found between 30°W and 10°E and a smaller one at 110–115°W whereas high concentrations of H<sub>2</sub>O are detected at 120–160°W, at 45–100°W and at 60–110°E. Physical reasons for these phenomena could be atmospheric circulation or specific properties of the soil that interacts with the atmosphere.
6. In the course of the spectral analysis the relative reflectance of the surface at a wavelength of 2.5 μm was mapped. Although it is not a quantitative measurement the agreement with the visible albedo is remarkably good. However, a correlation between the water abundances and the relative reflectance was not detected (between 30°S and 30°N). As the visible albedo depends on the fineness of the surface material (fine dust or coarse sand) this dataset does not support a dependence of the water vapour from the fineness of the soil.
7. In general, the observed abundances are in agreement with previous results of groundbased observations, of the orbiting *Viking*/MAWD and *MGS*/TES spectrometers, and results of simultaneous observations by SPICAM, OMEGA and PFS/LW

onboard *Mars Express* (within the respective errors of typically 20–30%). The occurring differences are on the one hand in the form of offsets to each other, like the SPICAM results being systematically lower than PFS/SW, and on the other hand the results scatter around each other. For example, in the orbit–for–orbit comparisons the (corrected) TES results are often higher than the PFS/SW ones but occasionally lower, as well. In this sense the OMEGA retrievals are in general agreement, too. The reason for the discrepancies are therefore the various applied retrieval techniques and instrumental behaviour. Yet it is important to see that also elder datasets are prone to these kind of problems and must therefore not be regarded as quantitatively precise. After all, only the intercomparison of datasets has triggered the reanalysis of the TES data that has caused its results to be lowered by approximately 70%.

8. Finally, the theoretical results of the EMCD general circulation model have so far been calibrated by the TES database. However, the consistently lower results of the *Mars Express* measurements demand an improvement of the model.

## 7.2 Future work and outlook

In the course of this work a reliable algorithm for PFS/SW data analysis in the 2.6  $\mu\text{m}$  water band has been developed. The processed available dataset covers the time from the start of the *Mars Express* mission until the mid of April 2005. After a large gap in data acquisition nominal operations of *MEX*/PFS were resumed in November 2005 ( $L_S=318^\circ$  of MY 27). At the moment the *MEX* mission is extended till end of November 2007 which marks the end of MY 28. Hence the analysis of this data will provide the possibility to compare subsequent martian years with the same instrument and the same analysis technique. This will allow the unambiguous identification of interannual variability and the confirmation of tentative measurements like the diurnal cycle. Moreover, in the current MY 28 also the southern summer is expected to be covered. This is particularly interesting for the correlation of atmospheric water with dust opacity, e.g. using measurements of the OMEGA spectrometer.

Yet the most promising aspect of PFS is the joint analysis of both water bands in the LW channel and the SW channel. If both retrieval algorithms (the one of this work and the one of Fouchet et al. (2006)) would be combined, the additional variable of the vertical  $\text{H}_2\text{O}$  distribution could be retrieved. However, this requires a thorough understanding of the atmospheric temperature profile as it influences the retrieved amounts of the LW channel most strongly. And of course other vertical distributions of  $\text{H}_2\text{O}$  molecules must be considered, including their impact on the retrievals, before definite conclusions can be drawn about the actual profile.

Finally, as for comparisons with other instruments, the newly arrived CRISM spectrometer onboard the American *Mars Reconnaissance Orbiter* started to deliver scientific data on a regular basis in November 2006. An intercomparison with these results will yield new insights into the behaviour of the instruments and especially of water vapour on Mars.



# A Appendix

## A.1 The definition of a martian year

The length of a martian year is 686.98 Earth days or 668.6 martian sols. The season of a martian year is given in solar longitude  $L_S$  that is defined as the positional angle between Mars and its vernal equinox point.

According to Clancy et al. (2000) the year 1 of the martian calendar, abbreviated MY 1, started on April 11, 1955. The various spacecraft did their observations in the following martian years: *Mariner 9* in MY 9–10, *Viking* in MY 12–13, *Pathfinder* in MY 23, *Mars Global Surveyor* in MY 24–26 and *Mars Express* starting in late MY 26. The year MY 27 began on March 6, 2004 and the current year MY 28 on January 22, 2006.

## A.2 The spectral bands of water vapour in the PFS range

Absorption in the infrared range for molecules that consist of two or more unequal atoms with a large dipole moment is taking place by vibrational and rotational excitation of the molecules (Goody 1964). The  $\nu_1$  vibration (for  $H_2O$  at  $2.74 \mu m / 3657 \text{ cm}^{-1}$ ) means symmetric stretching of the hydrogen atoms with respect to the oxygen atom,  $\nu_2$  ( $6.25 \mu m / 1595 \text{ cm}^{-1}$ ) means bending and the  $\nu_3$  vibration ( $2.66 \mu m / 3756 \text{ cm}^{-1}$ ) is caused by asymmetric stretching. Covered by PFS/SW there are two pronounced wavelength ranges in the reflected solar light containing water absorption lines, namely at  $1.87 \mu m$  ( $5350 \text{ cm}^{-1}$ ) and at  $2.6 \mu m$  ( $3850 \text{ cm}^{-1}$ ) used in this work. The first of these  $H_2O$  bands is a blend of vibrational bands; the second one is caused by a combination of the  $\nu_1$  and  $\nu_3$  bands. Additional bands in SW which are all combinations, overtones and upper state bands are located for example at  $1.38 \mu m / 7250 \text{ cm}^{-1}$ ,  $3.1 \mu m / 3162 \text{ cm}^{-1}$  ( $2\nu_2$ ; first overtone of  $\nu_2$ ) and  $4.8 \mu m / 2062 \text{ cm}^{-1}$ .

The relevant bands in the longwavelength channel are the  $\nu_2$  vibrational band at  $6.25 \mu m$  and a purely rotational band at  $20\text{--}45 \mu m$  ( $250\text{--}500 \text{ cm}^{-1}$ ), close to the  $\nu_2$  band of  $CO_2$ , which is used for the PFS/LW water retrievals.

## A.3 The European Mars Climate Database (EMCD)

After using the barometric formula for calculating the surface pressure and an altitude-dependent surface temperature for the first crude fittings the European Mars Climate

Database, version 3.1, was included for the generation of synthetic spectra. This numerical general circulation model incorporates the diurnal and seasonal changes of the martian atmosphere and delivers – among other parameters – a pressure and temperature profile for each grid-point on the surface for all points of time. The temporal resolution is 1/12 sol and 30° of  $L_S$ . The spatial resolution is a  $5^\circ \times 5^\circ$  longitude-latitude grid with 32 levels ranging from the zerolevel of a defined Mars geoid to an altitude of 120 km whereas the altitude resolution improves towards the zerolevel. In the retrieval algorithm the adjustment of the pressure profile to the actual surface altitude (taken from the MOLA  $1/4^\circ \times 1/4^\circ$  database) is done by the barometric formula while the temperature profile is simply shifted to the topographic zero point. The model also allows to select five scenarios of dust opacities spanning from a clear atmosphere to dust storms. For this work always the normal scenario with average dust conditions was used which relies on the TES measurements of MY 24. Lastly, a detailed description of the model is given by Lewis et al. (1999) and Forget et al. (1999).

With the availability of the upgraded EMCD 4.1 (Forget et al. 2006b) this climate model was included into the calculations. The main advantages are more accurate temperature and pressure profiles that start from the topographic MOLA altitude and a higher grid resolution of  $5.625^\circ \times 3.75^\circ$  in longitude and latitude. Furthermore, the altitude range now extends to 250 km, the seasonal results are interpolated and estimations for the following constituents and parameters are provided: mixing ratios of  $\text{CO}_2$ ,  $\text{N}_2$ ,  $\text{O}_2$ ,  $\text{CO}$ ,  $\text{H}_2\text{O}$ ,  $\text{O}_3$ , amounts of water ice and dust, incident and reflected solar flux.

## A.4 Measurement quantities of $\text{H}_2\text{O}$

The gas amount of water vapour in air can be described in two ways: either in terms of the mixing ratio per volume  $f$ , given in parts-per-million (ppm) or in terms of the depth of a water layer with the equal mass as the one of an integrated  $\text{H}_2\text{O}$  gas column per unit area reaching to an altitude  $z$ . This depth  $d_w$  can be calculated as given in Bohren and Albrecht (1998):

$$d_w = \frac{1}{\rho_w} \cdot \int_{\infty}^0 \rho_g(z) dz = \frac{1}{\rho_w R} \cdot \int_{\infty}^0 \frac{p_g(z)}{T(z)} dz \quad (\text{A.1})$$

Here  $\rho_w$  is the mass density of liquid water,  $\rho_g$  that of gaseous water (with  $\rho_g = f \cdot \rho_{\text{air,dry}}$ ),  $R$  the gas constant for water vapour,  $p_g$  the  $\text{H}_2\text{O}$  pressure and  $T$  the ambient temperature. The integration is from the top of the atmosphere to the ground. An example is shown in figure A.1, showing the profiles of temperature as calculated by EMCD,  $\text{H}_2\text{O}$  pressure, mixing ratio and particle density (per  $\text{cm}^2$ ) for the conditions of spectra 167–181 of orbit 37. In case of saturation conditions the water vapour pressure naturally follows the saturation pressure (dotted line in upper right panel) that is given by equation 5.8 on page 58; if it is lower than the saturation pressure the  $\text{H}_2\text{O}$  pressure depends only on the given mixing ratio (solid line below  $\sim 20$  km in upper right panel).

The measuring unit for this so-called column density are precipitable micrometers (pr.  $\mu\text{m}$ ) where 1 pr.  $\mu\text{m} = 1 \text{ g/m}^2$  for  $\text{H}_2\text{O}$  and it is the naturally retrieved quantity in IR spectral analysis. For example, if on Earth the entire water held by the atmosphere would condense, there would be a water layer of about 25 mm thickness in the annual mean.

It needs to be mentioned that column density can in principle also be calculated using pressure coordinates:

$$d_w = \frac{1}{g} \frac{m_w}{\langle M \rangle} \cdot \int_{p_\infty}^{p_0} f(p) dp$$

where  $m_w$  is the molecular weight of water vapour (18.0153 g/mol),  $\langle M \rangle$  is the mean molecular weight of martian atmosphere (43.44 g/mol),  $p_0$  the surface pressure,  $p_\infty$  the pressure at the upper limit of the atmosphere that is considered to be zero and  $f(p)$  the H<sub>2</sub>O mixing ratio in pressure coordinates.

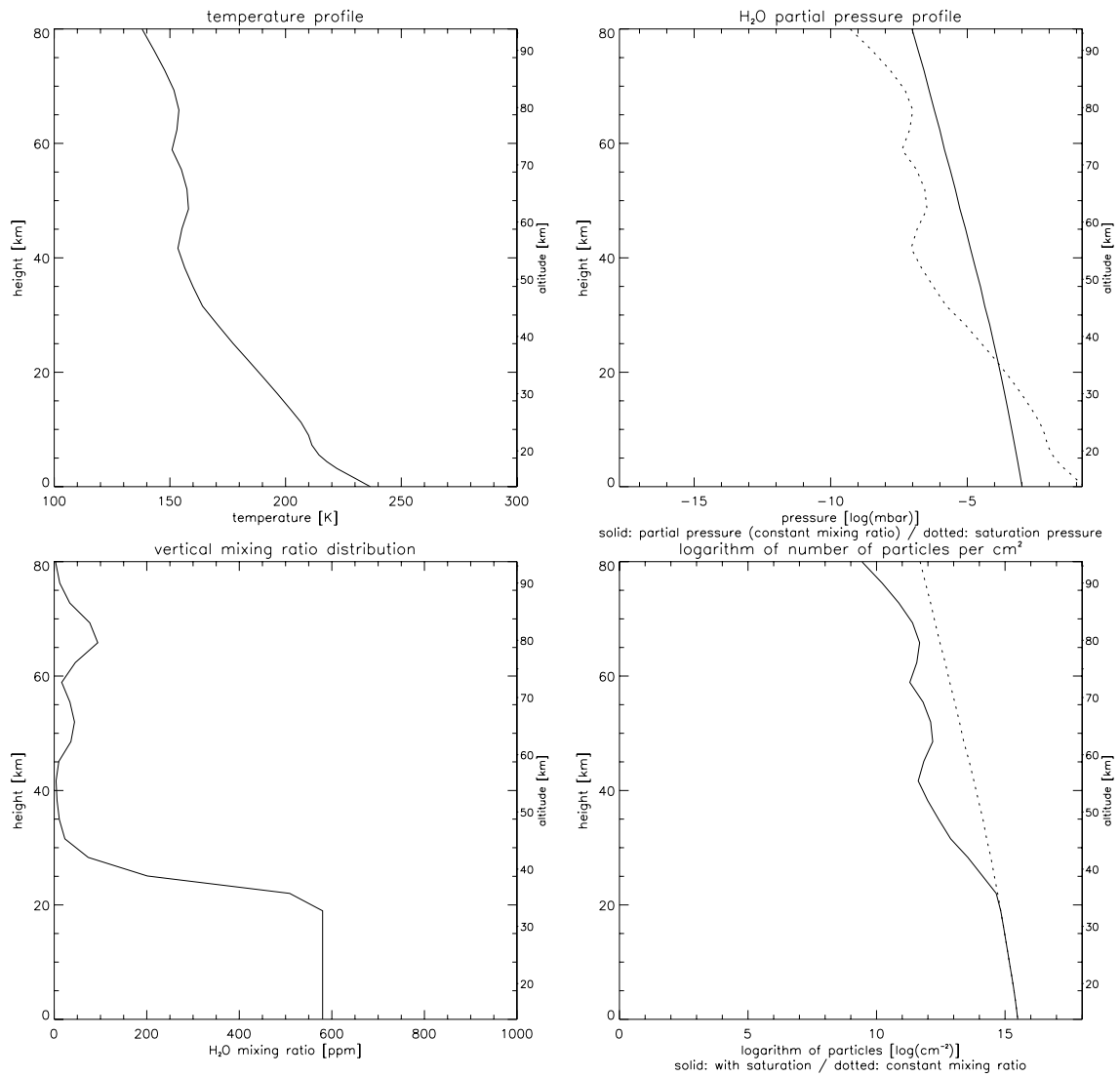


Figure A.1: For spectra 167–181 of orbit 37 there are the following profiles, plotted versus height over the surface (right y-axis) and MOLA altitude (left y-axis). Upper left: temperature profile; upper right: H<sub>2</sub>O pressure (dotted: with saturation; solid: no saturation); lower left: mixing ratio profile for saturation conditions; particle area density (solid: with saturation; dotted: no saturation).

## A.5 Hamming apodization

Apodization means the smoothing of a mathematical function by multiplication with a window function in order to reduce unwanted contributions outside of that window. In case of PFS the Fourier spectrum is multiplied by a so-called Hamming window function to remove higher order contributions at the edges of the interferogram. This results in a smoother frequency spectrum without high frequency noise and with reduced overshooting. The Hamming function  $A(\delta)$  is given by

$$A(\delta) = \alpha + (1 - \alpha) \cdot \cos\left(\frac{\pi \cdot \delta}{\delta_{max}}\right) \quad (\text{A.2})$$

where  $\delta$  is the interferogram path difference,  $\delta_{max}$  its maximum and  $\alpha$  a factor, set to 0.53856.

## A.6 Radiometric terminology

In radiometry there are several different terms to describe the energy transported by electromagnetic waves. The basic quantity is the flux meaning the energy transported per second [erg/s]. Depending on the way of measurement there are several notions that contain the term "spectral" because only discrete energies are considered:

- 1) flux per solid angle and wavenumber: spectral intensity [erg/s/sr/cm<sup>-1</sup>]
- 2) flux per area and wavenumber: spectral irradiance [erg/s/m<sup>2</sup>/cm<sup>-1</sup>]
- 3) flux per solid angle, per area and per wavenumber: spectral radiance [erg/s/sr/m<sup>2</sup>/cm<sup>-1</sup>]

# Bibliography

- Banfield, D., Conrath, B. J., Smith, M. D., Christensen, P. R., and Wilson, R. J. (2003). Forced waves in the martian atmosphere from MGS TES nadir data. *Icarus*, 161:319–345.
- Barker, E. S. (1976). Martian atmospheric water vapor observations - 1972-74 apparition. *Icarus*, 28:247–268.
- Barker, E. S., Schorn, R. A., Woszczyk, A., Tull, R. G., and Little, S. J. (1970). Mars: Detection of atmospheric water vapor during the southern hemisphere spring and summer season. *Science*, 170:1308–1310.
- Barnes, J. R. (1980). Time spectral analysis of midlatitude disturbances in the Martian atmosphere. *Journal of Atmospheric Sciences*, 37:2002–2015.
- Basilevsky, A. T., Rodin, A. V., Raitala, J., Neukum, G., Werner, S., Kozyrev, A. S., Sanin, A. B., Mitrofanov, I. G., Head, J. W., Boynton, W., and Saunders, R. S. (2006). Search for causes of the low epithermal neutron flux anomaly in the Arabia Terra region (Mars). *Solar System Research*, 40:355–374.
- Bauer, S. J. (2001). *Die Planetenatmosphären*, page 605 ff. Lehrbuch der Experimentalphysik - Erde und Planeten.
- Bibring, J.-P., Langevin, Y., Gendrin, A., Gondet, B., Poulet, F., Berthé, M., Soufflot, A., Arvidson, R., Mangold, N., Mustard, J., and Drossart, P. (2005). Mars Surface Diversity as Revealed by the OMEGA/Mars Express Observations. *Science*, 307:1576–1581.
- Bibring, J.-P., Langevin, Y., Mustard, J. F., Poulet, F., Arvidson, R., Gendrin, A., Gondet, B., Mangold, N., Pinet, P., and Forget, F. (2006). Global Mineralogical and Aqueous Mars History Derived from OMEGA/Mars Express Data. *Science*, 312:400–404.
- Bibring, J.-P., Langevin, Y., Poulet, F., Gendrin, A., Gondet, B., Berthé, M., Soufflot, A., Drossart, P., Combes, M., Bellucci, G., Moroz, V., Mangold, N., Schmitt, B., and OMEGA team, t. (2004). Perennial water ice identified in the south polar cap of Mars. *Nature*, 428:627–630.
- Biver, N., Lecacheux, A., Encrenaz, T., Lellouch, E., Baron, P., Crovisier, J., Frisk, U., Hjalmarson, Å., Olberg, M., Sandqvist, A., and Kwok, S. (2005). Wide-band observations of the 557 GHz water line in Mars with Odin. *A&A*, 435:765–772.

- Bohren, C. F. and Albrecht, B. A. (1998). *Atmospheric Thermodynamics*, page 181 ff. Oxford University Press.
- Böttger, H. M., Lewis, S. R., Read, P. L., and Forget, F. (2004). The effect of a global dust storm on simulations of the Martian water cycle. *Geophys. Res. Lett.*, 31:22702.
- Böttger, H. M., Lewis, S. R., Read, P. L., and Forget, F. (2005). The effects of the martian regolith on GCM water cycle simulations. *Icarus*, 177:174–189.
- Boynton, W. V., Feldman, W. C., Squyres, S. W., Prettyman, T. H., Brückner, J., Evans, L. G., Reedy, R. C., Starr, R., Arnold, J. R., Drake, D. M., Englert, P. A. J., Metzger, A. E., Mitrofanov, I., Trombka, J. I., d’Uston, C., Wänke, H., Gasnault, O., Hamara, D. K., Janes, D. M., Marcialis, R. L., Maurice, S., Mikheeva, I., Taylor, G. J., Tokar, R., and Shinohara, C. (2002). Distribution of Hydrogen in the Near Surface of Mars: Evidence for Subsurface Ice Deposits. *Science*, 297:81–85.
- Burgdorf, M. J., Encrenaz, T., Lellouch, E., Feuchtgruber, H., Davis, G. R., Swinyard, B. M., de Graauw, T., Morris, P. W., Sidher, S. D., Griffin, M. J., Forget, F., and Lim, T. L. (2000). ISO Observations of Mars: An Estimate of the Water Vapor Vertical Distribution and the Surface Emissivity. *Icarus*, 145:79–90.
- Christensen, P. R., Bandfield, J. L., Bell, J. F., Gorelick, N., Hamilton, V. E., Ivanov, A., Jakosky, B. M., Kieffer, H. H., Lane, M. D., Malin, M. C., McConnochie, T., McEwen, A. S., McSween, H. Y., Mehall, G. L., Moersch, J. E., Neelson, K. H., Rice, J. W., Richardson, M. I., Ruff, S. W., Smith, M. D., Titus, T. N., and Wyatt, M. B. (2003). Morphology and Composition of the Surface of Mars: Mars Odyssey THEMIS Results. *Science*, 300:2056–2061.
- Clancy, R. T., Grossman, A. W., and Muhleman, D. O. (1992). Mapping Mars water vapor with the Very Large Array. *Icarus*, 100:48–59.
- Clancy, R. T., Grossman, A. W., Wolff, M. J., James, P. B., Rudy, D. J., Billawala, Y. N., Sandor, B. J., Lee, S. W., and Muhleman, D. O. (1996). Water vapor saturation at low altitudes around Mars aphelion: A key to Mars climate? *Icarus*, 122:36–62.
- Clancy, R. T., Sandor, B. J., Wolff, M. J., Christensen, P. R., Smith, M. D., Pearl, J. C., Conrath, B. J., and Wilson, R. J. (2000). An intercomparison of ground-based millimeter, MGS TES, and Viking atmospheric temperature measurements: Seasonal and interannual variability of temperatures and dust loading in the global Mars atmosphere. *J. Geophys. Res.*, 105:9553–9572.
- Comolli, L. and Saggini, B. (2005). Evaluation of the sensitivity to mechanical vibrations of an IR Fourier spectrometer. *Review of Scientific Instruments*, 76(12):123112.
- Conrath, B., Curran, R., Hanel, R., Kunde, V., Maguire, W., Pearl, J., Pirraglia, J., and Welker, J. (1973). Atmospheric and surface properties of Mars obtained by infrared spectroscopy on Mariner 9. *J. Geophys. Res.*, 78:4267–4278.

- de Graauw, T., Caux, E., Guesten, R., Helmich, F., Pearson, J., Phillips, T. G., Schieder, R., Tielens, X., Saraceno, P., Stutzki, J., Wafelbakker, C. K., and Whyborn, N. D. (2005). The Herschel-Heterodyne Instrument for the Far-Infrared (HIFI). *Bulletin of the American Astronomical Society*, 37:1219.
- Encrenaz, T., Bézard, B., Greathouse, T., Holmes, S., Richter, M., Nuccitelli, D., Lacy, J., Lebonnois, S., Lefèvre, F., Atreya, S., Wong, A. S., Owen, T., and Forget, F. (2006). Ground-based high-resolution IR spectroscopy of Mars: H<sub>2</sub>O and H<sub>2</sub>O<sub>2</sub> mapping, search for CH<sub>4</sub>, and determination of CO<sub>2</sub> isotopic ratios. In Forget, F., Lopez-Valverde, M. A., Desjean, M. C., Huot, J. P., Lefevre, F., Lebonnois, S., Lewis, S. R., Millour, E., Read, P. L., and Wilson, R. J., editors, *Mars Atmosphere Modelling and Observations*, pages 511.
- Encrenaz, T., Bézard, B., Owen, T., Lebonnois, S., Lefèvre, F., Greathouse, T., Richter, M., Lacy, J., Atreya, S., Wong, A. S., and Forget, F. (2005a). Infrared imaging spectroscopy of Mars: H<sub>2</sub>O mapping and determination of CO<sub>2</sub> isotopic ratios. *Icarus*, 179:43–54.
- Encrenaz, T., Lellouch, E., Atreya, S. K., and Wong, A. S. (2004). Detectability of minor constituents in the martian atmosphere by infrared and submillimeter spectroscopy. *Planet. Space Sci.*, 52:1023–1037.
- Encrenaz, T., Lellouch, E., Cernicharo, J., Paubert, G., and Gulkis, S. (1995). A tentative detection of the 183-GHz water vapor line in the martian atmosphere: Constraints upon the H<sub>2</sub>O abundance and vertical distribution. *Icarus*, 113:110–118.
- Encrenaz, T., Melchiorri, R., Fouchet, T., Drossart, P., Lellouch, E., Gondet, B., Bibring, J.-P., Langevin, Y., Titov, D., Ignatiev, N., and Forget, F. (2005b). A mapping of martian water sublimation during early northern summer using OMEGA/Mars Express. *A&A*, 441:L9–L12.
- Fedorova, A., Korablev, O., Bertaux, J.-L., Rodin, A., Kiselev, A., and Perrier, S. (2006). Mars water vapor abundance from SPICAM IR spectrometer: Seasonal and geographic distributions. *Journal of Geophysical Research (Planets)*, 111:9.
- Fedorova, A. A., Rodin, A. V., and Baklanova, I. V. (2004). MAWD observations revisited: seasonal behavior of water vapor in the martian atmosphere. *Icarus*, 171:54–67.
- Feldman, W. C., Prettyman, T. H., Maurice, S., Plaut, J. J., Bish, D. L., Vaniman, D. T., Mellon, M. T., Metzger, A. E., Squyres, S. W., Karunatillake, S., Boynton, W. V., Elphic, R. C., Funsten, H. O., Lawrence, D. J., and Tokar, R. L. (2004). Global distribution of near-surface hydrogen on Mars. *Journal of Geophysical Research (Planets)*, 109:9006.
- Fiorenza, C. and Formisano, V. (2005). A solar spectrum for PFS data analysis. *Planet. Space Sci.*, 53:1009–1016.
- Forget, F., Haberle, R. M., Montmessin, F., Levrard, B., and Head, J. W. (2006a). Formation of Glaciers on Mars by Atmospheric Precipitation at High Obliquity. *Science*, 311:368–371.

- Forget, F., Hourdin, F., Fournier, R., Hourdin, C., Talagrand, O., Collins, M., Lewis, S. R., Read, P. L., and Huot, J.-P. (1999). Improved general circulation models of the Martian atmosphere from the surface to above 80 km. *J. Geophys. Res.*, 104:24155–24176.
- Forget, F., Millour, E., Lebonnois, S., Montabone, L., Dassas, K., Lewis, S. R., Read, P. L., López-Valverde, M. A., González-Galindo, F., Montmessin, F., Lefèvre, F., Desjean, M.-C., and Huot, J.-P. (2006b). The new Mars climate database. In Forget, F., Lopez-Valverde, M. A., Desjean, M. C., Huot, J. P., Lefevre, F., Lebonnois, S., Lewis, S. R., Millour, E., Read, P. L., and Wilson, R. J., editors, *Mars Atmosphere Modelling and Observations*, pages 128.
- Formisano, V., Angrilli, F., Arnold, G., Atreya, S., Bianchini, G., Biondi, D., Blanco, A., Blecka, M. I., Coradini, A., Colangeli, L., Ekonomov, A., Esposito, F., Fonti, S., Giuranna, M., Grassi, D., Gnedykh, V., Grigoriev, A., Hansen, G., Hirsh, H., Khatuntsev, I., Kiselev, A., Ignatiev, N., Jurewicz, A., Lellouch, E., Lopez Moreno, J., Marten, A., Mattana, A., Maturilli, A., Mencarelli, E., Michalska, M., Moroz, V., Moshkin, B., Nespoli, F., Nikolsky, Y., Orfei, R., Orleanski, P., Orofino, V., Palomba, E., Patsaev, D., Piccioni, G., Rataj, M., Rodrigo, R., Rodriguez, J., Rossi, M., Saggin, B., Titov, D., and Zasova, L. (2005). The Planetary Fourier Spectrometer (PFS) onboard the European Mars Express mission. *Planet. Space Sci.*, 53:963–974.
- Formisano, V., Grassi, D., Ignatiev, N. I., and Zasova, L. (2001). IRIS Mariner 9 data revisited: water and dust daily cycles. *Planet. Space Sci.*, 49:1331–1346.
- Formisano, V., Grassi, D., Orfei, R., Biondi, D., Mencarelli, E., Mattana, A., Nespoli, F., Maturilli, A., Giuranna, M., Rossi, M., Maggi, M., Baldetti, P., Chionchio, G., Saggin, B., Angrilli, F., Bianchini, G., Piccioni, G., Di Lellis, A., Cerroni, P., Capaccioni, F., Capria, M. T., Coradini, A., Fonti, S., Orofino, V., Blanco, A., Colangeli, L., Palomba, E., Esposito, F., Patsaev, D., Moroz, V., Zasova, L., Ignatiev, N., Khatuntsev, I., Moshkin, B., Ekonomov, A., Grigoriev, A., Nechaev, V., Kiselev, A., Nikolsky, Y., Gnedykh, V., Titov, D., Orleanski, P., Rataj, M., Malgoska, M., Jurewicz, A., Blecka, M. I., Hirsh, H., Arnold, G., Lellouch, E., Marten, A., Encrenaz, T., Lopez Moreno, J., Atreya, S., and Gobbi, P. (2004). *The Planetary Fourier Spectrometer (PFS) for Mars Express*. ESA SP 1240.
- Fouchet, T., Lellouch, E., Ignatiev, N. I., Titov, D., Tschimmel, M., Formisano, V., Giuranna, M., Maturilli, A., and Encrenaz, T. (2007). Martian water vapor: Mars Express PFS/LW observations. *Icarus*, *accepted*.
- Gamache, R. R., Neshyba, S. P., Plateaux, J. J., Barbe, A., Régalia, L., and Pollack, J. B. (1995). CO<sub>2</sub>-broadening of water-vapor lines. *Journal of Molecular Spectroscopy*, 170:131–151.
- Giuranna, M., Formisano, V., Biondi, D., Ekonomov, A., Fonti, S., Grassi, D., Hirsch, H., Khatuntsev, I., Ignatiev, N., Malgoska, M., Mattana, A., Maturilli, A., Mencarelli, E., Nespoli, F., Orfei, R., Orleanski, P., Piccioni, G., Rataj, M., Saggin, B., and Zasova, L. (2005). Calibration of the Planetary Fourier Spectrometer long wavelength channel. *Planet. Space Sci.*, 53:993–1007.

- Goody, R. M. (1964). *Atmospheric Radiation: Theoretical basis*, pages 179–193. Oxford University Press.
- Grassi, D., Ignatiev, N. I., Zasova, L. V., Maturilli, A., Formisano, V., Bianchini, G. A., and Giuranna, M. (2005). Methods for the analysis of data from the Planetary Fourier Spectrometer on the Mars Express Mission. *Planet. Space Sci.*, 53:1017–1034.
- Gurwell, M. A., Bergin, E. A., Melnick, G. J., Ashby, M. L. N., Chin, G., Erickson, N. R., Goldsmith, P. F., Harwit, M., Howe, J. E., Kleiner, S. C., Koch, D. G., Neufeld, D. A., Patten, B. M., Plume, R., Schieder, R., Snell, R. L., Stauffer, J. R., Tolls, V., Wang, Z., Winnewisser, G., and Zhang, Y. F. (2000). Submillimeter Wave Astronomy Satellite Observations of the Martian Atmosphere: Temperature and Vertical Distribution of Water Vapor. *ApJ*, 539:L143–L146.
- Gurwell, M. A., Bergin, E. A., Melnick, G. J., and Tolls, V. (2005). Mars surface and atmospheric temperature during the 2001 global dust storm. *Icarus*, 175:23–31.
- Hale, A. S., Tamppari, L. K., Christensen, P. R., Smith, M. D., Bass, D., Qu, Z., and Pearl, J. C. (2005). Water Ice Clouds in the Martian Atmosphere: A View from MGS TES. In Mackwell, S. and Stansbery, E., editors, *36th Annual Lunar and Planetary Science Conference*, pages 1083.
- Hanel, R., Conrath, B., Hovis, W., Kunde, V., Lowman, P., Maguire, W., Pearl, J., Pirraglia, J., Prabhakara, C., Schlachman, B., Levin, G., Straat, P., and Burke, T. (1972). Investigation of the Martian Environment by Infrared Spectroscopy on Mariner 9 (A 5. 2). *Icarus*, 17:423.
- Hanel, R. A., Conrath, B. J., Jennings, D. E., and Samuelson, R. E. (2003). *Exploration of the Solar System by Infrared Remote Sensing: Second Edition*. Exploration of the Solar System by Infrared Remote Sensing, by R. A. Hanel and B. J. Conrath and D. E. Jennings and R. E. Samuelson, pp. 534. ISBN 0521818974. Cambridge, UK: Cambridge University Press, April 2003.
- Hansen, G., Giuranna, M., Formisano, V., Fonti, S., Grassi, D., Hirsh, H., Ignatiev, N., Maturilli, A., Orleanski, P., Piccioni, G., Rataj, M., Saggin, B., and Zasova, L. (2005). PFS-MEX observation of ices in the residual south polar cap of Mars. *Planet. Space Sci.*, 53:1089–1095.
- Haus, R. and Titov, D. V. (2000). PFS on Mars Express: preparing the analysis of infrared spectra to be measured by the Planetary Fourier Spectrometer. *Planet. Space Sci.*, 48:1357–1376.
- Head, J. W., Neukum, G., Jaumann, R., Hiesinger, H., Hauber, E., Carr, M., Masson, P., Foing, B., Hoffmann, H., Kreslavsky, M., Werner, S., Milkovich, S., van Gasselt, S., and Co-Investigator Team, T. H. (2005). Tropical to mid-latitude snow and ice accumulation, flow and glaciation on Mars. *Nature*, 434:346–351.
- Houghton, J. (2002). *The physics of Atmospheres*. Cambridge University Press.

- Hunten, D. M., Sprague, A. L., and Doose, L. R. (2000). Correction for Dust Opacity of Martian Atmospheric Water Vapor Abundances. *Icarus*, 147:42–48.
- Ignatiev, N. I., Grassi, D., and Zasova, L. V. (2005). Planetary Fourier spectrometer data analysis: Fast radiative transfer models. *Planet. Space Sci.*, 53:1035–1042.
- Ignatiev, N. I., Zasova, L. V., Formisano, V., Grassi, D., and Maturilli, A. (2002). Water vapour abundance in Martian atmosphere from revised Mariner 9 IRIS data. *Advances in Space Research*, 29:157–162.
- Jakosky, B. M. and Barker, E. S. (1984). Comparison of ground-based and Viking Orbiter measurements of Martian water vapor - Variability of the seasonal cycle. *Icarus*, 57:322–334.
- Jakosky, B. M. and Farmer, C. B. (1982). The seasonal and global behavior of water vapor in the Mars atmosphere - Complete global results of the Viking atmospheric water detector experiment. *J. Geophys. Res.*, 87:2999–3019.
- Jakosky, B. M. and Haberle, R. M. (1992). *The seasonal behavior of water on Mars*, pages 969–1016. Mars.
- Jakosky, B. M., Mellon, M. T., Varnes, E. S., Feldman, W. C., Boynton, W. V., and Haberle, R. M. (2005). Mars low-latitude neutron distribution: Possible remnant near-surface water ice and a mechanism for its recent emplacement. *Icarus*, 175:58–67.
- Jakosky, B. M., Zurek, R. W., and La Pointe, M. R. (1988). The observed day-to-day variability of Mars atmospheric water vapor. *Icarus*, 73:80–90.
- James, P. B., Hansen, G. B., and Titus, T. N. (2005). The carbon dioxide cycle. *Advances in Space Research*, 35:14–20.
- James, P. B., Kieffer, H. H., and Paige, D. A. (1992). *The seasonal cycle of carbon dioxide on Mars*, pages 934–968. Mars.
- Jänchen, J., Bish, D. L., Möhlmann, D. T. F., and Stach, H. (2006). Investigation of the water sorption properties of Mars-relevant micro- and mesoporous minerals. *Icarus*, 180:353–358.
- Kahn, R. A., Martin, T. Z., Zurek, R. W., and Lee, S. W. (1992). *The Martian dust cycle*, pages 1017–1053. Mars.
- Kaplan, L. D., Münch, G., and Spinrad, H. (1964). An Analysis of the Spectrum of Mars. *ApJ*, 139:1.
- Kossacki, K. J., Markiewicz, W. J., Smith, M. D., Page, D., and Murray, J. (2006). Possible remnants of a frozen mud lake in southern Elysium, Mars. *Icarus*, 181:363–374.
- Krasnopol'skii, V. A., Korablev, O. I., Moroz, V. I., Krysko, A. A., Blamont, J. E., and Chassefiere, E. (1991). Infrared solar occultation sounding of the Martian atmosphere by the Phobos spacecraft. *Icarus*, 94:32–44.

- Krasnopolsky, V. A. (2006). Photochemistry of the martian atmosphere: Seasonal, latitudinal, and diurnal variations. *Icarus*, 185:153–170.
- Lammer, H., Kolb, C., Penz, T., Amerstorfer, U. V., Biernat, H. K., and Bodiselitsch, B. (2003). Estimation of the past and present Martian water-ice reservoirs by isotopic constraints on exchange between the atmosphere and the surface. *International Journal of Astrobiology*, 2:195–202.
- Laskar, J., Levrard, B., and Mustard, J. F. (2002). Orbital forcing of the martian polar layered deposits. *Nature*, 419:375–377.
- Lellouch, E., Encrenaz, T., de Graauw, T., Erard, S., Morris, P., Crovisier, J., Feuchtgruber, H., Girard, T., and Burgdorf, M. (2000). The 2.4–45 $\mu$ m spectrum of Mars observed with the infrared space observatory. *Planet. Space Sci.*, 48:1393–1405.
- Lewis, S. R., Collins, M., Read, P. L., Forget, F., Hourdin, F., Fournier, R., Hourdin, C., Talagrand, O., and Huot, J.-P. (1999). A climate database for Mars. *J. Geophys. Res.*, 104:24177–24194.
- Maturilli, A., Formisano, V., and Grassi, D. (2002). A software simulator for the Planetary Fourier Spectrometer on board the Mars express mission. *Advances in Space Research*, 29:169–174.
- Mauersberger, K. and Krankowsky, D. (2003). Vapor pressure above ice at temperatures below 170 K. *Geophys. Res. Lett.*, 30:21–1.
- Melchiorri, R., Encrenaz, T., Fouchet, T., Drossart, P., Lellouch, E., Gondet, B., Bibring, J. P., Langevin, Y., Schmitt, B., Titov, D., and Ignatiev, N. (2006). Water vapor mapping on Mars using OMEGA/Mars Express. *Planet. Space Sci.*, *in press*.
- Mitrofanov, I. G., Litvak, M. L., Kozyrev, A. S., Sanin, A. B., Tret'yakov, V. I., Grin'kov, V. Y., Boynton, W. V., Shinohara, C., Hamara, D., and Saunders, R. S. (2004). Soil Water Content on Mars as Estimated from Neutron Measurements by the HEND Instrument Onboard the 2001 Mars Odyssey Spacecraft. *Solar System Research*, 38:253–257.
- Möhlmann, D. T. F. (2004). Water in the upper martian surface at mid- and low-latitudes: presence, state, and consequences. *Icarus*, 168:318–323.
- Montmessin, F., Forget, F., Rannou, P., Cabane, M., and Haberle, R. M. (2004). Origin and role of water ice clouds in the Martian water cycle as inferred from a general circulation model. *Journal of Geophysical Research (Planets)*, 109:10004.
- Moroz, V. I. and Ksanfomaliti, L. V. (1972). Preliminary Results of Astrophysical Observations of Mars from Mars-3 (A 5. 1). *Icarus*, 17:408.
- Moroz, V. I. and Nadzhip, A. E. (1975). Water vapor in the Martian atmosphere from measurements onboard the Mars-3 interplanetary probe. *Cosmic Research*, 13:738–752.

- Novak, R. E., Mumma, M. J., DiSanti, M. A., Russo, N. D., and Magee-Sauer, K. (2002). Mapping of Ozone and Water in the Atmosphere of Mars near the 1997 Aphelion. *Icarus*, 158:14–23.
- Perrier, S., Bertaux, J. L., Lefèvre, F., Lebonnois, S., Korablev, O., Fedorova, A., and Montmessin, F. (2006). Global distribution of total ozone on Mars from SPICAM/MEX UV measurements. *Journal of Geophysical Research (Planets)*, 111:9.
- Putzig, N. E., Mellon, M. T., Kretke, K. A., and Arvidson, R. E. (2005). Global thermal inertia and surface properties of Mars from the MGS mapping mission. *Icarus*, 173:325–341.
- Read, P. and Lewis, S. (2004). *The Martian Climate Revisited*. Springer.
- Read, P. L., McCleese, D. J., Schofield, J. T., Taylor, F. W., and Calcutt, S. B. (2006). Remote sensing studies of the current martian climate by the Mars climate sounder on the Mars Reconnaissance Orbiter. In Forget, F., Lopez-Valverde, M. A., Desjean, M. C., Huot, J. P., Lefevre, F., Lebonnois, S., Lewis, S. R., Millour, E., Read, P. L., and Wilson, R. J., editors, *Mars Atmosphere Modelling and Observations*, pages 711.
- Rizk, B., Wells, W. K., Hunten, D. M., Stoker, C. R., Freedman, R. S., Roush, T., Pollack, J. B., and Haberle, R. M. (1991). Meridional Martian water abundance profiles during the 1988-1989 season. *Icarus*, 90:205–213.
- Rodin, A. V., Korablev, O. I., and Moroz, V. I. (1997). Vertical Distribution of Water in the Near-Equatorial Troposphere of Mars: Water Vapor and Clouds. *Icarus*, 125:212–229.
- Rosenqvist, J., Drossart, P., Combes, M., Encrenaz, T., Lellouch, E., Bibring, J. P., Erard, S., Langevin, Y., and Chassefière, E. (1992). Minor constituents in the Martian atmosphere from the ISM/Phobos experiment. *Icarus*, 98:254–270.
- Rothman, L. S., Jacquemart, D., Barbe, A., Benner, D. C., Birk, M., Brown, L. R., Carleer, M. R., Chackerian, C., Chance, K., Coudert, L. H., Dana, V., Devi, V. M., Flaud, J. M., Gamache, R. R., Goldman, A., Hartmann, J. M., Jucks, K. W., Maki, A. G., Mandin, J. Y., Massie, S. T., Orphal, J., Perrin, A., Rinsland, C. P., Smith, M. A. H., Tennyson, J., Tolchenov, R. N., Toth, R. A., Vander Auwera, J., Varanasi, P., and Wagner, G. (2005). The HITRAN 2004 molecular spectroscopic database. *Journal of Quantitative Spectroscopy and Radiative Transfer*, 96:139–204.
- Ryan, J. A., Sharman, R. D., and Lucich, R. D. (1982). Mars water vapor, near-surface. *J. Geophys. Res.*, 87:7279–7284.
- Salby, M. (1996). *Fundamentals of atmospheric physics*. Academic Press, Inc.
- Schorn, R. A., Spinrad, H., Moore, R. C., Smith, H. J., and Giver, L. P. (1967). High-Dispersion Spectroscopic Observations of Mars. II. The Water-Vapor Variations. *ApJ*, 147:743.
- Smith, M. D. (2002). The annual cycle of water vapor on Mars as observed by the Thermal Emission Spectrometer. *Journal of Geophysical Research (Planets)*, 107:25–1.

- Smith, M. D. (2004). Interannual variability in TES atmospheric observations of Mars during 1999-2003. *Icarus*, 167:148–165.
- Spinrad, H., Münch, G., and Kaplan, L. D. (1963). Letter to the Editor: the Detection of Water Vapor on Mars. *ApJ*, 137:1319.
- Sprague, A. L., Hunten, D. M., Doose, L. R., and Hill, R. E. (2003). Mars atmospheric water vapor abundance: 1996-1997. *Icarus*, 163:88–101.
- Sprague, A. L., Hunten, D. M., Doose, L. R., Hill, R. E., Boynton, W. V., Smith, M. D., and Pearl, J. C. (2006). Mars atmospheric water vapor abundance: 1991–1999, emphasis 1998–1999. *Icarus*, 184:372–400.
- Sprague, A. L., Hunten, D. M., Hill, R. E., Doose, L. R., and Rizk, B. (2001). Water Vapor Abundances over Mars North High Latitude Regions: 1996-1999. *Icarus*, 154:183–189.
- Sprague, A. L., Hunten, D. M., Hill, R. E., Rizk, B., and Wells, W. K. (1996). Martian water vapor, 1988-1995. *J. Geophys. Res.*, 101:23229–23254.
- Squyres, S. W., Grotzinger, J. P., Arvidson, R. E., Bell, J. F., Calvin, W., Christensen, P. R., Clark, B. C., Crisp, J. A., Farrand, W. H., Herkenhoff, K. E., Johnson, J. R., Klingelhöfer, G., Knoll, A. H., McLennan, S. M., McSween, H. Y., Morris, R. V., Rice, J. W., Rieder, R., and Soderblom, L. A. (2004). In Situ Evidence for an Ancient Aqueous Environment at Meridiani Planum, Mars. *Science*, 306:1709–1714.
- Tamppari, L. K. and The Phoenix Team (2006). The Phoenix lander and climate science on the surface in 2008. In Forget, F., Lopez-Valverde, M. A., Desjean, M. C., Huot, J. P., Lefevre, F., Lebonnois, S., Lewis, S. R., Millour, E., Read, P. L., and Wilson, R. J., editors, *Mars Atmosphere Modelling and Observations*, pages 714.
- Tillman, J. E. (1988). Mars global atmospheric oscillations - Annually synchronized, transient normal-mode oscillations and the triggering of global dust storms. *J. Geophys. Res.*, 93:9433–9451.
- Titov, D. V. (2002). Water vapour in the atmosphere of Mars. *Advances in Space Research*, 29:183–191.
- Titov, D. V. and Haus, R. (1997). A fast and accurate method of calculation of gaseous transmission functions in planetary atmospheres. *Planet. Space Sci.*, 45:369–377.
- Titov, D. V., Markiewicz, W. J., Thomas, N., Keller, H. U., Sablotny, R. M., Tomasko, M. G., Lemmon, M. T., and Smith, P. H. (1999). Measurements of the atmospheric water vapor on Mars by the Imager for Mars Pathfinder. *J. Geophys. Res.*, 104:9019–9026.
- Titov, D. V., Moroz, V. I., Grigoriev, A. V., Rosenqvist, J., Combes, M., Bibring, J.-P., and Arnold, G. (1994). Observations of water vapour anomaly above Tharsis volcanoes on Mars in the ISM (Phobos-2) experiment. *Planet. Space Sci.*, 42:1001–1010.

- Titov, D. V., Rosenqvist, J., Moroz, V. I., Grigoriev, A. V., and Arnold, G. (1995). Evidences of the regolith-atmosphere water exchange on Mars from the ISM (Phobos-2) infrared spectrometer observations. *Advances in Space Research*, 16:23–.
- Vold, R. D. and Vold, M. J. (1983). *Colloid and Interface Chemistry*, pages 71–114. Addison Wesley.
- Wolff, M. J., Clancy, R. T., Smith, M. D., Murchie, S., and The Crism Science Team (2006). Atmospheric science with MRO/CRISM: fun, fun, fun. In Forget, F., Lopez-Valverde, M. A., Desjean, M. C., Huot, J. P., Lefevre, F., Lebonnois, S., Lewis, S. R., Millour, E., Read, P. L., and Wilson, R. J., editors, *Mars Atmosphere Modelling and Observations*, pages 712.
- Zent, A. P., Howard, D. J., and Quinn, R. C. (2001). H<sub>2</sub>O adsorption on smectites: Application to the diurnal variation of H<sub>2</sub>O in the Martian atmosphere. *J. Geophys. Res.*, 106:14667–14674.
- Zent, A. P. and Quinn, R. C. (1995). Simultaneous adsorption of CO<sub>2</sub> and H<sub>2</sub>O under Mars-like conditions and application to the evolution of the Martian climate. *J. Geophys. Res.*, 100:5341–5349.
- Zubrin, R. and Wagner, R. S. (1996). *The case for Mars : the plan to settle the red planet and why we must*. New York : The Free Press, 1996.
- Zurek, R. W. (1992). *Comparative aspects of the climate of Mars - an introduction to the current atmosphere*, pages 799–817. Mars.
- Zurek, R. W., Barnes, J. R., Haberle, R. M., Pollack, J. B., Tillman, J. E., and Leovy, C. B. (1992). *Dynamics of the atmosphere of Mars*, pages 835–933. Mars.

# Publications

Fouchet, T., Lellouch, E., Ignatiev, N.I., Forget, F., Titov, D.V., **Tschimmel, M.**, Montmessin, F., Formisano, V., Giuranna, M., Maturilli, A., Encrenaz, T. (2007). Martian water vapor: Mars Express PFS/LW observations. *Icarus*, *accepted*



# Acknowledgements

First of all, my deep gratitude goes to my supervisor Dr. Dmitri Titov who always took his time and patience for giving advices and supporting me to the full extent. I can only say I could not have asked for a better supervisor! My thanks also include Dr. Keller whose experience gave me valuable inspiration and help. In the end, I got really hooked up by Mars in July 1997 when *Pathfinder* landed; I realized "That's what I want to do!". Because of this it was an honour to work at the MPAe/MPS in the Keller group.

Then I would like to thank of course my university supervisor Prof. Tilgner and my supervisor at the MPS Dr. Schmitt who accepted my PhD thesis and always provided me with all the necessary support. In particular, the possibility to do my PhD as part of the International Max Planck Research School is an unvaluable experience, both in scientific terms and intercultural experience.

My thanks and best wishes go also to Luca Maltagliati, to Nikolay Ignatiev at IKI in Moscow and to all the people of the PFS team (and others) at IFSI in Rome, in particular Prof. Formisano and Marco Giuranna. Thank you all for your contributions and discussions, and, even more, the friendships that came out of it.

Furthermore, my thanks include the ISSI in Bern that provided the excellent meeting opportunity for all people working about water vapour on Mars. I want to thank Anna Fedorova, Oleg Korablev, Emmanuel Lellouch, Thierry Fouchet, Ann Sprague and Mike Smith for the fruitful discussions and instructive days of work together.

Apart from doing research with PFS I had the pleasure to work with the Venus Monitoring Camera (VMC) during its calibration. Out of this reason I express my gratitude to Dr. Markiewicz and Dr. Titov for giving me this opportunity to gain a lot of laboratory experience and especially to witness the launch of *Venus Express* from Bajkonur. Unforgettable! In addition, my thanks go to Ilse Sebastian, Arne Dannenberg, Denis Beljaev, Nikolay Ignatiev, Pedro Russo and Richard Moissl for the entire "VMC experience".

I would like to say how thankful I am for the great time I had in Lindau and Göttingen. This was only possible because of the wonderful atmosphere at the institute and the friendship with the IMPRS students. Thank you all for that! I cannot mention everybody I would like to (just have a look on the website of the IMPRS). Yet I would like to thank my office mates Stefan Schröder, Maxim Kramar, Pedro Russo and Kristofer Hallgren for the fabulous working atmosphere and friendship.

My thanks and love go also to my parents, of course. I could not do what I do without your endless love and support. With all my heart I thank you! And as well thanks to my uncle Udo for the great discussions and the book that started it all...

Finally, "thank you!" to my best friends Niki (R.I.P.) and Mario who believed in me when others didn't, who encouraged me to follow my dreams and who taught me the meaning of true friendship. And of course a big thanks for you, my dear Fabiola, who came into my life in the darkest hour and showed me the light.



# Curriculum Vitae

Name: Tschimmel  
Vorname: Martin Alexander  
Geburtsdatum: 18. April 1977  
Geburtsort: Roding, Deutschland  
Staatsangehörigkeit: deutsch

## Schule:

- Grundschule: September 1983 bis Juli 1987 in Eferding und Pasching (Österreich)
- Gymnasium: September 1987 bis Juli 1996 am St.–Michaels–Gymnasium in Metten; zur gleichen Zeit Besuch des Internats des Benediktinerklosters

## Studium:

- Wintersemester 1996: Politik und slawische Philologie an der LMU München
- Sommersemester 1997 - Wintersemester 1997: Betriebswirtschaftslehre an der LMU München
- Sommersemester 1998: Volkswirtschaftslehre in Heidelberg (Vordiplom im Juni 1998), Teilnahme an ersten Physikvorlesungen
- Wintersemester 1998 - Sommersemester 2003: Physik an der LMU München, Diplomarbeit: Suche nach extrasolaren Planeten mittels Transitmethode
- September - November 2003: IAESTE Praktikum am Institut für biochemische Physik der Russischen Akademie der Wissenschaften in Moskau
- Dezember 2003 - Januar 2004: Anstellung am Institut für Astronomie in München
- Februar 2004 - Januar 2007: Doktorand der International Max Planck Research School on Physical Processes in the Solar System and Beyond, am Max-Planck-Institut für Sonnensystemforschung (MPS) in Katlenburg-Lindau

